Finite Volume Methods for Tsunamis Generated by Submarine Landslides

Jihwan Kim

A dissertation
submitted in partial fulfillment of the
requirements for the degree of

Doctor of Philosophy

University of Washington

2014

Reading Committee:

Randall J. LeVeque, Chair

Ka Kit Tung

Peter Mackenzie-Helnwein

Program Authorized to Offer Degree:
Applied Mathematics

University of Washington

Abstract

Finite Volume Methods for Tsunamis Generated by Submarine Landslides

Jihwan Kim

Chair of the Supervisory Committee:
Professor Randall J. LeVeque
Applied Mathematics

Submarine landslides can generate tsunamis, and the generated waves can be catastrophic when a large volume of landslide material is involved. Moreover, large earthquakes are often accompanied by submarine landslides that can enhance the magnitude of the resulting tsunamis. In this thesis, numerical schemes are developed to solve the wave propagation problems generated by submarine landslides. Assuming the landslides in a flow regime, depth-averaged models are studied, and finite volume methods are extended to the fully coupled multi-layer shallow water equations. From the fully coupled model, an efficient simplified approach is derived that is often appropriate for tsunamis generated by submarine landslides. These waves can have relatively short wavelength, and another class of equations may be necessary that can handle the dispersion of waves. Several types of the Boussinesq equations have been reviewed and implemented with a hybrid of high-resolution finite volume and finite difference methods. Stability analysis and convergence tests have been performed for the hybrid scheme. The develpoment has been done in the context of the GEOCLAW framework, a code designed to handle the single-layer shallow water equations, that uses adaptive mesh refinement to model tsunami propagation on a global scale with inundation of specific regions on a fine grid. The newly developed methods, tested on the exact solutions, are validated by comparing to laboratory experiments and by applying to historic events such as the Papua New Guinea 1998 and Storegga slides. Possible scenarios of submarine landslides and resulting tsunamis on the Washington coast were investigated.

TABLE OF CONTENTS

LIST OF FIGURES

ACKNOWLEDGMENTS

I would like to thank my advisor, Randall J. LeVeque, for his constant encouragement, helpful suggestions, and patience. This work would not have been possible without his constant support and push for making this a better body of work.

My thesis committee, Ka Kit Tung, Peter Mackenzie and Parker MacCready have also provided indelible advice and comments. Peter Mackenzie has been of particular help and I thank him for the many discussions we have had over the years that have often caused me to rethink how I was approaching a problem.

I am also grateful for the current and former students of Professor LeVeque who have provided a template for success and guidance throughout the years. The rest of the students and faculty of the Applied Mathematics department have also all been immensely helpful and I would like to thank them for their input and collaboration.

Finally, I would like to thank my friends and family that have been ever patient and encouraging through my years in graduate school. I am also forever indebted to Jeong-Ha Oh whose constant patience and encouragement have been essential.

DEDICATION

to My Family

Chapter 1

INTRODUCTION

1.1 Motivation

Landslides are a common cause of tsunami generation, and when a large volume of material is involved in a landslide, it can trigger a catastrophic tsunami. For example, on 17 July 1998, a submarine landslide generated destructive waves at the North coast of Papua New Guinea when a magnitude 7.0 earthquake hit the area. The earthquake itself did not generate notable waves, but shook out an unstable area at the verge of the continental shelf and triggered a large underwater landslide of 3-8 km^3 [47, 79, 100]. The generated tsunami was as high as 15 meter and killed about 2,200 people. Another case is found from the historical evidence that supports the existence of large submarine landslides at the edge of continental shelf on the North coast of Norway. A landslide called the *Storegga slide* occurred about 8000 years ago with a total volume of 3500 km^3[16, 20, 31]. The generated waves were as high as 20 m at Shetland island, and tsunami deposits were located as far away as Greenland [19, 82, 137]. Thus submarine landslides should be considered as a source of tsunamis.

Not only can submarine landslides alone generate destructive waves, but also tsunamis generated by earthquakes can be enhanced by submarine landslides initiated by the earthquake. The Indian Ocean tsunami in 2004 and Tohoku tsunami in 2011 were mainly generated by tectonic plate movement, and the generated waves were amplified by submarine landslides. In the study of Tohoku 2011 event, several possiblilities have been studied to explain large tsunamis detected at the south coast of Hokkaido. One explanation is suggested by Grilli et al. [56] with the submarine slump, and showed that the tsunami excited by a dual source reproduces both the recorded onshore run-up and the wave heights and wave frequencies recorded at offshore buoys. The wave generation mechanism by submarine landslides is different from the earthquakes, and the characteristics of waves can be also

different.

When the tsunami is triggered only by a large-scale earthquake, the shallow water equations are often an appropriate model, because the wavelength of tsunamis generated by subduction earthquakes is several hundred kilometers. Other systems may be preferred when the waves are generated mainly by submarine landslides, because waves generated by underwater slides may have different characteristics. As noted by Matsuyama et al. [100], the wavelength of tsunamis generated by submarine landslides is a few kilometers, and waves are generated over a time period of several minutes. For those waves with short wavelength, dispersion of waves can be of importance. One class of efficient depth-averaged models with dispersion is the *Boussinesq*-type equations, which can produce more accurate results for those waves that are involved with the submarine landslide deformation.

The purpose of this thesis is to develop an accurate and efficient numerical scheme for tsunamis generated by submarine landslides. With mathematical analysis and numerical simulations, we derive and validate our equations and methods through comparison against laboratory experiments and real-world observations. We also focus on developing a numerical package that is easy to use for other users who are investigating tsunami and landslide modeling.

1.2 Background

1.2.1 Mathematical Modeling

Tsunamis generated by submarine landslides have been modeled in several different ways. One scheme is to prescribe a perturbed water surface elevation that corresponds to the bathymetry deformation. In this scheme, the actual deformation of the bathymetry is ignored, and possible cases of wave elevation are tested as the initial conditions. Therefore this may be very similar to the wave generation by earthquakes. For example, see Harbitz [63], Ward [138] and Satake [122].

Another method is to regard the submarine landslide as a rigid body. The advantage of this scheme is directly related to the convenience of using rigid bodies in the laboratory experiments. Performing experiments is easier with a rigid body than with granular materials,

in which case the change of the bathymetry can be exactly measured in the experiments. Several characteristics such as mixing and pore pressure, which are observed from granular flows, can be ignored. Since it is also possible to prescribe and record the exact motion of rigid body, comparison to the numerical simulations is convenient as well. For example, depth-averaged equations, such as the shallow water equations and the Boussinesq type equations, have been widely used for the governing equations of the surface waves. See Pelinovsky and Poplavsky [114], Watts [139], Lynett and Liu [90], Grilli et al. [57], Enet and Grilli [38], Fuhrman and Madsen [94], and Zhou and Teng [144].

Another approach is to regard the submarine landslide as a fluid flow. In numerical modeling, a multi-phase fluid flow model is solved by treating the water and landslide as two different fluid flows. Jiang and LeBlond [78], Heinrich et al. [67], and Imamura and Hashi [74] used multi-phase fluid models. In this type of approach, several choices for submarine landslide models are possible such as Savage-Hutter, viscous fluid, and Coulomb friction models, for example. The Savage-Hutter model was introduced by Savage and Hutter [123] to explore the deformation of dry granular flow along a channel. Fernández-Nieto et al. [40] extended the Savage-Hutter model for landslide generated tsunami modeling. The viscous fluid model has been used in landslide modeling, and Jiang and LeBlond [78] derived coupled multi-layer shallow water equations. They investigated fully-coupled and one-way coupled models, and compared numerical results to study the regime where the one-way coupled model is valid. They concluded that the difference between the two models is smaller when the landslide is located in deeper ocean and the density difference is larger. Based on these results, Heinrich et al. [67] applied a one-way coupled model to the Papua New Guinea 1998 event with the viscous fluid model and the Coulomb friction model for the landslide deformation.

In tsunami modeling the shallow water equations are widely used for the governing equations of the waves. But the Boussinesq-type equations are also adopted when the dispersion of waves is important. Computationally, the Boussinesq equations are much more expensive than the shallow water equations, because an implicit method must be used. For the derivations and numerical studies of the Boussinesq-type equations, see Peregrine [115], Nwogu [107], Madsen, Sørenson and Schäffer [96], [95], [124], Gobbi et al. [51], Lynett and

Liu [91], Liu and Sun [89], Ataie-Ashitiani and Najafi-Jilani [8], and Zhou and Teng [144].

1.2.2 Numerical Studies

Mathematical models can be validated through numerical simulations by comparing the results with laboratory and field data. There are a limited number of laboratory experiments which were carried out with solid block and granular materials. Some of the notable experiments include those of Ataie-Ashtiani and Najafi-Jilani [7], Fleming et al. [44], Fritz et al. [46], Watts [139], and Zhou and Teng [144]. Field observations of the tsunamis generated by landslides are scarce, and historical data are also hard to find. Well known cases are the 1998 Papua New Guinea tsunami, 1929 Grand Banks tsunami, and the Storegga slide. The Papua New Guinea tsunami in 1998 has a run-up record with 20 meter in some place which was reported by Synolakis et al. [130]. Heinrich et al. [67] and Imamura and Hashi [74] have carried out numerical simulations on this event independently. The Storegga slides occurred about $8,000$ years ago at the edge of Norway's continental shelf. and Bondevik et al. [15] and Haflidason et al. [60] used rigid body motion schemes for the numerical studies.

In previous numerical simulations, finite difference schemes have been extensively used when the governing equations for surface waves are depth-averaged. If the governing equations are shallow water equations, then finite volume methods are often employed instead. However, the finite volume methods for the Boussinesq type equations have been rarely investigated including stability and convergence studies. See Bonneton et al. [17] and Dutykh et al. [36] for example.

1.3 Objectives

The main objective of this thesis is to develop an efficient and robust numerical scheme which can solve the wave propagation problem generated by submarine landslides. Since depth-averaged models reduce computational efforts in numerical studies of the fluid dynamics, several different types of the depth-averaged models will be examined and adopted. Numerical schemes will be developed in the scope of the finite volume methods with stability analysis.

Appropriate models for the landslide deformation will be also examined. The slope movement can be categorized into five types, which are falls, topples, slides, spreads and flows [116], and, in this thesis, submarine landslides will be considered as flows. The shallow water equations will be adopted for the main governing equations, and various friction models will be tested such as the Coulomb friction and viscous fluid models.

The landslide movement will generate waves, and the *fully coupled* model include the interaction between the landslide and the water column. Because the fully coupled multi-layer shallow water equations are conditionally hyperbolic and computationally expensive, alternative approaches have been investigated. See Audusse [9], Abgrall and Karni [1] and Bouchut and Zeitlin [18] for instance. In the applications of tsunamis generated by submarine landslides, the one-way coupled model suggested by Jiang and LeBlond [78], is an efficient scheme. The *one-way* coupled model only considers the influence to the water by the landslide deformation, and ignores the reaction of the water column to the ongoing landslide. In this thesis, the one-way coupled model will be investigated extensively. The numerical experiments will be performed with the *fully coupled* and *one-way coupled* models to investigate when the one-way coupled model is valid.

Based on the one-way coupled model, a different class of the wave model will be investigated instead of the shallow water equations. Since the waves generated by submarine landslides often have shorter wavelength than those by subduction earthquakes, the Boussinesq type equations will be considered to incorporate dispersion of waves. The Boussinesq-type equations require another numerical schemes, and the hybrid of the finite volume and finite difference scheme will be explored.

Several difficulties arise in developing the Boussinesq solvers. One of the difficulties is related to the efficiency of the Boussinesq-type solver. For example, consider one of the simplest Boussinesq-type equations derived by Peregrine [115], which can be rearranged as follows,

$$h_t + (hu)_x = 0, \tag{1.1}$$

$$(hu)_t + \left(hu^2 + \frac{g}{2}h^2\right)_x + ghb_x + S_1 = 0, \tag{1.2}$$

and

$$S_1 = (I - D_1)^{-1} \Psi_1, \tag{1.3}$$

with

$$D_1 w = \frac{1}{2} H^2 w_{xx} - \frac{1}{6} H^3 \left(\frac{w}{H} \right)_{xx},$$

and

$$\Psi_1 = \frac{1}{2} H^2 \left((hu^2)_x + g(h\eta_x) \right)_{xx} - \frac{1}{6} H^3 \left(\frac{(hu^2)_x + gh\eta_x}{H} \right)_{xx}.$$

This set of equations can be decomposed into the shallow water part and dispersion part. In the equation (1.2), S_1 represents the dispersion part, and the shallow water equations are recovered when $S_1 = 0$. To compute S_1 in the equation (1.3), a large sparse linear system needs to be solved, and this step determines the efficiency of the entire numerical scheme. In the 1-dimensional case, the sparse matrix is tridiagonal and can be computed efficiently. But in the 2-dimensional case, the sparse matrix system has a form that is computationally expensive. In Chapter 6, these difficulties will be addressed and studied in detail.

The developed approaches will be applied to test problems from small laboratory experiments to global scale problems. Laboratory experiments include NTHMP benchmarking project [52] and Watts' experiments [139]. Large scale problems will be considered such as Valdes slide [142], Papua New Guinea 1998, and Storegga slide.

In solving large scale problems, our interests are often focused on a small area which requires fine grids. In developing an efficient numerical scheme, adaptive mesh refinement(AMR) is one of the main components. Figure 1.1 shows a snapshot of the numerical simulation of the Storegga slide with AMR around the Shetland Islands which are located at the lower left corner of the Figure. In Figure 1.2, snapshots are shown with uniform coarse grids (left) and AMR (right). Complex topography of the Shetland Islands requires fine grids which are necessary for the accurate forecast of tsunamis. Using fine grids in the entire domain is computationally expensive, and AMR is one of the efficient methods that can cover a large domain and obtain tsunami inundation computation in a small area of our interest.

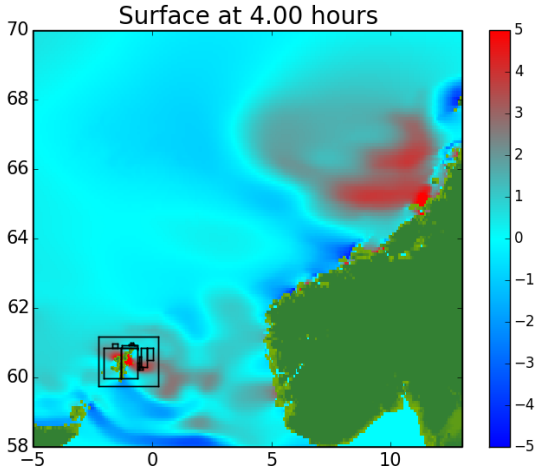

Figure 1.1: Numerical simulation of the Storegga slide with adaptive mesh refinement around the Shetland Islands (lower left).

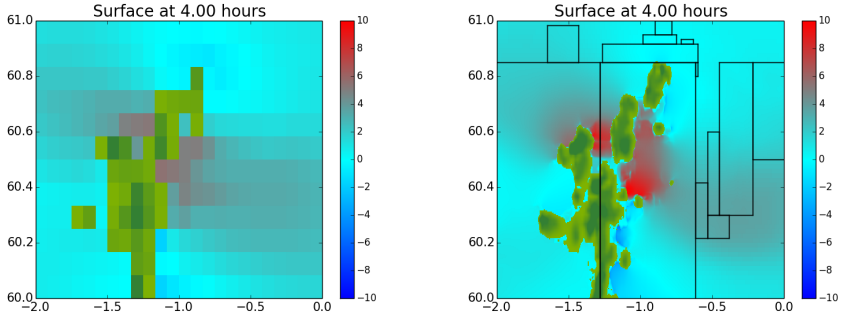

Figure 1.2: Tsunami propagation at the Shetland Island with coarse and fine grids. For the left figure, uniform grid was used with $\Delta x = \Delta y = 5'$. For the right figure, an adaptive mesh refinement scheme was used with the smallest grid size equal to $15''$.

The numerical schemes in this work are developed in the context of the finite volume method with the GEOCLAW in its foundation. The GEOCLAW software is a shallow water equations solver based on the finite volume method with AMR, which has been used in many tsunami researches. The GEOCLAW software will be extended in two directions. One

extension is to develop numerical schemes for the fully coupled multi-layer shallow water equations. The other direction is to extend the one-way coupled model with the Boussinesq-type equations and handle the dispersion of waves with efficiency.

The purpose of this thesis is to provide several schemes for the multi-layer depth-averaged equations with focus on the tsunamis generated by submarine landslides. The schemes must be able to handle dry state problems and dispersive terms correctly, and efficiently at the same time. Whether the Boussinesq-type equations are applicable to the tsunami modeling is discussed when the results are compared to the field survey data.

1.4 Overview

In Chapters 2 and 3, a general overview of conservation laws will be provided with emphasis on the shallow water system. In Chapter 2 some theory on hyperbolic PDEs and properties of Riemann problems will be discussed. Chapter 3 reviews finite volume methods and Godunov-type methods with approximate Riemann solvers and numerical treatments of the source terms. In Chapter 4, the multi-layer shallow water system is derived and approximate Riemann solvers are investigated for this system with analytic interpretations. In Chapter 5, numerical modeling schemes for landslides are reviewed, and then a one-way coupled model is suggested for the numerical modeling of the waves generated by submarine slides. In Chapter 6, another class of depth averaged equations is presented. Numerical schemes for the Boussinesq type equations are investigated with convergence and stability studies. In order to validate the developed numerical schemes, several results are presented in one dimensional cases in Chapter 7. In Chapter 8, numerical tests for two dimensional cases will be considered including large scale problems, and compared with field survey data. Finally, Chapter 9 concludes with a summary of the findings, and possible future directions of research.

Chapter 2

CONSERVATION LAWS AND RELATED SYSTEMS

In this chapter, we review the solution of the hyperbolic conservation law and investigate the properties of the shallow water equations. See LeVeque [87, 86], Lax [84] and Evans [39] for details.

2.1 Hyperbolic Conservation Laws

2.1.1 Conservation Laws

Consider a class of partial differential equations on n space dimension

$$\frac{\partial}{\partial t}q(x,t) + \sum_{j=1}^{n} \frac{\partial f_j(q)}{\partial x_j} = 0, \quad x \in \mathbb{R}^n, \tag{2.1}$$

where $q \in \mathbb{R}^m$ is a vector of m state variables and $f_j(q) \in \mathbb{R}^m$ is a vector of corresponding fluxes in the j^{th} direction. This class of partial differential equations is called *conservation laws*. For any region $\Omega \subseteq \mathbb{R}^n$ and an outward unit normal vector $\omega = (\omega_1, \ldots, \omega_n)$ to the boundary $\partial\Omega$ of Ω, applying the divergence theorem to the equation (2.1) yields

$$\frac{d}{dt}\int_{\Omega} q dx + \sum_{j=1}^{n} \int_{\partial\Omega} f_j(q)\omega_j dS = 0. \tag{2.2}$$

The equation (2.2) implies that the change of the quantity q in time is determined by the flux functions f_j at the boundary $\partial\Omega$.

2.1.2 Hyperbolic Systems of Conservation Laws

The equation (2.1) can be written as a quasi-linear system

$$\frac{\partial}{\partial t}q(x,t) + \sum_{j=1}^{n} A_j(q)\frac{\partial q}{\partial x_j} = 0, \tag{2.3}$$

where (i,k) element of A_j is

$$(A_j)_{ik} = \frac{\partial f_{ji}}{\partial q_k},$$

with $f_j = [f_{j1}, f_{j2}, \ldots, f_{jm}]^T$. The system (2.3) is *hyperbolic* if for all $\alpha_1, \alpha_2, \ldots, \alpha_n \in \mathbf{R}$ the matrix $\mathbf{A} := \alpha_1 A_1 + \alpha_2 A_2 + \cdots + \alpha_n A_n$ has real eigenvalues and a complete set of eigenvectors. In addition, for each $p = 1, \ldots, m$, the p-th field is *genuinely nonlinear* if

$$\nabla \lambda_p(q) \cdot r_p(q) > 0,$$

with eigenvalues λ_p and eigenvectors r_p of A_j for all q. The p-th field is *linearly degenerate* if

$$\nabla \lambda_p(q) \cdot r_p(q) = 0,$$

for all q.

2.2 Discontinuities and weak solutions

2.2.1 Rankine-Hugoniot condition

Discontinuous solutions for the system (2.1) cannot be defined in the classical sense. A general class of the solutions can be defined from the integral form (2.2) which are called *weak solutions*. Let q be a solution to the system of conservation law (2.2) which is piecewise continuous. Across the shocks, the following condition is called *Rankine-Hugoniot jump conditions* (2.4),

$$|s|[[q]] = \sum_{j=1}^{n} \hat{s}_j [[f_j(q)]], \tag{2.4}$$

where $|s|$ is the instantaneous propagation speed, $\hat{s}_j$ is the unit vector in the direction of the propagation, and $[[\cdot]]$ denotes the jump at the discontinuity

2.2.2 Entropy condition

While there exists a unique smooth solution for the differential form of the conservation laws (2.1) as long as it remains smooth, the uniqueness is not guaranteed for discontinuous weak solutions of the integral form (2.2). An admissiblility condition, based on the physics, is called an *entropy condition*.

Definition A function $S(q)$ is called an *entropy* for a system of conservation laws (2.1) if every smooth solution of (2.1) satisfies an additional conservation law

$$\partial_t S + \nabla \cdot F = 0, \tag{2.5}$$

where $F(q)$ is called the *entropy flux*. In addition, $S(q)$ is required to be a *convex* function of q.

If $q(x,t)$ is an admissible solution of (2.1), then it satisfies, in the sense of distribution,

$$\partial_t S(q) + \partial_x F(q) \leq 0,$$

for any *entropy* S and *entropy flux* F. Details can be found at Friedlander [45] and Lax [84] for example.

2.3 Riemann problem

Consider a scalar conservation law as follows,

$$q_t + f(q)_x = 0, \quad x \in \mathbb{R} \quad \text{and} \quad t > 0, \tag{2.6}$$

with piecewise constant initial conditions

$$q(x,0) = \begin{cases} q_l, & \text{if} \quad x < 0, \\ q_r, & \text{if} \quad x > 0. \end{cases} \tag{2.7}$$

This initial value problem (2.6) and (2.7) is called the *Riemann* problem. There are three important cases for the solutions of the *Riemann problem*; *rarefaction waves*, *shocks* and *contact discontinuities*.

Assuming $f(q)$ is uniformly convex, i.e. genuinely nonlinear, the entropy condition determines the unique solution to the *Riemann problem*, and leads the following theorem.

Theorem 2.3.1 *1. If $q_l > q_r$, the unique entropy solution of the Riemann problem is*

$$q(x,t) := \begin{cases} q_l, & \text{if} \quad \frac{x}{t} < s, \\ q_r, & \text{if} \quad \frac{x}{t} > s, \end{cases}$$

where

$$s := \frac{f(q_l) - f(q_r)}{q_l - q_r}.$$

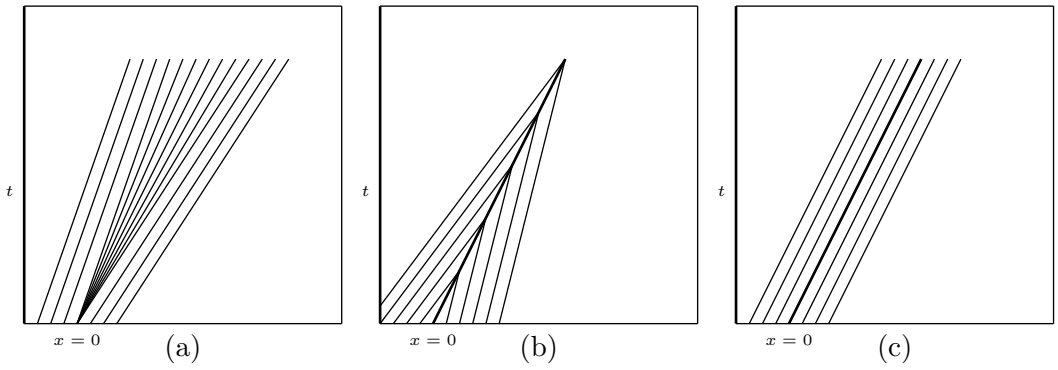

Figure 2.1: Three special cases for the solution of the Riemann problem. (a) rarefaction waves in the p-th field (b) shock wave (c) contact discontinuity

2. If $q_l < q_r$, the unique entropy solution of the Riemann problem is

$$q(x,t) = \begin{cases} q_l, & \text{if } \frac{x}{t} < f'(q_l), \\ g\left(\frac{x}{t}\right), & \text{if } f'(q_l) < \frac{x}{t} < f'(q_r), \\ q_r, & \text{if } \frac{x}{t} > f'(q_r). \end{cases}$$

In the first case of the Theorem 2.3.1, the *shock wave* of speed s is connecting two states q_l and q_r. The second case is called as *rarefaction waves* which connects two states continuously.

If the $f''(q) \equiv 0$, then *contact discontinuities* can exist in the Riemann problem. In this case, two states q_l and q_r are connected by a discontinuity where th p-th characteristic speed is constant so that $\lambda(q_l) = \lambda(q_r)$.

For a system of conservation law (2.3), the unique solution can be determined by the following theorem.

Theorem 2.3.2 *A discontinuity separating states q_l and q_r propagating at speed s, satisfies the Lax entropy condition if there is an index p such that*

$$\lambda^l(q_l) > s > \lambda^p(q_r),$$

so that p-characteristics are impinging on the discontinuity, while the other characteristics

are crossing the discontinuity,

$$\begin{aligned} \lambda^j(q_l) &< s \quad \textit{and} \quad \lambda^j(q_r) < s \quad \textit{for} \quad j < p, \\ \lambda^j(q_l) &> s \quad \textit{and} \quad \lambda^j(q_r) > s \quad \textit{for} \quad j > p. \end{aligned}$$

In this expression, we assume the eigenvalues are ordered so that $\lambda^1 < \lambda^2 < \cdots < \lambda^n$ *in each state.*

2.4 Shallow water equations

As an example, the shallow water equations will be considered in this section. The equations can be derived from depth-averaging the Navier-Stokes equations assuming the wavelength is much greater than the depth of water. The shallow water equations with a flat bottom are given as

$$\begin{aligned} &h_t + (hu)_x = 0, \\ &(hu)_t + \left(hu^2 + \frac{1}{2} g h^2 \right)_x = 0, \end{aligned}$$

where $h(x,t)$ and $u(x,t)$ are the height and speed of water, and g is the gravitational constant. This can be written in quasi-linear form as follows,

$$q_t + A(q) q_x = 0,$$

where

$$q = \begin{bmatrix} h \\ hu \end{bmatrix}, \quad A(q) = \begin{bmatrix} 0 & 1 \\ gh - u^2 & 2u \end{bmatrix}.$$

Then the eigenvalues of $A(q)$ are

$$\lambda_1 = u - \sqrt{gh}, \quad \text{and} \quad \lambda_2 = u + \sqrt{gh},$$

and corresponding eigenvectors are

$$r_1 = \begin{bmatrix} 1 \\ \lambda_1 \end{bmatrix}, \quad r_2 = \begin{bmatrix} 1 \\ \lambda_2 \end{bmatrix}.$$

If the depth of the water is positive $h > 0$, then the eigenvalues are real with $\lambda_1 < \lambda_2$ and $\nabla\lambda_k \cdot r_k = \frac{3\sqrt{g}}{\sqrt{h}} \neq 0$. Thus the shallow water system is hyperbolic and genuinely nonlinear if $h > 0$.

Consider the Riemann problem with initial conditions,

$$(h, hu)(x, 0) = \begin{cases} (h_l, h_l u_l), & x < 0, \\ (h_r, h_r u_r), & x > 0. \end{cases}$$

The aim is to determine the middle state $(h_*, h_* u_*)$. Since the system is hyperbolic and genuinely nonlinear, the left and right states can be connected by shock and/or rarefaction not by the contact discontinuity.

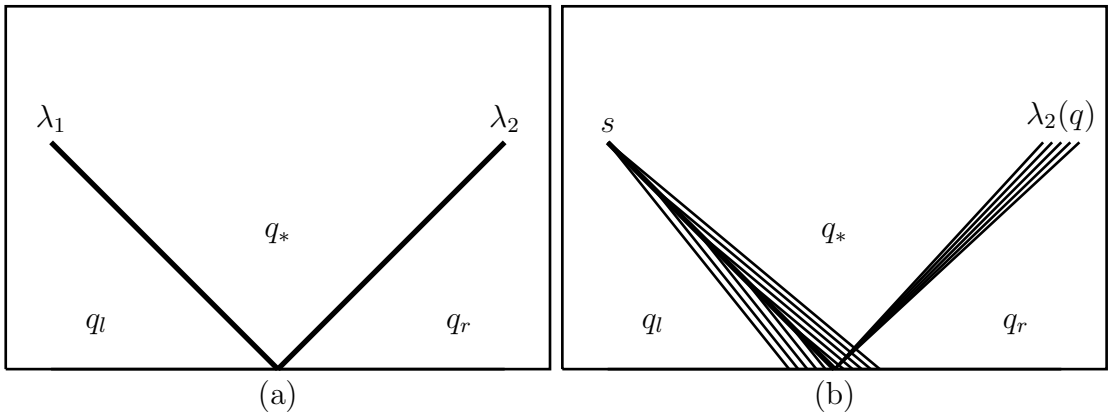

Figure 2.2: The solution to a Riemann problem for a linear system in the x-t plane. The solution consists of m-waves moving at the speed of the corresponding eigenvalue λ_p. (b) An example of a solution to a nonlinear Riemann problem in the x-t plane showing each of the waves or characteristic transitions. The example shows 1-characteristics for a shock in the first field, and shows a rarefaction wave in the second field.

If q_l is connected to q_* by a shock with speed s_1, then the Rankine-Hugoniot condition should be satisfied,

$$\begin{aligned} s_1(h_* - h_l) &= (h_* u_* - h_l u_l), \\ s_1(h_* u_* - h_l u_l) &= h_* u_*^2 - h_l u_l^2 + \frac{1}{2}\left(g h_*^2 - g h_l^2\right). \end{aligned}$$

Eliminating s_1 from these equations, we have

$$u_l = u_* - \sqrt{\frac{g}{2}\left(\frac{h_*}{h_l} - \frac{h_l}{h_*}\right)(h_* - h_l)}.$$

Similarly, if q_r and q_* are connected by a shock wave, then we have

$$u_r = u_* + \sqrt{\frac{g}{2}\left(\frac{h_*}{h_r} - \frac{h_r}{h_*}\right)(h_* - h_r)}.$$

It is possible to show that an integral curve in the phase plane of a genuinely nonlinear field corresponds to a constant contour of a function of q. This function is called *Riemann invariant* since the value of the function is invariant along an integral curve. For the shallow water system, the Riemann invariants are

$$w^1(q) = u + 2\sqrt{gh},$$
$$w^2(q) = u - 2\sqrt{gh}.$$

If the rarefaction wave connects q_l and q_*, then $w^1(q_l) = w^1(q_*)$. If q_r and q_* are connected by rarefaction, then $w^2(q_*) = w^2(q_r)$.

The 1-wave and 2-wave can be rarefaction wave or shock wave, and thus there are four possible cases. Physically, the middle state $(h_*, (hu)_*)$ should be unique when the left and right states are given. The unique solution can be determined by *Lax entropy condition* 2.3.2.

2.5 Higher dimension shallow water equations

The shallow water equation of 2-dimension is written as

$$q_t + f(q)_x + g(q)_y = 0,$$

where

$$q = \begin{bmatrix} h \\ hu \\ hv \end{bmatrix}, \quad f(q) = \begin{bmatrix} hu \\ hu^2 + \frac{1}{2}gh^2 \\ huv \end{bmatrix}, \quad \text{and} \quad g(q) = \begin{bmatrix} hv \\ huv \\ hv^2 + \frac{1}{2}gh^2 \end{bmatrix}.$$

This system can be written in quasi-linear form,

$$q_t + A(q)q_x + B(q)q_y = 0,$$

where

$$A(q) = \begin{bmatrix} 0 & 1 & 0 \\ gh - u^2 & 2u & 0 \\ -uv & v & u \end{bmatrix}, \quad \text{and} \quad B(q) = \begin{bmatrix} 0 & 0 & 1 \\ -uv & v & u \\ gh - v^2 & 0 & 2v \end{bmatrix}$$

The eigenvalues and corresponding eigenvectors of $A(q)$ are,

$$\begin{aligned} \lambda_1 &= u - \sqrt{gh}, & r_1 &= [1, \lambda_1, v]^T, \\ \lambda_2 &= u, & r_2 &= [0, 0, 1]^T, \\ \lambda_3 &= u + \sqrt{gh}, & r_3 &= [1, \lambda_3, v]^T. \end{aligned}$$

The eigenvalues and corresponding eigenvectors of $B(q)$ are,

$$\begin{aligned} \lambda_1 &= v - \sqrt{gh}, & r_1 &= [1, u, \lambda_1]^T, \\ \lambda_2 &= v, & r_2 &= [0, 1, 0]^T, \\ \lambda_3 &= v + \sqrt{gh}, & r_3 &= [1, u, \lambda_3]^T. \end{aligned}$$

The two-dimensional shallow water equations are identical except a new second field which is linearly degenerate. This new second field is a contact discontinuity which propagates at the speed of $s = u^*$ or $s = v^*$ and separates two states initially in contact at $x = 0$. Thus the transverse velocity can be considered as passive tracer which has no effect on the Riemann problem. For details see [87].

Chapter 3

FINITE VOLUME METHOD

In this chapter, we study finite volume methods developed for the solution of the hyperbolic conservation laws. These methods can be interpreted as a class of finite difference methods, but the derivation is based on the integral form of the equations in which discontinuous solutions are admissible.

3.1 Finite Volume Method for Conservation Law

To derive a finite volume method, we divide the domain Ω into grid cells. For simplicity, consider one dimensional case. We denote the i-th grid cell by $\mathcal{C}_i = (x_{i-1/2}, x_{i+1/2})$ and assume that all the grids are uniform in size. The numerical solution $\mathcal{Q}_i^n$ is an approximation to the integral of the real solution $q(x, t_n)$,

$$\mathcal{Q}_i^n \approx \frac{1}{\Delta x} \int_{\mathcal{C}_i} q(x, t_n) dx, \tag{3.1}$$

where $\Delta x = x_{i+1/2} - x_{i-1/2}$ is the length of the cell.

The integral form of the conservation law (2.2) can be written as

$$\frac{d}{dt} \int_{\mathcal{C}_i} q(x, t) dx + f(q(x_{i+1/2}, t)) - f(q(x_{i-1/2}, t)) = 0. \tag{3.2}$$

Integrating the equation (3.2) from $t = t_n$ to $t = t_{n+1}$ yields

$$\int_{\mathcal{C}_i} q(x, t_{n+1}) dx - \int_{\mathcal{C}_i} q(x, t_n) dx + \int_{t_n}^{t_{n+1}} f(q(x_{i+1/2}, t)) dt - \int_{t_n}^{t_{n+1}} f(q(x_{i-1/2}, t)) dt = 0.$$

Rearranging and dividing by Δx gives

$$\frac{1}{\Delta x} \int_{\mathcal{C}_i} q(x, t_{n+1}) dx = \frac{1}{\Delta x} \int_{\mathcal{C}_i} q(x, t_n) dx \tag{3.3}$$

$$- \frac{1}{\Delta x} \left[\int_{t_n}^{t_{n+1}} f(q(x_{i+1/2}, t)) dt - \int_{t_n}^{t_{n+1}} f(q(x_{i-1/2}, t)) dt \right]. \tag{3.4}$$

This equation (3.4) states how the solution $\mathcal{Q}_i^{n+1}$ is determined by the previous states. For the numerical approximation $\mathcal{Q}_i^{n+1}$, we may rewrite the method in the flux-differencing form

$$\mathcal{Q}_i^{n+1} = \mathcal{Q}_i^n - \frac{\Delta t}{\Delta x}\left(F_{i+1/2}^n - F_{i-1/2}^n\right), \tag{3.5}$$

where

$$F_{i-1/2}^n \approx \int_{t_n}^{t_{n+1}} f(q(x_{i-1/2}, t)dt. \tag{3.6}$$

The accuracy and stability of the numerical scheme (3.5) depends on the approximation of the flux (3.6) which is conservative.

3.2 Godunov-type Methods

Godunov-type methods provide stable and consistent numerical schemes for solving the equation (3.5). These methods are often referred as *REA algorithm*, standing for reconstruct-evolve-average. In the reconstruction step, a piecewise constant function $\tilde{q}^n(x, t_n)$ is reconstructed form $\mathcal{Q}_i^n$ so that

$$\tilde{q}^n(x, t_n) = \mathcal{Q}_i^n, \quad \text{for all } x \in \mathcal{C}_i.$$

The next step is to evolve the hyperbolic equations exactly. to obtain $\tilde{q}^n(x, t_{n+1})$ at time Δt later where Δt is determined by the CFL condition. With the propagated information, the final step is averaging to obtain $\mathcal{Q}_i^{n+1}$,

$$\mathcal{Q}_i^{n+1} = \frac{1}{\Delta x}\int_{\mathcal{C}_i} \tilde{q}^n(x, t_{n+1})dx.$$

In order to implement this scheme, the evolving step requires solving differential equations with piecewise constant data, and the theory of Riemann problems can be used here.

3.2.1 The Wave-Propagation Form of Godunov Method

The last step of Godunov-type methods is finding the average of the cell $\mathcal{C}_i$ from the propagated information. For the linear hyperbolic system, the solution to the Riemann problem has the following relation

$$\mathcal{Q}_i^n - \mathcal{Q}_{i-1}^n = \sum_{p=1}^{m} \alpha_{i-1/2}^p r^p \equiv \sum_{p=1}^{m} \mathcal{W}_{i-1/2}^p,$$

where m is number of waves, and $\alpha^p_{i-1/2}$ and r^p are coefficients and eigenvectors corresponding to the eigenvalues λ^p for the Riemann problem at the cell interface of $\mathcal{C}_i$ and $\mathcal{C}_{i-1}$.

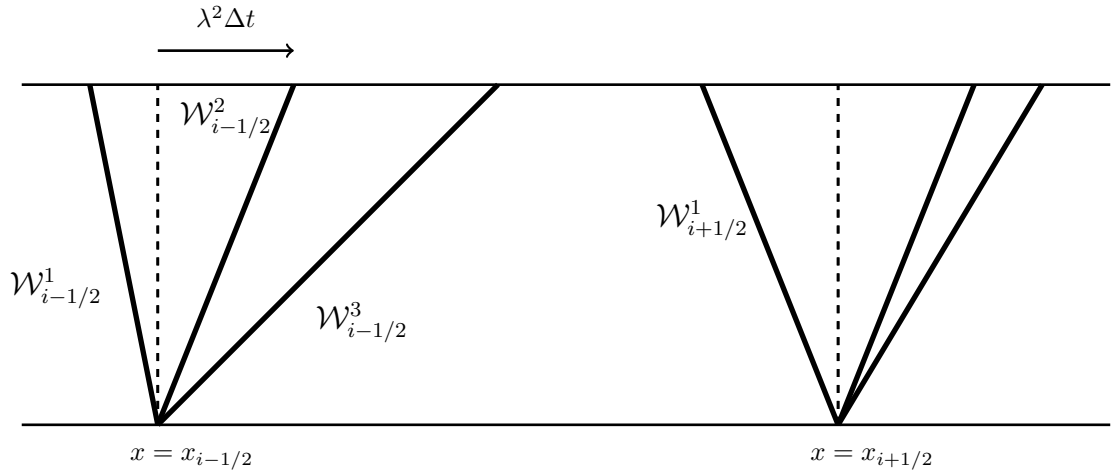

Figure 3.1: Diagram of the resulting waves from the boundaries of the i-th grid cell. For this case, the wave $\mathcal{W}^2_{i-1/2}$ has moved a distance $\lambda^2\Delta t$ into the cell. The waves that will be averaged are $\mathcal{W}^2_{i-1/2}$, $\mathcal{W}^3_{i-1/2}$, and $\mathcal{W}^1_{i+1/2}$.

Then $\mathcal{Q}^{n+1}_i$ is determined only by the fluxes from cell boundaries $x = x_{i+1/2}$ and $x = x_{i-1}$. At the interface $x = x_{i+1/2}$, the waves $\mathcal{W}^p_{i+1/2}$ with negative $\lambda^p_{i+1/2}$ affect $\mathcal{Q}^{n+1}_i$, and similarly the waves $\mathcal{W}^p_{i-1/2}$ with positive $\lambda^p_{i+1/2}$ have influences on cell $\mathcal{C}_i$. We can summarize as follows,

$$\mathcal{Q}^{n+1}_i = \mathcal{Q}^n_i - \frac{\Delta t}{\Delta x}\left(\mathcal{A}^+\Delta\mathcal{Q}_{i-1/2} + \mathcal{A}^-\Delta\mathcal{Q}_{i+1/2}\right), \tag{3.7}$$

where

$$\mathcal{A}^-\Delta\mathcal{Q}_{i+1/2} = \sum_{p=1}^{m}(\lambda^p)^-\,\mathcal{W}^p_{i+1/2},$$
$$\mathcal{A}^+\Delta\mathcal{Q}_{i-1/2} = \sum_{p=1}^{m}(\lambda^p)^+\,\mathcal{W}^p_{i-1/2},$$

and

$$\lambda^+ = \max(\lambda, 0), \qquad \lambda^- = \min(\lambda, 0).$$

With this wave-propagation approach form, the cell average at the next time step $t = t_{n+1}$ is calculated directly without computing the integration. If the numerical scheme to be conservative, the following condition should be satisfied,

$$f(\mathcal{Q}_i) - f(\mathcal{Q}_{i-1}) = \mathcal{A}^- \Delta\mathcal{Q}_{i+1/2} + \mathcal{A}^+ \Delta\mathcal{Q}_{i-1/2}. \tag{3.8}$$

The wave propagation scheme satisfies the condition (3.8).

3.3 High Resolution Methods

The Godunov-type methods converge to entropy satisfying weak solutions, but they are only first-order accurate and numerically diffusive. Second-order schemes, such as the Lax-Wendroff scheme, are derived based on the Taylor expansion to the PDEs, but their solutions are spurious and inaccurate at the discontinuities. This problem can be improved if *limiters* can be applied in such a way that the discontinuities remain non-oscillatory and the smooth part continues to be accurate.

The wave propagation scheme (3.7) can be extended to a second-order accurate form,

$$\mathcal{Q}_i^{n+1} = \mathcal{Q}_i^n - \frac{\Delta t}{\Delta x}\left(\mathcal{A}^+ \Delta\mathcal{Q}_{i-1/2} + \mathcal{A}^- \Delta\mathcal{Q}_{i+1/2}\right) + \frac{\Delta t}{\Delta x}\left(\tilde{F}_{i-1/2} + \tilde{F}_{i+1/2}\right), \tag{3.9}$$

where the limited second-order correction flux $\tilde{F}_{i-1/2}$ is defined as

$$\tilde{F}_{i-1/2} = \frac{1}{2}\sum_{p=1}^{m} \left|s_{i-1/2}^p\right| \left(1 - \frac{\Delta t}{\Delta x}\left|s_{i-1/2}^p\right|\right) \tilde{\mathcal{W}}_{i-1/2}^p, \tag{3.10}$$

with $\tilde{\mathcal{W}}_{i-1/2}^p = \mathcal{W}_{i-1/2}^p \phi(\theta_{i-1/2}^p)$. In this expression $\phi(\theta_{i-1/2}^p)$ is a limiter function which will be defined in the following section.

3.3.1 Limiters

A limiter function is an interpretation of the smoothness of a solution so that the second-order correction term is applied for a smooth solution and it is not used for a discontinuous one. A limiter determines the smoothness from the local variations with the ratio of the jumps in $\mathcal{Q}_i^n$. For the scalar hyperbolic problems, the index I is chosen to the upwind

direction at the interface $x_{i-1/2}$,

$$I = \begin{cases} i-1, & \text{if} \quad s_{i-1/2} > 0, \\ i+1, & \text{if} \quad s_{i-1/2} < 0. \end{cases}$$

Then $\theta^n_{i-1/2}$ is defined to measure the smoothness as follows,

$$\theta^n_{i-1/2} = \frac{\Delta \mathcal{Q}^n_{I-1/2}}{\Delta \mathcal{Q}^n_{i-1/2}}.$$

It can be easily observed that $\theta^n_{i-1/2} \approx 1$ for smooth solutions and $\theta^n_{i-1/2} \approx 0$ for solutions with a steep gradient or discontinuity. From this, one possible choice of a limiter is

$$\phi(\theta) = \theta, \tag{3.11}$$

which is called *Beam-Warming* limiter.

Rather than focusing on the local variations, define the *total variation* of a numerical solution as

$$TV(\mathcal{Q}) = \sum_{i \in \mathcal{Z}_C} \left| \mathcal{Q}_i - \mathcal{Q}_{i-1} \right|.$$

A *total variation diminishing* (TVD) method satisfies $TV(\mathcal{Q}^{n+1}) \leq TV(\mathcal{Q}^n)$ when applied to a scalar problem. A limiter with TVD property can reduce the oscillations of solutions which Lax-Wendroff method exhibits.

For nonlinear system of conservation laws, a measure for the smoothness of a solution, $\theta^p_{i-1/2}$ can be defined as

$$\theta^p_{i-1/2} = \frac{\mathcal{W}^p_{I-1/2} \cdot \mathcal{W}^p_{i-1/2}}{\left| \mathcal{W}^p_{i-1/2} \right|^2}, \tag{3.12}$$

which measures local smoothness in the p-th field. A limiter function can be chosen as

$$\phi(\theta) = \max(0, \min(1, \theta)), \tag{3.13}$$

which is called as *minmod* limiter. Another choice of limiter is the *MC* limiter,

$$\phi(\theta) = \max(0, \min((1+\theta)/2, 2, \theta)). \tag{3.14}$$

It can be shown that the limiter functions (3.13) and (3.14) satisfies TVD property. For details, see Harten [65] and Sweby [128].

3.4 CFL number

The CFL condition is a necessary condition for stability, which requires the numerical domain of dependency should include the true domain of dependency. In the wave propagation methods, the time step satisfy

$$\frac{\max_p(|s^p_{i-1/2}|)\Delta t}{\Delta x} \leq 1 \tag{3.15}$$

at every cell interface.

3.5 Approximate Riemann Solvers

The second step of the Godunov-type methods involves solving Riemann problem for every time step and every cell interface. In the wave propagation algorithms, only small portion of the Riemann solution is utilized for the computation of the fluxes. Even for the higher order accurate methods, the potion of utilized information from Riemann solutions are very small. Thus many research have been seeking for approximate Riemann solvers that do not require full structures of Riemann problems.

One natural approach is, for a given non-linear PDE $q_t + f'(q)_x = 0$, to find a linearized equation

$$\hat{q}_t + \hat{A}_{i-1/2}\hat{q}_x = 0, \tag{3.16}$$

where $\hat{A}_{i-1/2}$ is a matrix that is chosen to be some approximation to $f'(q)$ valid in a neighborhood of $\mathcal{Q}_i$ and $\mathcal{Q}_{i-1}$. Since the system is hyperbolic, we require $\hat{A}_{i-1/2}$ to be diagonalizable with real eigenvalues. For the consistency with the original conservation law, we require

$$\hat{A}_{i-1/2} \to f'(\bar{q}), \quad \text{as} \quad \mathcal{Q}_i, \mathcal{Q}_{i-1} \to \bar{q}. \tag{3.17}$$

3.5.1 Roe Linearization

One of the notable approximate Riemann solvers is *Roe linearization*. It came from the observation that Riemann problems arising at cell interfaces. With (3.16) and (3.17), Roe

linearization requires another condition

$$\hat{A}_{i-1/2}(\mathcal{Q}_i - \mathcal{Q}_{i-1}) = f(\mathcal{Q}_i) - f(\mathcal{Q}_{i-1}). \tag{3.18}$$

For the shallow water equations, the choices of Roe average are

$$\hat{A}_{i-1/2} = \begin{bmatrix} 0 & 1 \\ -\tilde{u}^2 + g\bar{h} & 2\tilde{u} \end{bmatrix},$$

where

$$\tilde{u} = \frac{\sqrt{h_{i-1}}u_{i-1} + \sqrt{h_i}u_i}{\sqrt{h_{i-1}} + \sqrt{h_i}}, \quad \bar{h} = \frac{h_{i-1} + h_i}{2}.$$

It can be easily shown that these choices satisfy (3.16), (3.17) and (3.18). And the Roe solver produces exact solutions when two states are connected by a single shock wave because the Rankin-Hugoniot condition is satisfied.

The numerical methods based on the Roe averages may yield non-physical solutions in strong rarefaction cases where a dry state should arise. In these situations, the solutions from Roe solvers may yield negative values for the height of the water. To overcome this disadvantage, other numerical methods are investigated.

3.5.2 HLLE solver

Another class of approximate Rieman solvers was introduced by Harten, Lax and van Leer [66] and extended by Einfeldt [37]. *HLLE* solvers assume that there are only two waves that connect the left and right state. Then HLLE solvers use a single state $\hat{\mathcal{Q}}_{i-1/2}$ such that

$$\mathcal{W}^1_{i-1/2} = \hat{\mathcal{Q}}_{i-1/2} - \mathcal{Q}_{i-1}, \quad \text{and} \quad \mathcal{W}^2_{i-1/2} = \mathcal{Q}_i - \hat{\mathcal{Q}}_{i-1/2}.$$

We require the approximate solver to be conservative so that

$$s^1_{i-1/2}\left(\hat{\mathcal{Q}}_{i-1/2} - \mathcal{Q}_{i-1}\right) + s^2_{i-1/2}\left(\mathcal{Q}_i - \hat{\mathcal{Q}}_{i-1/2}\right) = f(\mathcal{Q}_i) - f(\mathcal{Q}_{i-1}),$$

and thus

$$\hat{\mathcal{Q}}_{i-1/2} = \frac{f(\mathcal{Q}_i) - f(\mathcal{Q}_{i-1}) - s^2_{i-1/2}\mathcal{Q}_i + s^1_{i-1/2}\mathcal{Q}_{i-1}}{s^1_{i-1/2} - s^2_{i-1/2}}$$

The HLLE solvers suggest the choices for the wave speed $s^1_{i-1/2}$ and $s^2_{i-1/2}$ as

$$s^1_{i-1/2} = \min_p \left(\min \left(\lambda^p_{i-1}, \hat{\lambda}^p_{i-1/2} \right) \right),$$
$$s^2_{i-1/2} = \max_p \left(\max \left(\lambda^p_{i}, \hat{\lambda}^p_{i-1/2} \right) \right),$$

where $\hat{\lambda}^p_{i-1/2}$ are the eigenvalues of $\hat{A}$ using Roe averages. If the *HLLE* scheme is applied to the 1-dimension shallow water system, the wave speeds are simply

$$s^1_{i-1/2} = \min \left(\lambda^1_{i-1}, \hat{\lambda}^1_{i-1/2} \right),$$
$$s^2_{i-1/2} = \max \left(\lambda^2_{i}, \hat{\lambda}^2_{i-1/2} \right).$$

We can easily show that this choice of the wave speeds always gives non-negative solutions. See George [48] for details.

3.6 Numerical Treatments of Source Terms

There are many situations in which source terms appear with the conservation laws, giving an equation of the form,

$$q_t + f(q)_x = \psi(q). \tag{3.19}$$

The equation (3.19) is often called *balance law*. In this section, several numerical schemes will be discussed to solve the balance law.

3.6.1 Fractional Step Method

The *fractional step method* separates the system into two systems

$$q_t + f(q)_x = 0,$$

and

$$q_t = \psi(q).$$

Then the solution q is updated in alternating steps. This method is simple and allows easy extension to the high-resolution methods by using the Strang splitting.

3.6.2 Godunov and Strang Splitting

Consider a more general PDE

$$q_t = (\mathcal{A} + \mathcal{B})q,$$

where $\mathcal{A}$ and $\mathcal{B}$ are differential operators. In *Godunov splitting*, we first update

$$q^* = e^{\mathcal{A}\Delta t} q(x, 0), \tag{3.20}$$

then

$$q^{**} = e^{\mathcal{B}\Delta t} q^* = e^{\mathcal{B}\Delta t} e^{\mathcal{A}\Delta t} q(x, 0). \tag{3.21}$$

This Godunov splitting is $\mathcal{O}(\Delta t)$ accuracy in general. Second order accuracy can be obtained by solving the first problem $q_t = \mathcal{A}q$ over $\Delta t/2$, and the second problem $q_t = \mathcal{B}q$ over Δt. Then the first problem is solved again over $\Delta t/2$. In summary, we update by

$$q^* = e^{\mathcal{A}\Delta t/2} e^{\mathcal{B}\Delta t} e^{\mathcal{A}\Delta t/2} q(x, 0).$$

This scheme is called *Strang splitting*.

3.6.3 Shallow Water Equations

If the source term depends on the derivative of q with respect to x, the steady state may not be easily preserved with a fractional step method. For example, consider shallow water equations with bathymetry $b(x)$,

$$h_t + (hu)_x = 0, \tag{3.22}$$

$$(hu)_t + \left(hu^2 + \frac{1}{2} g h^2 \right)_x = -ghb_x. \tag{3.23}$$

When $(hu)_x \equiv 0$ and $\left(hu^2 + \frac{1}{2}gh^2\right)_x \equiv -ghb_x$, the steady states are preserved. If the fractional step method is used, the splitting error can cause spurious waves to form near bathymetry jumps and can quickly dominate the solution in practical problems. Because preserving the balance between $\left(hu^2 + \frac{1}{2}gh^2\right)_x$ and $-ghb_x$ is computational nontrivial when these terms are large. One of the possible schemes to circumvent this issue is *f-wave* scheme.

3.7 f-wave Scheme

3.7.1 f-wave Propagation Form

An alternative form is suggested by Bale, LeVeque, Mitran and Rossmanith [10], and we split the jump in flux into *f-waves* $\mathcal{Z}^p_{i-1/2}$ as

$$f(\mathcal{Q}_i) - f(\mathcal{Q}_{i-1}) = \sum_{p=1}^{m} \mathcal{Z}^p_{i-1/2}. \tag{3.24}$$

Each *f-wave* $\mathcal{Z}^p$ moves at the speed of s^p. In a linearized Riemann solver, the flux difference are decomposed with eigenvcetors $\hat{r}^p_{i-1/2}$ of $\hat{A}_{i-1/2}$.

$$f(\mathcal{Q}_i) - f(\mathcal{Q}_{i-1}) = \sum_{p=1}^{m} \beta^p_{i-1/2} \hat{r}^p_{i-1/2} \equiv \sum_{1}^{m} \mathcal{Z}^p_{i-1/2}, \tag{3.25}$$

where the coefficients $\beta^p_{i-1/2}$ are

$$\beta_{i-1/2} = R^{-1}_{i-1/2} \left(f(\mathcal{Q}_i) - f(\mathcal{Q}_{i-1}) \right),$$

with the matrix of right eigenvectors $R_{i-1/2}$. Then the fluctuations can be defined as

$$\mathcal{A}^- \Delta \mathcal{Q}_{i+1/2} = \sum_{\{p: s^p_{i+1/2} < 0\}} \mathcal{Z}^p_{i+1/2}, \tag{3.26}$$

$$\mathcal{A}^+ \Delta \mathcal{Q}_{i-1/2} = \sum_{\{p: s^p_{i-1/2} > 0\}} \mathcal{Z}^p_{i-1/2} \tag{3.27}$$

If all of the speeds are nonzero, this decomposition will maintain conservation since the condition (3.8) is satisfied. The *f-wave* scheme has an advantage in problems with source terms when they are close to the steady state.

3.7.2 f-wave Scheme for the Balance Law

One of the alternative schemes for balance laws is *f-wave* method suggested by Bale, LeVeque, Mitran and Rossmanith [10]. The *f-wave method* uses the source term to modify the flux difference before performing the wave decomposition,

$$f(\mathcal{Q}_i) - f(\mathcal{Q}_{i-1}) - \Delta x \Psi_{i-1/2} = \sum_{p=1}^{m} \beta^p_{i-1/2} r^p_{i-1/2},$$

where

$$\Delta x \Psi_{i-1/2} \approx \int \psi(q,x)dx.$$

An ambiguity of f-wave scheme lies in the choice of the approximation to the source term which can be understood as the choice of paths in the Dal Maso LeFloch and Murat theory [98]. The *DLM theory* claims that the choice of path connecting $\mathcal{Q}_{i-1}$ and $\mathcal{Q}_i$ is not uniquely determined. In the next chapter, the DLM theory will be discussed in detail in the context of the multi-layer shallow water system.

To implement the *f-wave* method with the shallow water equations, we need to determine the approximation of the source term, $\int ghb_x dx$. One simple choice is to take the average so that

$$\int ghb_x dx \approx g\frac{h_{i-1}+h_i}{2}\left(b_i - b_{i-1}\right).$$

This choice can be interpreted as a straight line path in DLM theory, and it is sufficient to maintain steady states.

George [48, 49] suggested an alternative approximation where the derivation is based smooth steady states,

$$\int ghb_x dx \approx g\frac{h_{i-1}+h_i}{2}\frac{\widetilde{\lambda_1\lambda_2}}{\overline{\lambda_1\lambda_2}}\left(b_i - b_{i-1}\right),$$

where

$$\widetilde{\lambda_1\lambda_2} = -\left(-u_{i-1}u_i + g\left(\frac{h_{i-1}+h_i}{2}\right)\right),$$

and

$$\overline{\lambda_1\lambda_2} = -\left(-\left(\frac{u_{i-1}+u_i}{2}\right)^2 + g\left(\frac{h_{i-1}+h_i}{2}\right)\right).$$

From numerical tests, George [49] showed that this shallow water solver easily maintains steady states with small perturbations, and also handles the dry state.

Chapter 4

MULTI-LAYER SHALLOW WATER EQUATIONS

In this chapter, we review the derivation of multi-layer shallow water equations, and explore numerical schemes for this system.

4.1 Derivation of the two layer shallow water equations

We denote by $z = b(x, y, t)$ for bottom topography, and let $h_1(x, y, t)$ and $h_2(x, y, t)$ stand for the depth of the upper and lower layer respectively. Let the free surface boundary be $z = \eta_1(x, y, t)$ and the interface between the two layers as $z = \eta_2(x, y, t)$. By our notation, $\eta_1(x, y, t) = b(x, y, t) + h_2(x, y, t) + h_1(x, y, t)$ and $\eta_2(x, y, t) = b(x, y, t) + h_2(x, y, t)$. With the fluid speed $\mathbf{u} = (u, v, w)$, the incompressibility condition for the flow states that $\nabla \cdot \mathbf{u} = 0$,

$$\frac{\partial u}{\partial x} + \frac{\partial v}{\partial y} + \frac{\partial w}{\partial z} = 0. \tag{4.1}$$

Neglecting the viscous terms, the incompressible Navier-Stokes equation reads

$$\rho \left(\frac{\partial \mathbf{u}}{\partial t} + \mathbf{u} \cdot \nabla \mathbf{u} \right) = -\nabla p + \rho \mathbf{g}, \tag{4.2}$$

where $\mathbf{g} = (0, 0, -g)$. This equation (4.2) is the Euler equations. The Euler equations are simplified by the hydrostatic assumption,

$$\frac{\partial p}{\partial z} = -\rho g, \quad \text{and} \quad u_z = v_z = 0.$$

For the two layer case, the density $\rho(z)$ is piecewise constant. With the density of the upper layer ρ_1 and lower layer ρ_2, the density $\rho(\mathbf{x}; z)$ is given as,

$$\rho(\mathbf{x}; z) = \begin{cases} \rho_1, & \text{if } \eta_2(\mathbf{x}) \le z \le \eta_1(\mathbf{x}), \\ \rho_2, & \text{if } b(\mathbf{x}) \le z \le \eta_2(\mathbf{x}). \end{cases}$$

Thus the pressure $p(\mathbf{x}; z)$ is

$$p(\mathbf{x}; z) = \begin{cases} \rho_1 g(\eta_1 - z), & \text{if } \eta_2 \le z \le \eta_1, \\ \rho_1 g(\eta_1 - \eta_2) + \rho_2 g(\eta_2 - z), & \text{if } b \le z \le \eta_2. \end{cases}$$

For an arbitrary area A in the x-y plane, we define the control volume V_k as follows,

$$V_1 = \{(x,y,z)|(x,y) \in A, \quad \eta_2(x,y,t) \le z(x,y,t) \le \eta_1(x,y,t)\},$$
$$V_2 = \{(x,y,z)|(x,y) \in A, \quad b(x,y,t) \le z(x,y,t) \le \eta_2(x,y,t)\}.$$

The conservation of mass for the control volume V_k reads

$$\frac{\partial}{\partial t}\int_{V_k} \rho_k = -\int_{\partial V_k} \rho_k \mathbf{u}_k \cdot \mathbf{n}, \quad k = 1,2,$$

where $\mathbf{n} = (n_x, n_y, n_z)$ is the normal vector of the surface, and $\mathbf{u}_k(x,y,z,t) = (u_k, v_k, w_k)$ is the speed of each layer. Since the density ρ_k is constant within each layer and $w_k \cdot n_z = 0$, vertical integration yields,

$$\frac{\partial}{\partial t}\int_A h_k = -\int_{\partial A} h_k \mathbf{u}_k \cdot \mathbf{n} = -\int_{\partial A} h_k \mathbf{u}_k^{\perp} \cdot \mathbf{n}^{\perp}, \tag{4.3}$$

where $\mathbf{u}_k^{\perp}(x,y,t) = (\bar{u}_k, \bar{v}_k)^T$ is the depth averaged speed and $\mathbf{n}^{\perp} = (n_x, n_y)^T$. The equation (4.3) implies that the mass is conserved in each layer.

Next we consider the momentum equation for each layer. For the upper layer, we divide the cylindrical boundary of ∂V into three components,

$$\partial V_1 = \partial V_{s_1} \cup \partial V_{\eta_1} \cup \partial V_{\eta_2},$$

where ∂V_{s_1}, ∂V_{η_1} and ∂V_{η_2} are the vertical, upper and lower surface area of the cylinder ∂V respectively. Then the momentum equation is given by

$$\frac{\partial}{\partial t}\int_{V_1} \rho \mathbf{u}^{\perp} = -\int_{\partial V_{s_1}} \rho \mathbf{u}^{\perp}(\mathbf{u}\cdot\mathbf{n}) - \int_{\partial V_{s_1}} p\mathbf{n}^{\perp} - \int_{\partial V_{\eta_2}} p\mathbf{n}^{\perp} + \int_{\partial V_{\eta_1}} p\mathbf{n}^{\perp},$$

where $p(\mathbf{x})$ is the pressure. Since we assume the pressure at the surface η_1 is zero, that is, ignoring the atmospheric pressure, we have

$$\frac{\partial}{\partial t}\int_{V_1} \rho \mathbf{u}^{\perp} = -\int_{\partial V_{s_1}} \rho \mathbf{u}^{\perp}(\mathbf{u}\cdot\mathbf{n}) - \int_{\partial V_{s_1}} p\mathbf{n}^{\perp} - \int_{\partial V_{\eta_2}} p\mathbf{n}^{\perp}.$$

We integrate vertically from $z = \eta_2$ to $z = \eta_1$ with $h_1 = \eta_1 - \eta_2$, then we obtain,

$$\begin{aligned}\frac{\partial}{\partial t}\int_A \rho_1 h_1 \mathbf{u}_1^{\perp} &= -\int_{\partial A} \rho_1 h_1 \mathbf{u}_1^{\perp}(\mathbf{u}_1^{\perp}\cdot\mathbf{n}^{\perp}) - \int_{\partial V_{s_1}} \rho_1 g(\eta_1 - z)\mathbf{n}^{\perp} - \int_{\partial V_{\eta_2}} \rho_1 g(\eta_1 - z)\mathbf{n}^{\perp} \\ &= -\int_{\partial A} \rho_1 h_1 \mathbf{u}_1^{\perp}(\mathbf{u}_1^{\perp}\cdot\mathbf{n}^{\perp}) - \int_{\partial A} \frac{\rho_1}{2} g h_1^2 \mathbf{n}^{\perp} - \int_A \rho_1 g h_1 \nabla^{\perp}\eta_2. \end{aligned} \tag{4.4}$$

The last integral is a surface integral with $\nabla^{\perp}\eta_2 = (\frac{\partial \eta_2}{\partial x}, \frac{\partial \eta_2}{\partial y})^T$. Thus we obtain the momentum equation for the upper layer, and the momentum is not conserved but coupled with the momentum of the lower layer.

Similarly we derive the momentum equation of the lower layer including the pressure gradient from the upper layer onto lower layer. Thus the momentum equation is

$$\frac{\partial}{\partial t}\int_{V_2} \rho_2 \mathbf{u}_2^{\perp} = -\int_{\partial V_{s_2}} \rho_2 \mathbf{u}_2^{\perp}(\mathbf{u}_2 \cdot \mathbf{n}) - \int_{\partial V_{s_2}} P\mathbf{n}^{\perp} - \int_{\partial V_b} P\mathbf{n}^{\perp} + \int_{\partial V_{\eta_2}} P\mathbf{n}^{\perp}.$$

And the vertical integration from $z = b$ to $z = \eta_2$ yields

$$\begin{aligned}
\frac{\partial}{\partial t}\int_A \rho_2 h_2 \mathbf{u}_2^{\perp} =& -\int_{\partial A} \rho_2 h_2 \mathbf{u}_2^{\perp}(\mathbf{u}_2^{\perp} \cdot \mathbf{n}^{\perp}) - \int_{\partial V_{s_2}} (\rho_1 g h_1 + \rho_2 g(\eta_2 - z))\mathbf{n}^{\perp} \\
& - \int_{\partial V_b} (\rho_1 g h_1 + \rho_2 g(\eta_2 - z))\mathbf{n}^{\perp} + \int_{\partial V_{\eta_2}} (\rho_1 g h_1 + \rho_2 g(\eta_2 - z))\mathbf{n}^{\perp} \\
=& -\int_{\partial A} \rho_2 h_2 \mathbf{u}_2^{\perp}(\mathbf{u}_2^{\perp} \cdot \mathbf{n}^{\perp}) - \int_{\partial V_{s_2}} (\rho_1 g h_1 h_2 + \frac{1}{2}\rho_2 g h_2^2)\mathbf{n}^{\perp} \\
& - \int_A (\rho_1 g h_1 \nabla^{\perp} b + \rho_2 g h_2 \nabla^{\perp} b) + \int_A \rho_1 g h_1 \nabla^{\perp}\eta_2. \\
=& -\int_{\partial A} \rho_2 h_2 \mathbf{u}_2^{\perp}(\mathbf{u}_2^{\perp} \cdot \mathbf{n}^{\perp}) - \int_{\partial A} (\frac{g}{2}\rho_2 h_2^2 + \rho_1 g h_1 h_2)\mathbf{n}^{\perp} \\
& - \int_A \rho_2 g h_2 \nabla^{\perp} b + \int_A \rho_1 g h_1 \nabla^{\perp}(\eta_2 - b). \qquad (4.5)
\end{aligned}$$

Combining (4.4) and (4.5) yields,

$$\frac{\partial}{\partial t}\int_A q + \int_{\partial A} f(q) n_x + \int_{\partial A} g(q) n_y = \int_A \psi,$$

where

$$q = \begin{bmatrix} h_1 \\ h_1 u_1 \\ h_1 v_1 \\ h_2 \\ h_2 u_2 \\ h_2 v_2 \end{bmatrix}, \quad f(q) = \begin{bmatrix} h_1 u_1 \\ h_1 u_1^2 + \frac{1}{2} g h_1^2 \\ h_1 u_1 v_1 \\ h_2 u_2 \\ h_2 u_2^2 + \frac{1}{2} g h_2^2 \\ h_2 u_2 v_2 \end{bmatrix}, \quad g(q) = \begin{bmatrix} h_1 v_1 \\ h_! u_1 v_1 \\ h_1 v_1^2 + \frac{1}{2} g h_1^2 \\ h_2 v_2 \\ h_2 u_2 v_2 \\ h_2 v_2^2 + \frac{1}{2} g h_2^2 \end{bmatrix},$$

and

$$\psi = \begin{bmatrix} 0 \\ -gh_1(h_2+b)_x \\ -gh_1(h_2+b)_y \\ 0 \\ -gh_2(rh_1+b)_x \\ -gh_2(rh_1+b)_y \end{bmatrix},$$

where $r = \rho_1/\rho_2$.

4.2 Quai-linear Form of the Two-Layer Shallow Water System

Consider the 1-dimensional case. The two layer shallow water system is derived as follows,

$$q_t + f(q)_x = \psi,$$

where

$$q = \begin{bmatrix} h_1 \\ h_1u_1 \\ h_2 \\ h_2v_2 \end{bmatrix}, \quad f(q) = \begin{bmatrix} h_1u_1 \\ h_1u_1^2 + \frac{1}{2}gh_1^2 \\ h_2u_2 \\ h_2u_2^2 + \frac{1}{2}gh_2^2 \end{bmatrix}, \quad \text{and} \quad \psi = \begin{bmatrix} 0 \\ -gh_1(h_2+b)_x \\ 0 \\ -gh_2(rh_1+b)_x \end{bmatrix}.$$

We observe that this system bears source terms which contain the derivative of variables. One approach is to solve the hyperbolic system first, and include all the source terms using a splitting method. For example, Audusse [9] and Chen and Peng [26] used this approach to solve the two-layer shallow water system. Although this scheme can hinder the possibility of being non-hyperbolic, it does not represent the correct speeds of the internal waves, and thus does not preserve steady states.

Relocating the x-derivative terms on the right hand side to the left hand side, we obtain a quasi-linear form,

$$q_t + A(q)q_x = \phi(q), \tag{4.6}$$

where

$$A(q) = \begin{bmatrix} 0 & 1 & 0 & 0 \\ gh_1 - u_1^2 & 2u_1 & gh_1 & 0 \\ 0 & 0 & 0 & 1 \\ rgh_2 & 0 & gh_2 - u_2^2 & 2u_2 \end{bmatrix}, \quad \phi(q) = \begin{bmatrix} 0 \\ -gh_1 b_x \\ 0 \\ -gh_2 b_x \end{bmatrix}. \tag{4.7}$$

Note that $A(q) \neq \partial f(q)/\partial x$.

4.3 Eigenstructure

4.3.1 Eigenvalue

The characteristic polynomial of $A(q)$ is,

$$p(x) = ((x-u_1)^2 - gh_1)((x-u_2)^2 - gh_2) - rg^2 h_1 h_2. \tag{4.8}$$

Since the roots of this quartic equation (4.8) cannot be found explicitly, several approaches have been suggested to find approximation to the real solutions.

Algebraic interpretation

The discriminant of the following quartic equation

$$a_4 x^4 + a_3 x^3 + a_2 x^2 + a_1 x + a_0 = 0,$$

is

$$\begin{aligned} D_4 =& [(a_1^2 a_2^2 a_3^2 - 4a_1^3 a_3^3 - 4a_1^2 a_2^3 a_4 + 18 a_1^3 a_2 a_3 a_4 - 27 a_1^4 a_4^2 + 256 a_0^3 a_4^3) \\ &+ a_0(-4a_2^3 a_3^2 + 18 a_1 a_2 a_3^3 + 16 a_2^4 a_4 - 80 a_1 a_2^2 a_3 a_4 - 6 a_1^2 a_3^2 a_4 + 144 a_1^2 a_2 a_4^2) \\ &+ a_0^2(-27 a_3^4 + 144 a_2 a_3^2 a_4 - 128 a_2^2 a_4^2 - 192 a_1 a_3 a_4^2)]. \end{aligned}$$

If $D_4 > 0$, then the quartic equation has four real roots or four complex roots. Otherwise if $D_4 < 0$, then it has two real roots and two complex roots. Since $p(u_1 + \sqrt{gh_1}) < 0$, $p(u_2 + \sqrt{gh_2}) < 0$ and $p(x) \to \infty$ as $|x| \to \infty$, the equation (4.8) always has at least two real roots. Therefore, $D_4 > 0$ implies that this quartic equation has four real roots, and can be used as a criterion for the hyperbolicity of the system.

Approximate expression

Under the assumptions that $|u_1 - u_2|$ and $(1 - r)$ are very small ($\ll 1$), first order approximation for the eigenvalues can be found as follows,

$$\lambda_{ext}^{\pm} = U_m \pm \sqrt{g(h_1 + h_2)} \tag{4.9}$$

$$\lambda_{int}^{\pm} = U_c \pm \sqrt{g' \frac{h_1 h_2}{h_1 + h_2} \left[1 - \frac{(u_2 - u_1)^2}{g'(h_1 + h_2)}\right]}, \tag{4.10}$$

where

$$U_m = \frac{h_1 u_1 + h_2 u_2}{h_1 + h_2}, \quad U_c = \frac{h_1 u_2 + h_2 u_1}{h_1 + h_2}, \tag{4.11}$$

and $g' = g(1 - r)$ is the reduced gravity. Two eigenvalues $\lambda_{ext}^{\pm}$ are real, and comparable to the two waves of the single-layer shallow water equations if $h_1 + h_2$ are considered as the depth of water. Meanwhile two eigenvalues $\lambda_{int}^{\pm}$ are conditionally real if

$$\frac{(u_2 - u_1)^2}{g'(h_1 + h_2)} < 1. \tag{4.12}$$

If these eigenvalues $\lambda_{int}^{\pm}$ are imaginary, the system is not hyperbolic. The notation λ_{int} stands for the internal wave which is associated with stratified fluids with different uniform densities also known as barotropic modes, while λ_{ext} are the wave speeds of surface waves, or baroclinic modes. If $|u_2 - u_1|$ becomes large enough, the shear stress grows and can be expected to lead to a growing Kelvin-Helmholtz instability in the full problem, which results in the loss of hyperbolicity in these depth-averaged equations.

Geometric interpretation

Another way to interpret the eigenvalues is with a geometric approach that was suggested by Ovsyannikov [111]. If we set,

$$z = x - u_1 \quad \text{and} \quad w = x - u_2, \tag{4.13}$$

then $p(x) = 0$ from (4.8) reads

$$(z^2 - gh_1)(w^2 - gh_2) - rg^2 h_1 h_2 = 0. \tag{4.14}$$

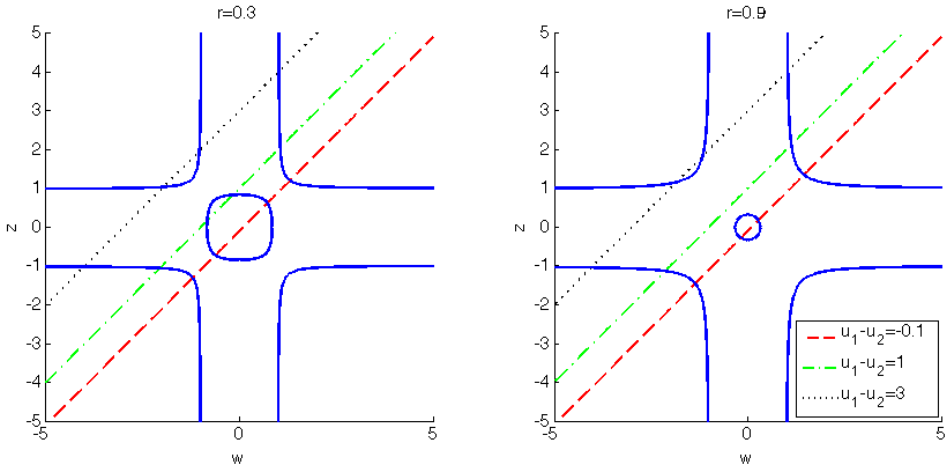

Figure 4.1: Graphs of (4.14) and (4.15) are given for different values of $r = 0.3$ and $r = 0.9$. The solid lines are the graph for (4.14). The dashed, dash-dot and dotted lines are the graphs for (4.15) with $u_1 - u_2 = -0.1$, 1 and 3 respectively. Values are fixed as $h_1 = h_2 = g = 1$ for this graph.

Eliminating x from (4.13) yields,

$$w = z + (u_1 - u_2). \tag{4.15}$$

The Figure 4.1 is the graph of (4.14) and (4.15) for different values of r, and fixed values of $h_1 = h_2 = g = 1$. Figure 4.1 shows two cases for the values $r = 0.3$ and $r = 0.9$ respectively. The solid curves represent solutions of (4.14) and the dashed, dash-dot and dotted lines denote (4.15) with $u_1 - u_2 = -0.1$, 1 and 3 respectively. When $h_1 = h_2$, the shape of the central part is close to a circle with radius $\sqrt{(1-r)gh_1}$. If $h_1 \neq h_2$, then the shape of the curve around the origin is close to an ellipse.

The roots of the characteristic polynomial (4.8) are the intercepts of the dashed line and solid curves. When $|u_1 - u_2|$ is sufficiently small, four real solutions exist. Two of them are interceptions with the outer curves and they correspond to $\lambda^{\pm}_{ext}$. The others are interceptions with the inner closed curve, and correspond to $\lambda^{\pm}_{int}$. This is the case of dashed line in Figure 4.1. But the dash-dot line on the right figure has only two intercepts with

the solid curves which indicates the loss of hyperbolicity. Even if $|u_1 - u_2|$ is very large, there can be four real roots which is observed for the dotted lines in Figure 4.1. However this must be excluded because it is not a physically reasonable case.

The hyperbolicity condition should be determined by the existence of the interceptions with the inner part. If $r \approx 1$, then the central parts can be regarded as an ellipse with two axes of length $\sqrt{g'h_1}$ and $\sqrt{g'h_2}$. Then simple calculation yields the hyperbolicity condition which is exactly the same as (4.12). If $r \ll 1$, then the shape of the central part is similar to a square, and the hyperbolicity condition can be found as follows,

$$\frac{|u_2 - u_1|}{\sqrt{g'h_1} + \sqrt{g'h_2}} < 1. \tag{4.16}$$

The conditions for the hyperbolicity of the system can analytically be found for special cases. When $h_1 = h_2 = h$, the characteristic polynomial is quadratic. If the following condition is satisfied,

$$2\left(gh(1-\sqrt{r})\right)^{1/2} < (u_2 - u_1)^2 < 2\left(gh(1+\sqrt{r})\right)^{1/2},$$

the problem is non-hyperbolic. To make sense physically, right inequality should be disregarded. When $r = 1$, the original one layer shallow water equation will be recovered and, therefore, the problem is non-hyperbolic if

$$0 < (u_2 - u_1)^2 < \left((gh_1)^{1/3} + (gh_2)^{1/3}\right)^3,$$

which indicates that it is ill-posed whenever the speeds of the two layers are different. Therefore, the two-layer shallow water equations with $\rho_1 = \rho_2$ are ill-posed.

4.3.2 Eigenvector

Once the eigenvalues are found computationally, the eigenvectors can be found easily. Let λ^k be an eigenvalue of the two layer shallow water system given by (4.6) and (4.7). Then the corresponding eigenvector r^k is given by,

$$r^k = \begin{bmatrix} 1 \\ \lambda^k \\ c_k \\ c_k\lambda^k \end{bmatrix},$$

where c_k is given by

$$c_k = -1 + \frac{(\lambda^k - u_1)^2}{gh_1}.$$

4.4 Hyperbolicity

When the difference between the speeds of the two layers is large, the two-layer shallow water system loses hyperbolicity. By reducing the difference, the system can regain hyperbolicity, but may be inconsistent with the physical situation. One method is to introduce an additional layer between two layers when the system becomes non-hyperbolic. See, for example, Frings et al.[21]. The speed of the new layer should be a value between the speeds of the pre-existing two layers, and the depth is determined in relation to the imaginary part of the eigenvalues. The new system can still lose the hyperbolicity, and this requires another layer, which lowers the efficiency.

Another approach to alleviate the hyperbolicity condition is to introduce friction terms. When the system is non-hyperbolic, the speeds of the layers are modified so that the difference of velocities become smaller until the system retains the hyperbolicity. For viscous fluid, the friction coefficient is related with the Reynolds number by the Moody's diagram [105]. Thus the local mixing of two layers can be reinterpreted as friction forces as long as the instability is localized.

4.5 Numerical scheme for multi-layer shallow water system

Consider a quasi-linear system given as,

$$\mathbf{q}_t + A(\mathbf{q})\mathbf{q}_x = 0, \tag{4.17}$$

where $\mathbf{q} = \mathbf{q}(x,t)$. The equation (4.17) is *conservative* if it can be written as $\mathbf{q}_t + f(\mathbf{q})_x = 0$ for some $f(\mathbf{q})$, and *non-conservative* otherwise. If the system is conservative, *Rankine-Hugoniot* jump condition can be applied to find shock speeds. If it is non-conservative, however, finding the shock condition becomes non-trivial. There have been many theoretical efforts to figure out this condition, and the following *Dal Maso, LeFloch, and Murat(DLM)* theory is one of them.

4.5.1 DLM families of paths and nonconservative products

According to Dal Maso, LeFloch, and Murat(DLM), a shock wave theory for a non-conservative system requires a prescribed family of paths. Details of the DLM theory can be found in Dal Maso et al. [98] and Castro et al. [24], for example. Let Ω be an open subset of $\mathbb{R}^n$. The set of functions of bounded variation and locally bounded variation on Ω will be denoted by $BV(\Omega)$ and $BV_{loc}(\Omega)$, respectively. We define the families of paths as follows.

Definition A path Φ in $\Omega \subset \mathbb{R}^N$ is a family of smooth maps $[0,1] \times \Omega \times \Omega \to \Omega$ satisfying:

- $\Phi(0; \mathbf{q}_{i-1}, \mathbf{q}_i) = \mathbf{q}_{i-1}$ and $\Phi(1; \mathbf{q}_{i-1}, \mathbf{q}_i) = \mathbf{q}_i$,
- $\forall V \subset \Omega$, $\exists k$ such that $\left|\frac{\partial \Phi}{\partial s}(s; \mathbf{q}_{i-1}, \mathbf{q}_i)\right| \leq k|\mathbf{q}_{i-1} - \mathbf{q}_i|$, for any $\mathbf{q}_{i-1}, \mathbf{q}_i \in V$ and almost every $s \in [0,1]$,
- $\forall V \subset \Omega$, $\exists K$ such that $\left|\frac{\partial \Phi}{\partial s}(s; \mathbf{q}^1_{i-1}, \mathbf{q}^1_i) - \frac{\partial \Phi}{\partial s}(s; \mathbf{q}^2_{i-1}, \mathbf{q}^2_i)\right| \leq K\left(|\mathbf{q}^1_{i-1} - \mathbf{q}^2_{i-1}| + |\mathbf{q}^1_i - \mathbf{q}^2_i|\right)$, for any $\mathbf{q}^1_{i-1}, \mathbf{q}^1_i, \mathbf{q}^2_{i-1}$, and $\mathbf{q}^2_i \in V$ and almost every $s \in [0,1]$.

We require that a shock joining the states $\mathbf{q}_{i-1}$ and $\mathbf{q}_i$ and propagating with speed s must satisfy the jump condition,

$$s(\mathbf{q}_i - \mathbf{q}_{i-1}) = \int_0^1 A(\Phi(t; \mathbf{q}_{i-1}, \mathbf{q}_i))\partial_t \Phi(t; \mathbf{q}_{i-1}, \mathbf{q}_i) dt. \tag{4.18}$$

If the system is conservative, $A(\mathbf{q})\mathbf{q}_x = f(\mathbf{q})_x$, then the right hand side of equation (4.18) is,

$$\int_0^1 A(\Phi(t; \mathbf{q}_{i-1}, \mathbf{q}_i))\partial_t \Phi(t; \mathbf{q}_{i-1}, \mathbf{q}_i) dt = f(\mathbf{q}_i) - f(\mathbf{q}_{i-1}),$$

which is independent of $\Phi(t; \mathbf{q}_{i-1}, \mathbf{q}_i)$. Thus we recover the Rankine-Hugoniot jump condition for any choice of the path.

If the system is non-conservative, the shock speed depends on the choice of paths. The choice of path $\Phi(t; \mathbf{q}_{i-1}, \mathbf{q}_i)$ is not unique, and the shock speed cannot be uniquely determined.

4.5.2 SIngle layer shallow water equations and f-wave method

First consider the single layer shallow water equations with bottom topography,

$$\mathbf{q}_t + \mathbf{f}(\mathbf{q})_x = \Psi(\mathbf{q}),$$

where

$$\mathbf{q} = \begin{bmatrix} h \\ hu \\ b \end{bmatrix}, \quad \mathbf{f}(\mathbf{q}) = \begin{bmatrix} hu \\ hu^2 + \frac{1}{2}gh^2 \\ 0 \end{bmatrix}, \quad \text{and} \quad \Psi(\mathbf{q}) = \begin{bmatrix} 0 \\ -ghb_x \\ 0 \end{bmatrix}.$$

The *f-wave* method decomposes the flux difference $f(\mathbf{q}_i) - f(\mathbf{q}_{i-1})$ directly so that

$$f(\mathbf{q}_i) - f(\mathbf{q}_{i-1}) - \Delta x \Psi_{i-1/2} = \sum_{p=1}^{n} \beta_{i-1/2}^p r_{i-1}^p \equiv \sum_{p=1}^{n} \mathcal{Z}_{i-1/2}^p,$$

where

$$\beta_{i-1/2} = R_{i-1/2}^{-1} \left(f(\mathbf{q}_i) - f(\mathbf{q}_{i-1}) - \Delta x \Psi_{i-1/2} \right),$$

with

$$\Delta x \Psi_{i-1/2} = \begin{bmatrix} 0 \\ -g\hat{h}\left(b_i - b_{i-1}\right) \\ 0 \end{bmatrix}$$

One ambiguity of the *f-wave* scheme is that several choices are possible for the the approximation of the source terms, in this case $\hat{h}$. George [48] and [49] suggested an alternative choice based on the conservation of energy for smooth solutions

$$-g\hat{h}(b_i - b_{i-1}) = -g\frac{h_i + h_{i-1}}{2}\frac{\widetilde{\lambda_1\lambda_2}}{\overline{\lambda_1\lambda_2}}(b_i - b_{i-1}),$$

where

$$\widetilde{\lambda_1\lambda_2} = g\bar{h} - \bar{u}^2, \qquad \overline{\lambda_1\lambda_2} = g\bar{h} - u_{i-1}u_i.$$

with $\bar{h} = (h_{i-1} + h_i)/2$ and $\bar{u} = (u_{i-1} + u_i)/2$. As the matrix $R_{i-1/2}$ is the matrix of eigenvectors of $\hat{A}_{i-1/2}$, following the notation of [10], the relations are

$$\alpha_{i-1/2} = R_{i-1/2}^{-1} \left(\mathbf{q}_i - \mathbf{q}_{i-1} \right),$$

and

$$\alpha_{i-1/2} s_{i-1/2} = \beta_{i-1/2},$$

lead to the Rankine-Hugoniot condition as follows,

$$s_{i-1/2}\left(\mathbf{q}_i - \mathbf{q}_{i-1}\right) = f(\mathbf{q}_i) - f(\mathbf{q}_{i-1}) - \Delta x \Psi_{i-1/2},$$

where $s_{i-1/2}$ is the shock speed.

$$\begin{aligned} &s\left(h_i - h_{i-1}\right) = (hu)_i - (hu)_{i-1}, \\ &s\left((hu)_i - (hu)_{i-1}\right) = (hu^2 + gh^2/2)_i - (hu^2 + gh^2/2)_{i-1} + g\hat{h}\left(b_i - b_{i-1}\right). \end{aligned} \tag{4.19}$$

If we apply the DLM theory, the shock speeds of the single layer shallow water equations satisfy

$$\begin{aligned} &s\left((h)_i - (h)_{i-1}\right) = (hu)_i - (hu)_{i-1}, \\ &s\left((hu)_i - (hu)_{i-1}\right) = (hu^2 + gh^2/2)_i - (hu^2 + gh^2/2)_{i-1} \\ &\qquad\qquad + g\int_0^1 \Phi_h(t;\mathbf{q}_{i-1},\mathbf{q}_i))\partial_t \Phi_b(t;\mathbf{q}_{i-1},\mathbf{q}_i)dt, \end{aligned} \tag{4.20}$$

where the family of paths $\Phi(t;\mathbf{q}_{i-1},\mathbf{q}_i)$ is

$$\Phi(t;\mathbf{q}_{i-1},\mathbf{q}_i) = \begin{bmatrix} \Phi_h(t) \\ \Phi_q(t) \\ \Phi_b(t) \end{bmatrix}.$$

If we choose the path as follows,

$$\Phi_h = h_{i-1} + t(h_i - h_{i-1}) + 6(t - t^2)\bar{h}\left(\frac{(u_i - u_{i-1})^2}{\bar{u}^2 - g\bar{h}}\right), \quad \Phi_b = b_{i-1} + t(b_i - b_{i-1}),$$

then we recover the same scheme as George [48] suggested.

4.5.3 Multi-layer shallow water equations

Consider two layer shallow water equations with $b(x) \equiv 0$.

$$\mathbf{q}_t + \mathbf{f}(\mathbf{q})_x = \Psi(\mathbf{q}),$$

where

$$\mathbf{q} = \begin{bmatrix} h_1 \\ h_1u_1 \\ h_2 \\ h_2v_2 \end{bmatrix}, \quad \mathbf{f}(\mathbf{q}) = \begin{bmatrix} h_1u_1 \\ h_1u_1^2 + \frac{1}{2}gh_1^2 \\ h_2u_2 \\ h_2u_2^2 + \frac{1}{2}gh_2^2 \end{bmatrix}, \quad \text{and} \quad \Psi(\mathbf{q}) = \begin{bmatrix} 0 \\ -gh_1(h_2)_x \\ 0 \\ -rgh_2(h_1)_x \end{bmatrix}.$$

One simple choice is the arithmatic mean so that

$$\hat{h}_1 = \frac{(h_1)_i + (h_1)_{i-1}}{2}, \qquad \hat{h}_2 = \frac{(h_2)_i + (h_2)_{i-1}}{2}.$$

Similar to the single layer case, the shock speed condition takes the explicit form

$$\begin{aligned}
&s\left((h_1)_i - (h_1)_{i-1}\right) = (h_1u_1)_i - (h_1u_1)_{i-1},\\
&s\left((h_1u_1)_i - (h_1u_1)_{i-1}\right) = (h_1u_1^2 + gh_1^2/2)_i - (h_1u_1^2 + gh_1^2/2)_{i-1}\\
&\qquad\qquad + g\frac{(h_1)_i + (h_1)_{i-1}}{2}\left((h_2)_i - (h_2)_{i-1}\right),\\
&s\left((h_2)_i - (h_2)_{i-1}\right) = (h_2u_2)_i - (h_2u_2)_{i-1},\\
&s\left((h_2u_2)_i - (h_2u_2)_{i-1}\right) = (h_2u_2^2 + gh_2^2/2)_i - (h_2u_2^2 + gh_2^2/2)_{i-1}\\
&\qquad\qquad + rg\frac{(h_2)_i + (h_2)_{i-1}}{2}\left((h_1)_i - (h_1)_{i-1}\right),
\end{aligned} \tag{4.21}$$

when we choose the arithmetic average for $\hat{h}_1$ and $\hat{h}_2$.

When applied to the two layer shallow water system, the equation (4.18) reads

$$\begin{aligned}
&s\left((h_1)_i - (h_1)_{i-1}\right) = (h_1u_1)_i - (h_1u_1)_{i-1},\\
&s\left((h_1u_1)_i - (h_1u_1)_{i-1}\right) = (h_1u_1^2 + gh_1^2/2)_i - (h_1u_1^2 + gh_1^2/2)_{i-1}\\
&\qquad\qquad + g\int_0^1 \Phi_{h_1}(t;\mathbf{q}_{i-1},\mathbf{q}_i))\partial_t\Phi_{h_2}(t;\mathbf{q}_{i-1},\mathbf{q}_i)dt,\\
&s\left((h_2)_i - (h_2)_{i-1}\right) = (h_2u_2)_i - (h_2u_2)_{i-1},\\
&s\left((h_2u_2)_i - (h_2u_2)_{i-1}\right) = (h_2u_2^2 + gh_2^2/2)_i - (h_2u_2^2 + gh_2^2/2)_{i-1}\\
&\qquad\qquad + rg\int_0^1 \Phi_{h_2}(t;\mathbf{q}_{i-1},\mathbf{q}_i))\partial_t\Phi_{h_1}(t;\mathbf{q}_{i-1},\mathbf{q}_i)dt,
\end{aligned} \tag{4.22}$$

where the family of paths $\Phi(t;\mathbf{q}_{i-1},\mathbf{q}_i)$ is

$$\Phi(t;\mathbf{q}_{i-1},\mathbf{q}_i) = \begin{bmatrix} \Phi_{h_1} \\ \Phi_{q_1} \\ \Phi_{h_2} \\ \Phi_{q_2} \end{bmatrix}.$$

One of the choices is linear path,

$$\Phi(t;\mathbf{q}_{i-1},\mathbf{q}_i) = \mathbf{q}_{i-1} + t(\mathbf{q}_i - \mathbf{q}_{i-1}),$$

for $0 \leq t \leq 1$. Thus Φ_{h_1} and Φ_{h_2} are given as

$$\begin{aligned} \Phi_{h_1}(t; \mathbf{q}_{i-1}, \mathbf{q}_i) &= (h_1)_{i-1} + t\left((h_1)_i - (h_1)_{i-1}\right), \\ \Phi_{h_2}(t; \mathbf{q}_{i-1}, \mathbf{q}_i) &= (h_2)_{i-1} + t\left((h_2)_i - (h_2)_{i-1}\right). \end{aligned} \tag{4.23}$$

When these two equations (4.23) are applied to the equations (4.22), the integral of the second equation of (4.22) leads to

$$\begin{aligned} \int_0^1 \Phi_{h_1}(t; \mathbf{q}_{i-1}, \mathbf{q}_i))\partial_t \Phi_{h_2}(t; \mathbf{q}_{i-1}, \mathbf{q}_i) dt &= \int_0^1 (h_1)_{i-1} + t\left((h_1)_i - (h_1)_{i-1}\right)\left((h_2)_i - (h_2)_{i-1}\right) dt \\ &= \left[t(h_1)_{i-1} + t^2/2\left((h_1)_i - (h_1)_{i-1}\right)\left((h_2)_i - (h_2)_{i-1}\right)\right]_0^1 \\ &= \frac{(h_1)_i + (h_1)_{i-1}}{2}\left((h_2)_i - (h_2)_{i-1}\right). \end{aligned}$$

Similar calculation for the integral of the fourth equation of (4.22) reduces to the shock condition (4.21) found by the *f-wave* method.

In the study of non-conservative system, the solution is not uniquely determined, because the jump condition at the discontinuities depends on the choice of the path and we can choose different paths. Dolejsi and Gallouet [35] investigated the non-conservative system which arises from a flow simulation of solid-liquid-gas slurries. They compared the numerical results from different numerical schemes, and showed that different numerical schemes converge to different weak solutions.

4.6 Dry State Riemann Problem

For single layer shallow water system, *dry state Riemann problems* refer to the cases where either h_{i-1} or h_i is zero, or a dry state appears in the Riemann solution for $t > 0$. In forecasting tsunamis, one of our interests is predicting the inundation accurately, and the dry state Riemann problems arise at the shorelines. Depth positivity is one of the properties required for dry state Riemann solvers, and the HLLE scheme is used in this work. For details, see George [48] for example. In multi-layer shallow water system, there are more than one type of dry state Riemann problems. Some previous works include Castro et al. [23] and Mandli [97].

Consider the case depicted in Figure 4.2 where $(h_1)_i = (h_2)_i = 0$. This is dry state

problem for both upper and lower layers. It is required to determine whether lower and/or upper layer will overtop the right bathymetry b_i or not.

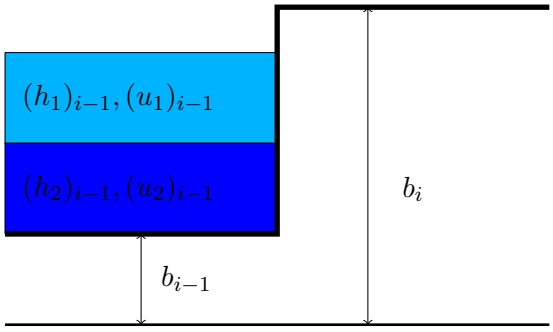

Figure 4.2: Dry state Riemann problem Case 1.

Let us call the *right solid wall for lower layer* if $(h_2)_{i-1} + b_{i-1} < b_i$ and $(h_2)^* + b_{i-1} < b_i$ are satisfied. We call similarly for the upper layer and left solid wall cases. In order to determine the solid wall states, we compare $(h_2)_{i-1} + b_{i-1}$ and b_i. If $(h_2)_{i-1} + b_{i-1}$ is greater than b_i, then we expect the lower layer will overtop b_i, and we solve the Riemann problem without modification. Even if $(h_2)_{i-1} + b_{i-1} < b_i$, we cannot say that lower layer has right solid wall because the lower layer still can overtake b_i depending on the speed of the lower layer $(u_2)_{i-1}$. To determine it, we solve single layer shallow water system with $(h_2)_i = (h_2)_{i-1}$ and $(u_2)_i = (u_2)_{i-1}$. If $h_2^* + b_{i-1} < b_i$ from the resolved solution, then we say solid wall on the right side for the lower layer. Otherwise, there is no right solid wall case. If lower layer has right solid wall, then we proceed to the upper layer to figure out solid wall state in a smiler way.

If we have determined there is a solid wall on the right for both upper and lower layer, we solve the modified Riemann problem such that

$$
\begin{aligned}
&(h_1)_i = (h_1)_{i-1}, \quad (u_1)_i = -(u_1)_{i-1}, \\
&(h_2)_i = (h_2)_{i-1}, \quad (u_2)_i = -(u_2)_{i-1}, \\
&\text{and} \quad b_i = b_{i-1}.
\end{aligned}
$$

If only the lower layer has right solid wall state, more careful modification is required based

on preserving steady states shown in Figure 4.3. We solve the revised Riemann problem as follows,

$$\begin{aligned} &\text{lower layer}: \quad (h_2)'_i = (h_2)_{i-1}, \quad (u_2)'_i = -(u_2)_{i-1}, \quad \text{and} \quad b'_i := b_{i-1}, \\ &\text{upper layer}: \quad b'_{i-1} := b_{i-1} + (h_2)_{i-1}. \end{aligned}$$

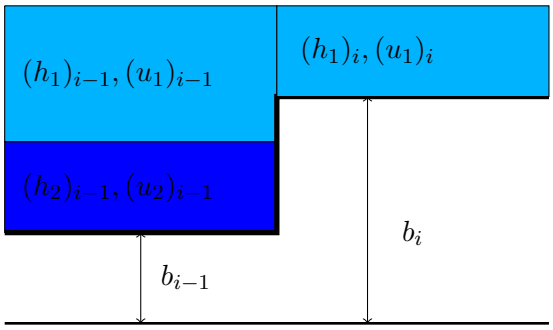

Figure 4.3: Dry state Riemann problem Case 2.

If the *f-wave* method is applied for this case, then the flux difference with source term reduces to

$$\begin{aligned} &f(\mathcal{Q}_i) - f(\mathcal{Q}_{i-1}) - \Delta x \Psi_{i-1/2} \\ &= \begin{bmatrix} [[h_1 u_1]] \\ [[h_1 u_1^2 + g h_1^2/2]] + g\bar{h}_1 \left([[b]] - (h_2)_{i-1} \right) \\ [[h_2 u_2]] \\ [[h_2 u_2^2 + g h_2^2/2]] \end{bmatrix}, \end{aligned}$$

where $[[q]] = q_i - q_{i-1}$. With this modification, we can preserve the steady states.

4.7 Alternative Schemes for the Coupled System

4.7.1 Layer-by-Layer Approaches

Instead of solving the full system, we solve each layer system alternately. We solve the equations for the upper layer,

$$(h_1)_t + (h_1 u_1)_x = 0,$$
$$(h_1 u_1)_t + \left(h_1 u_1^2 + \frac{g}{2} h_1^2\right)_x = g h_1 (h_2 + b)_x.$$

And then the equations for the lower layer,

$$(h_2)_t + (h_2 u_2)_x = 0,$$
$$(h_2 u_2)_t + \left(h_2 u_2^2 + \frac{g}{2} h_2^2\right)_x = g h_2 (r h_1 + b)_x.$$

are solved with same time step size Δt. In one time step, each layer is determined from the information at the start of the computation, and they do not interact directly. For this reason, this scheme is called the *layer-by-layer* approach.

The *layer-by-layer* approach has several advantages over the fully coupled one. Based on the HLLE type method, this scheme can maintain depth positivity. And this system is always hyperbolic since the eigenvalues are given as

$$\lambda_{upper} = u_1 \pm \sqrt{g h_1}, \quad \text{and} \quad \lambda_{lower} = u_2 \pm \sqrt{g h_2},$$

which are always real. Since the eigenstructure is explicit, this scheme is computationally efficient. However, this scheme may not reflect the physical situation correctly if the interaction between two layers is significant. When the difference in the speeds of two layers is large, the eigenvalues are real numbers and we are still able to solve this system.

Castro et al. [25] suggested a numerical test where this *layer-by-layer* approach completely fails. Consider a Riemann problem with the following initial conditions

$$h_1(x,0) = \begin{cases} 0.5, & \text{if } x < 0, \\ 0.55, & \text{if } x > 0, \end{cases} \qquad (hu)_1(x,0) = \begin{cases} 1.25, & \text{if } x < 0, \\ 1.375, & \text{if } x > 0, \end{cases}$$
$$h_2(x,0) = \begin{cases} 0.5, & \text{if } x < 0, \\ 0.45, & \text{if } x > 0, \end{cases} \qquad (hu)_2(x,0) = \begin{cases} 1.25, & \text{if } x < 0, \\ 1.125, & \text{if } x > 0, \end{cases}$$

with $r = 0.98$. The test is an interface-moving problem as $u_1 = u_2 \equiv 2.5$. When the eigenvalues are computed from *layer-by-layer*, we have

$$\lambda_{upper} = 2.5 \pm 2.2694, \quad \lambda_{lower} = 2.5 \pm 2.1586.$$

Thus we have four positive eigenvalues. When they are calculated from the fully coupled system, the eigenvalues are

$$\lambda = -0.6242,\ 2.2782,\ 2.7281 \text{ and } 5.6242.$$

Thus we have three positive eigenvalues and one negative eigenvalue. Therefore the layer-by-layer approach fails since the eigenvalues are completely different.

When we focus on the submarine landslides and tsunamis, Fine et al. [41] showed that the condition, $u_2 < \sqrt{gh_2}$, is satisfied for the submarine flows. Under this regime, numerical results from the *layer-by-layer* approach may not be remarkably different from the fully coupled one. Bouchut and Zeitlin [18] suggested an improved layer-by-layer scheme with flux modification based on the entropy of each layer.

4.7.2 One-way Coupled Model

Another class of numerical scheme is *one-way coupled model*. Assuming that the surface variation is small compared to the total depth,

$$h_1 + h_2 + b \approx constant,$$

we have

$$(h_1)_x = -(h_2 + b)_x \tag{4.24}$$

Replacing (4.24) into the momentum equation of the lower layer, the two layer system can be written as follows,

$$\begin{aligned}
&(h_1)_t + (h_1 u_1)_x = 0,\\
&(h_1 u_1)_t + \left(h_1 u_1^2 + \frac{g}{2} h_1^2\right)_x = -g h_1 (h_2 + b)_x,\\
&(h_2)_t + (h_2 u_2)_x = 0,\\
&(h_2 u_2)_t + \left(h_2 u_2^2 + \frac{g'}{2} h_2^2\right)_x = -g' h_2 b_x,
\end{aligned}$$

where $g' = (1-r)g$ is the reduced gravity. The eigenvalues are easily found as

$$\lambda_{upper} = u_1 \pm \sqrt{gh_1}, \quad \text{and} \quad \lambda_{lower} = u_2 \pm \sqrt{g'h_2}.$$

Therefore, this scheme is hyperbolic and depth positivity preserving.

The *one-way coupled* and the *layer-by-layer* approaches look similar. One of the advantages of *one-way coupled* approach is in the approximations to the exact eigenvalues. For example, consider the case with $h_2 \ll h_1$. Then the equation (4.11) yields $U_m = u_1$ and $U_c = u_2$. From equations (4.9) and (4.10), the eigenvalues of fully coupled system are

$$\lambda^{\pm}_{ext} \approx u_1 \pm \sqrt{gh_1}, \quad \text{and} \quad \lambda^{\pm}_{int} \approx u_2 \pm \sqrt{g'h_2},$$

which are approximation to the eigenvalues of the *one-way coupled* approach.

Another advantage is that we can solve the lower layer system independently from the upper layer, which is not possible in the *layer-by-layer* approach. The motion of the submarine landslides can be solved with reduced gravity g' followed by the usual tsunami models with moving topography.

Several limitation can be noted for this *one-way coupled* model. Sometimes, large waves can be generated by the subaerial landslides plunging into the water. In these cases, the above assumptions are not valid and coupling between two layers needs to be considered carefully. When the friction between two layers are important, the one-way coupled model cannot be used because the friction force is calculated based on the difference of the two layers' speeds.

Subaerial Case

In this section, *subaerial landslides* refer to the cases where the landslides are initiated at subaerial or partially subaerial conditions and plunge into the water. If we apply the *one-way coupled* model for the subaerial landslide cases, some modifications are necessary. Some approaches have been suggested by Fine et al. [41] for example. First we need to determine whether the landslide is subaerial or submarine. If $(h_1)_{i-1} > 0$ and $(h_1)_i > 0$, then we assume that the slide is submarine, and otherwise, we regard that the slide is subaerial. If

the slide is subaerial, we solve the momentum equation for the lower layer given as

$$(h_2u_2)_t + \left(h_2u_2^2 + \frac{g}{2}h_2^2\right)_x = -gh_2b_x,$$

because the equation of the lower layer is independent of the upper layer. If the slide is submarine, we solve the reduced gravity equation which is

$$(h_2u_2)_t + \left(h_2u_2^2 + \frac{g'}{2}h_2^2\right)_x = -g'h_2b_x.$$

In this work, we will not include test problems of the subaerial cases, and leave this as future work.

Chapter 5

NUMERICAL SCHEMES FOR LANDSLIDE MODELING

In this chapter, previous works on subaerial landslide modeling will be briefly reviewed, and possible extensions to submarine landslides will be discussed. Inconsistent terminologies have been used to classify different types of landslides, and the landslide classifications suggested by Varnes [135], Hutchinson [72] and Hungr et al. [70], will be adopted in this work. Slope movements can be categorized into five types which are falls, topples, slides, spreads and flows, and the main interest in this chapter is numerical modeling of landslides of flow type. Also we introduce our numerical models that are applied to numerical simulations.

5.1 Landslide Modeling

One of the widely used numerical schemes in landslide modeling is the *Discrete Element Method* (DEM) that was developed by Cundall [30] for numerical modeling of landslides. DEM treats particles as an assembly of distinct bodies, and applies their constitutive properties, contact laws, displacements and body forces respectively. When large scale problems are solved, DEM requires a large number of variables, and is computationally expensive.

One of the alternatives are depth-averaged models that are based on the continuum fluid mechanics. The Savage-Hutter (SH) model is a depth-averaged model that is derived with bed-normal coordinates and applies Coulomb friction. Later Iverson [75], and Pitman and Le's model [118] extended the SH model to a two-layer approaches. These depth-averaged models assume that the velocity profile of the layer is uniform as shown in the Figure 5.1.

Savage and Hutter [123] derived a depth-averaged fluid model with shallowness assumption of the landslides. Details of the assumptions and limitations can be found at Hutter et

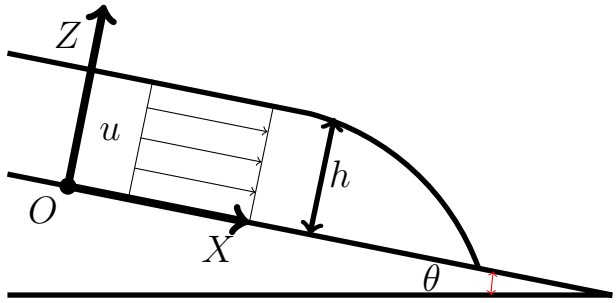

Figure 5.1: Uniform speed profile of the Coulomb fluid

al. [73]. The SH model in 1-dimension is written as

$$\begin{aligned} \frac{\partial h}{\partial t} + \frac{\partial}{\partial x}(hu) &= 0, \\ \frac{\partial}{\partial t}(hu) + \frac{\partial}{\partial x}(hu^2) &= hs_x - \frac{\partial}{\partial x}\left(\frac{\beta_x h^2}{2}\right), \end{aligned}$$

where

$$\begin{aligned} &\beta_x = -g_z K_x, \\ &s_x = g_x - \frac{u}{|u|}\tan\delta\left(-g_z + \lambda\kappa\eta u^2\right) + g_z\frac{\partial b}{\partial x}, \\ &\eta = \cos(\varphi(x) + \varphi_0), \\ &K_x = 2\sec^2\phi\left(1 \mp \left(1 - \cos^2\phi/\cos^2\delta\right)^{1/2}\right), \quad \left(\frac{\partial u}{\partial x} \gtrless 0\right), \end{aligned}$$

with $\mathbf{g} = (g_x, g_z) = (-g\sin\theta, -g\cos\theta)$, and θ is the angle of slope. Moreover $\lambda\kappa$ is the local radius of curvature of the master curve, ϕ and δ are the internal and bed friction angles, and φ is the accumulation of the torsion of the master curve. A single curve, following the landslide topography, is selected as a master curve [119]. The landslide should move along the master curve which must be prescribed.

The SH model has been validated through laboratory experiments. See Koch et al. [80], Gray et al. [54] and Pudasaini and Hutter [119] for examples. However, previous laboratory experiments were performed only with dry granular materials. Since information on the master curve is required, the SH model is appropriate to the confined landslides. For the

open-field flows, the simplified SH model can be used without the torsion and curvature related terms.

For the saturated granular flows, Iverson [75] presented a mixture model with granular material and interstitial fluid. Assuming that the difference of the speed between the granular material and the fluid is small, Iverson derived a reduced model,

$$\begin{aligned}
&\frac{\partial h}{\partial t} + \frac{\partial}{\partial x}(hu) = 0,\\
&\frac{\partial u}{\partial t} + u\frac{\partial u}{\partial x} + \frac{\partial}{\partial x}(\cos(\theta)k_{ap}(h-P)+P)\\
&= -sgn(u)\left(1-\frac{P}{h}\right)\tan\phi\cos\theta - \varphi\mu\eta\frac{u}{h^2} + \sin\theta,
\end{aligned}$$

where P is the pore pressure, μ is the viscosity coefficient and η is a parameter of flow profile.

Pitman and Le [118] extended Iverson's work and derived a two fluid model for the saturated flow. Using the same notation as Pitman and Le [118], their model reads as follows,

$$\begin{aligned}
&\frac{\partial h}{\partial t} + \frac{\partial}{\partial x}\left(h\left(\varphi v + (1-\varphi)u\right)\right) = 0,\\
&\frac{\partial}{\partial t}(h\varphi) + \frac{\partial}{\partial x}(h\varphi v) = 0,\\
&\frac{\partial}{\partial t}(h\varphi v) + \frac{\partial}{\partial x}\left(h\varphi v^2\right) =\\
&-\frac{1}{2}\left(1-\frac{\rho^f}{\rho^s}\right)\frac{\partial}{\partial x}\left(\alpha_{xx}h^2\varphi(-g^z)\right) - \frac{1}{2}\frac{\rho^f}{\rho^s}\varphi\frac{\partial}{\partial x}(h^2(-g^z))\\
&+\left(1-\frac{\rho^f}{\rho^s}\right)(-\alpha_{xx}b_x - \alpha_{xz})h\varphi(-g^z)\frac{\rho^f}{\rho^s}h\varphi(-g^z)b_x\\
&+\left(1-\frac{\rho^f}{\rho^s}\right)\frac{h(1-\varphi)\varphi}{v_T(1-\varphi)^m}(u-v) + h\varphi g^x,\\
&\frac{\partial}{\partial t}(hu) + \frac{\partial}{\partial x}(hu^2) = \frac{1}{2}\frac{\partial}{\partial x}h^2(g^z) - \frac{\rho^s-\rho^f}{\rho^f}\frac{h\varphi}{v_T(1-\varphi)^m}(u-v) + hg^x.
\end{aligned}$$

In this expression, v and u are the velocities of solid and fluid with density ρ^s and ρ^f respectively. The solid volume fraction of the fluid is φ, and v_T is the terminal speed of a typical particle falling vertically in the fluid. Parameter m is related to the Reynold number of the flow.

Since these models are derived in a bed-normal coordinate system, the exact knowledge of the path of the slide motion is desirable. Because the previous models become simple ones without the information on the master curve. Also note that the bed-normal coordinate system can be uniquely determined only when the landslide is shallow and the bathymetry is smooth.

5.2 Submarine Landslide Modeling

5.2.1 Savage-Hutter Type Model

Understanding the deformation of underwater slides is still scarce, and numerical models are not established as well as for subaerial landslides. There are several previous works which adopted simpler forms of the SH model. For example, Heinrich et al. [67] used the SH model for landslides as follows,

$$\begin{aligned} \frac{\partial h}{\partial t} + \frac{\partial}{\partial x}(hu) &= 0, \\ \frac{\partial}{\partial t}(hu) + \frac{\partial}{\partial x}\left(hu^2 + \frac{g'}{2}h^2\right) &= -g'hb_x - \tau, \end{aligned} \tag{5.1}$$

where τ is a friction force, g' is the reduced gravity, and θ and φ are the slope angle and the internal friction angle respectively. The motion of the landslides is computed with equations (5.1), and the results are transformed from bed-normal coordinates to earth-centered coordinates. Then the shallow water equations are used for the water layer where the change of bathymetry is computed with the SH model. The water layer is affected by the submarine landslides, but the slide layer is not influenced by the water.

Fernández-Nieto et al. [40] suggested a two-layer coupled SH type model for submarine landslides and generated waves. This model is fully coupled between the water and slide layer in bed-normal coordinates, and it is applicable only to 1-dimension with mild change in bathymetry.

5.2.2 Choice of the Coordinate System

Landslides should be thin and the bathymetry needs to be smooth in order to use the SH model with the bed-normal coordinates. In Figure 5.2, one possible case is shown where the bed-normal coordinate system does not represent the physical situation correctly. The

depth of the layer at $x = X_1$ and $x = X_2$ are h_1 and h_2 respectively, but there are some areas where the depth of the layer is counted repeatedly. Therefore, the bed-normal coordinate system cannot be used for general cases. For this reason, the earth-centered coordinates are used instead of the bed-normal coordinates.

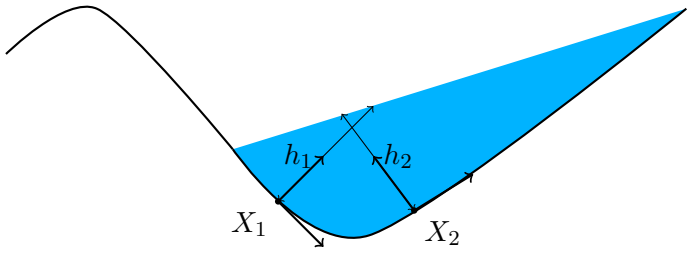

Figure 5.2: Non-physical case with bed-normal coordinates. The depth of the layer at $x = X_1$ and $x = X_2$ are h_1 and h_2 respectively, but they do not represent the correct physical situation.

5.2.3 Friction Models

Coulomb friction model

The Coulomb friction model depends on the basal friction angle that needs to be prescribed according to the properties of materials. The internal friction angle for rock is between 30° and 45°, but this value is often too large to explain the motion of saturated landslides. Submarine landslide movement on a very mild slope ($< 5°$) is often observed, but numerical simulations with the friction angle in this range fail to capture this type of deformation. Even though it is still unclear, one of the possible explanations for the movement of submarine landslide on a mild slope, is that excessive high pore pressure and liquefaction may reduce the friction angle and increase the mobility of landslides. For instance, Heinrich et al. [67] have chosen the value of the basal friction angle between 7° and 17°. In this work, the

following Coulomb friction model will be used,

$$\begin{aligned}
&(h_1)_t + (h_1 u_1)_x = 0, \\
&(h_1 u_1)_t + \left(h_1 u_1^2 + \frac{1}{2} g h_1^2 \right)_x = -g h_1 (h_2 + b)_x, \\
&(h_2)_t + (h_2 u_2)_x = 0, \\
&(h_2 u_2)_t + \left(h_2 u_2^2 + \frac{1}{2} g h_2^2 \right)_x = -g h_2 \left(r h_1 + b \right)_x - r g h_2 \tan(\phi) \cos(\theta) \frac{u_2}{|u_2|},
\end{aligned} \tag{5.2}$$

where ϕ is the basal friction angle, and θ is the angle of the slope.

Viscous fluid model

Jiang and LeBlond [78] explored viscous fluid models for submarine landslides, and Fine et al. [41] applied this approach to large scale problems. Jiang and LeBlond assumed that the velocity profile of the landslide is parabolic as in Figure 5.3 and derived the following equations

$$\begin{aligned}
&(h_1)_t + (h_1 u_1)_x = 0, \\
&(h_1 u_1)_t + \left(h_1 u_1^2 + \frac{1}{2} g h_1^2 \right)_x = -g h_1 (h_2 + b)_x, \\
&(h_2)_t + \frac{2}{3} (h_2 u_2)_x = 0, \\
&\frac{2}{3} (h_2 u_2)_t + \left(\frac{8}{15} h_2 u_2^2 + \frac{1}{2} g h_2^2 \right)_x = -g h_2 \left(r h_1 + b \right)_x - \frac{2 \mu u_2}{\rho_2 h_2},
\end{aligned} \tag{5.3}$$

where μ is the viscosity coefficient for the landslide.

One extended viscous type model is the Herschel-Bulkley model. Details of this model can be found at Huang and Garcia [69] and Chen et al. [27]. The velocity profile of the landslide is shown in Figure 5.4 so that the plug zone has the uniform velocity. Then the basal friction is given as

$$\tau_0 = \tau_y + K \left(\frac{1 + (1/n)}{1 - nH/(2n+1)h_2} \right)^n \left(\frac{|u_2|}{H} \right)^n,$$

where τ_y is the yield stress, K is a dynamic viscosity, n is the flow index between 0 and 1, and $H = h_2 - \tau_y / (\rho_2 g \sin\theta)$ is the depth of the shear zone. If $n = 1$, then this model is the same as the previous Jiang and LeBlond's model. In this work, the viscous fluid model (5.3) will be used.

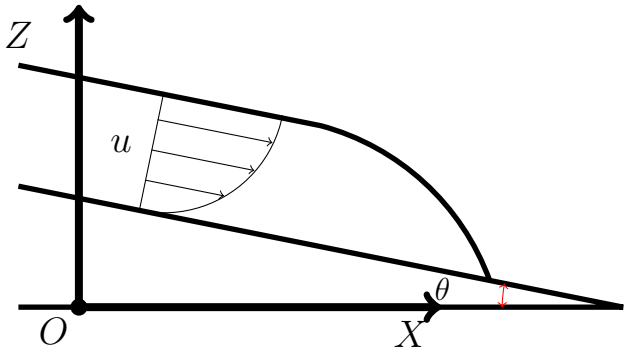

Figure 5.3: Parabolic velocity profile of landslide layer.

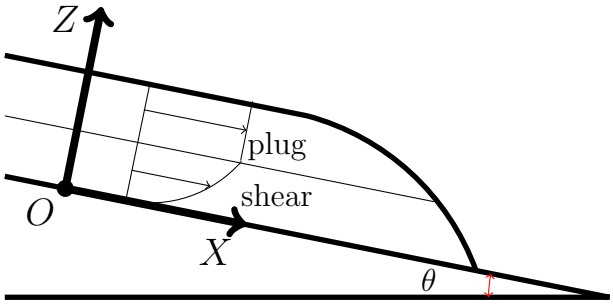

Figure 5.4: Velocity profile of landslide layer with shear and plug zone.

Comparison of friction models

Both the Coulomb friction model (5.2) and the viscous fluid model (5.3) are used to compare the motion of landslides. In these tests, the water layer is ignored and the initial shape of landslide is Gaussian on the uniform slope. Figure 5.5 depicted the initial shape of landslide on a slope of 15°. Three cases of slope will be compared with the slope of angle equal to 5°, 15° and 30°.

Figures 5.6, 5.7 and 5.8 show the height of the landslide at $t = 30$ s on three different slopes of 5°, 15° and 30° respectively. On each figure, the viscous coefficient varies from $\mu = 25$ to 500 m^2/s for the viscous fluid model, and the basal friction angle varies from $\phi = 7°$ to 25° for the Coulomb friction model following Heinrich et al. [67]'s work.

It is observed that the Coulomb friction model depends heavily on the choice of the

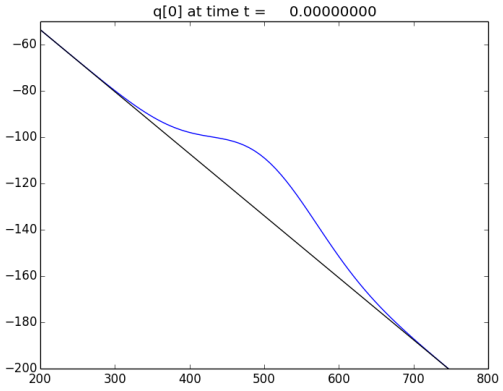

Figure 5.5: Gaussian shape of a landslide on a slope of 15° at $t = 0$ s.

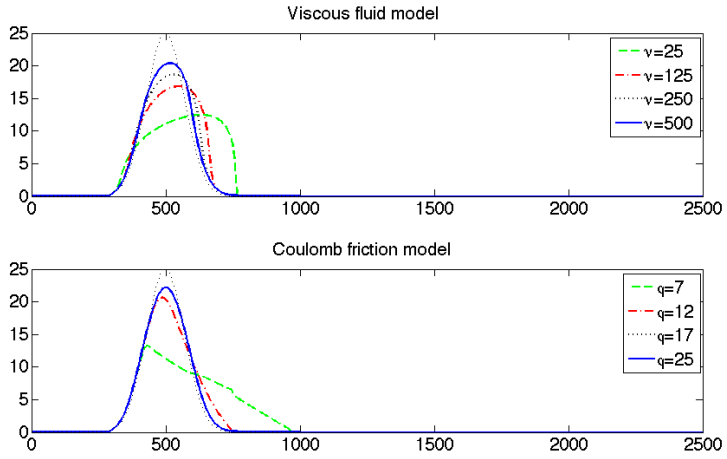

Figure 5.6: Numerical results for the viscous fluid model and the Coulomb friction model on a uniform slope of 5° at $t = 24$ s. The kinematic viscosity is chosen between 25 and 500 m^2/s, and the Coulomb friction angle is selected between 7° and 25°.

basal friction angle. If the basal friction angle is smaller than the angle of the slope, then only small deformation of landslide is observed. As a small difference of the friction angle can result in a large variation, the basal friction angle should be carefully chosen.

On the contrary, the viscous fluid model produces similar patterns for different viscous

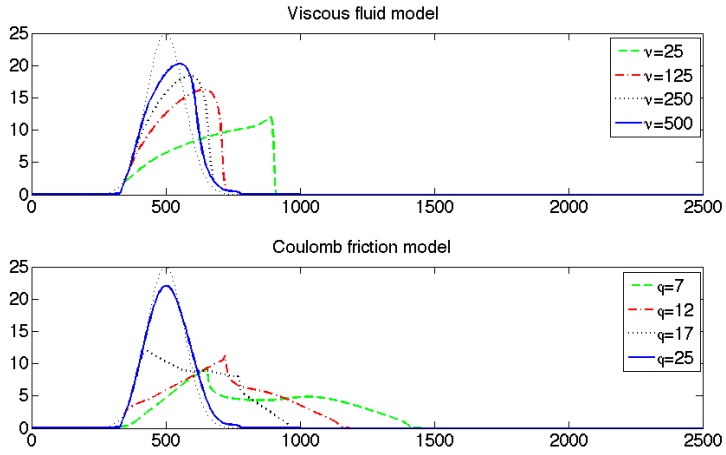

Figure 5.7: Numerical results for the viscous fluid model and the Coulomb friction model on a uniform slope of 15° at t=24 s.

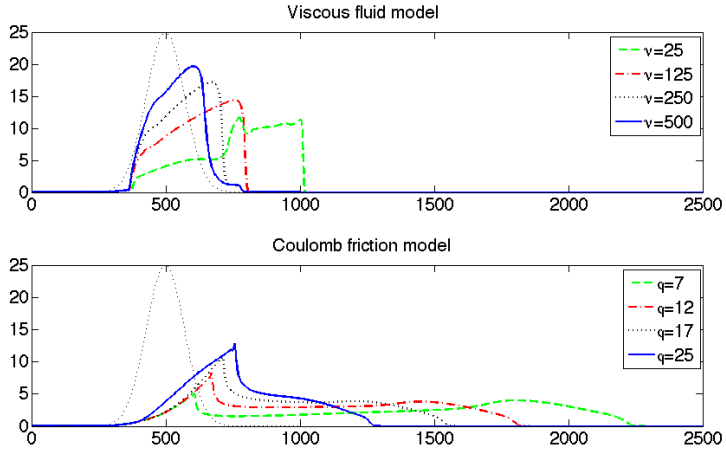

Figure 5.8: Numerical results for the viscous fluid model and the Coulomb friction model on a uniform slope of 30° at t=24 s.

coefficients. A shock front is visible which is observed by Iverson et al. [76] experiments. Though the landslide with smaller viscous coefficient moves further, the difference is not as large as the case of the Coulomb friction model.

5.2.4 Hydroplaning

At a critical speed, the intrusion of a thin water layer underneath the landslide produces *hydroplaning* which is a lubricant effect. Mohrig et al. [104] reported laboratory experiments which demonstrate that the fronts of submarine debris flows can *hydroplane* on thin layers of water. The *hydroplaning* dramatically reduces the bed friction, thus increasing head velocity although their experiments are small scale. Their laboratory experiments showed that the minimum value for the *hydroplaning* is $Fr_d = 0.35$ where

$$Fr_d = \frac{u_2}{\sqrt{\left(\frac{1}{r} - 1\right) g h_2 \cos\theta}}.$$

The *hydroplaning* of the submarine landslide is still poorly understood and the laboratory experiments are not sufficient to validate results of large scale landslides.

De Blasio et al. [32] validated their model by comparing the numerical simulation with the field data of the Storegga slides. The viscosity is time dependent which changes from the initial to residual viscosity constant that is referred to as *remoulding*. De Blasio et al. suggested a yield stress model combining *remoulding* and *hydroplaning*, but the coefficients were adjusted to match the field data.

Taylor et al. [132] suggested a friction model for a semi-elliptic rigid body on a mild slope based on Grilli and Watts [59]. They assumed that for large enough speeds, *hydroplaning* occurs over a specific percentage of slide length. They have chosen 6 m/s as the critical speed for the *hydroplaning* so that the basal friction is given as

$$\tau = \begin{cases} \tau_0, & \text{if } u_2 \leq 6 \text{ m/s}, \\ \tau_0(1 - h_y), & \text{if } u_2 > 6 \text{ m/s}, \end{cases}$$

where τ_0 is the basal friction without hydroplaning and h_y is the fraction of the slide length susceptible to hydroplaning in $[0, 1]$. They have chosen the values for h_y as 0.25, 0.5, 0.75 and 1, and showed that the effect of the basal resistance increases as slope angles decrease.

The previous *hydroplaning* models are derived for the solid body motion, and applying the same model to the fluid model is not straight forward. Determining the front location and speed is a crucial part, and extending it to the 2-dimensional case is another issue.

5.2.5 Pore Water Pressure and Liquefaction

Pore water pressure refers to the pressure exerted on its surroundings by water held in pore spaces in rock or soil. The pressure is positive when a soil is fully saturated, and is then proportional to the height of the water measured in an open tube above the point of interest. The pressure is zero when the soil voids are filled with air, and is negative when the voids are partly filled with water. As discussed in previous section, the pore water pressure has been included in landslide modeling by Iverson [75] and Pitman and Le [118].

Liquefaction is a phenomenon in which the strength and stiffness of a soil is reduced by earthquake shaking or other rapid loading. This occurs in saturated soils where water fills the space between soil particles. Generally, the liquefaction of submarine landslides accounts for the movement on a mild slope. For example, see Seed [125], Grilli and Watts [58] and Finn [42]. Seed [125] show the friction coefficients drop by factors between 2 and 10 by liquefaction.

Chapter 6

BOUSSINESQ EQUATIONS AND NUMERICAL SCHEMES

In tsunami modeling, the shallow water equations are widely used for their accuracy, efficiency and robustness. The wavelength of the earthquake generated tsunami is often several hundred kilometers and the amplitude is several meters so that dispersion of waves is weak and can be ignored. Therefore these waves are under the regime of shallow water equations.

Meanwhile, tsunamis triggered by submarine landslides have different characteristics. As noted by Matsuyama et al. [100], the wavelength of the tsunami is a few kilometers, and waves are generated over a time period of several minutes. Thus dispersion of waves is necessary to include, and other physical models, such as Boussinesq type equations, are often preferable.

The derivations of the several Boussinesq type equations are based on the assumptions that two parameters, the ratio of the wave amplitude to the water depth (ϵ) and the ratio of the water depth to the wavelength (μ), are small and $O(\epsilon) = O(\mu^2)$. In this chapter, we review several Boussinesq type models and develop numerical schemes.

6.1 Airy Wave Theory

Before we discuss the Boussinesq type equations, we briefly review Airy wave theory or Stokes' first order wave theory and derive the linear dispersion relation. See Kundu et al. [81] for example. For simplicity, we consider the two dimensional case, one horizontal direction plus depth, so that depth-averaging gives 1-dimensional equations. If the fluid is incompressible and irrotational, then there exists a velocity potential $\Phi(x, z, t)$ satisfying $\frac{\partial \Phi}{\partial x} = u$ and $\frac{\partial \Phi}{\partial z} = w$. Then the continuity equation can be written in terms of Φ as

$$\frac{\partial^2 \Phi}{\partial x^2} + \frac{\partial^2 \Phi}{\partial z^2} = 0. \tag{6.1}$$

We impose impermeable boundary condition at bottom,

$$\frac{\partial \Phi}{\partial z} = 0, \quad \text{at} \quad z = -b(x), \tag{6.2}$$

and the kinematic free surface boundary condition,

$$\frac{\partial \eta}{\partial t} = \frac{\partial \Phi}{\partial z}, \quad \text{at} \quad z = 0, \tag{6.3}$$

where $b(x)$ is the bathymetry and $\eta(x,t)$ is water surface elevation with respect to the sea-level. The dynamic boundary condition gives

$$\frac{\partial \Phi}{\partial t} + g\eta = 0, \quad \text{at} \quad z = 0. \tag{6.4}$$

We have a set of equations (6.1), (6.2), (6.3) and (6.4). Since we are looking for the plane wave solution, we set

$$\Phi = A(z)\sin(\omega t - kx), \tag{6.5}$$

where k and ω are wave number and frequency of wave respectively. If we plug (6.5) into (6.1), then we have

$$\big(-k^2 A(z) + A''(z)\big)\sin(\omega t - kx) = 0. \tag{6.6}$$

General solutions to the second order ODE $-k^2 A(z) + A''(z) = 0$ is

$$A(z) = C_1 \cosh(kz + C_2),$$

with constants C_1 and C_2. The boundary condition (6.2) reads

$$C_1 \sinh(kz + C_2)\sin(\omega t - kx) = 0, \quad \text{at} \quad z = -b(x).$$

If we assume $b(x) \equiv H$, then the equation (6.1) leads to $C_2 = kH$. From the equation (6.4), we have,

$$\eta = -\frac{1}{g}\omega C_1 \cosh(kH)\cos(\omega t - kx),$$

which should satisfy (6.3). Therefore we have

$$\frac{1}{g}\omega^2 C_1 \cosh(kH)\sin(\omega t - kx) = C_1 k \sinh(kH)\sin(\omega t - kx).$$

This leads to the dispersion relation

$$\omega^2 = gk \tanh(kH). \tag{6.7}$$

Moreover, if we set $\eta_0 = \frac{\omega}{g} C_1 \cosh(kH)$, then we have

$$\eta = \eta_0 \sin(\omega t - kx).$$

Thus the phase speed c_p is

$$c_p = \frac{\omega}{k} = \sqrt{\frac{g \tanh(kH)}{k}}.$$

If the depth of water H is much smaller than the wavelength λ, then those waves are often referred to as *shallow water waves*. We have $\omega^2 \approx k^2 gH$, and the phase speed and group speed can be approximated as

$$c_p \approx \sqrt{gH}, \quad \text{and} \quad c_g \approx \sqrt{gH}.$$

For *deep water waves* with $H > \lambda/4$, we have $\omega^2 \approx gk$, and $\lambda_0 = \frac{2\pi}{k} = \frac{2\pi g}{\omega^2}$ is often called the *deep water wavelength*.

In the following section, we will review Boussinesq type equations which were developed to match the dispersion relation (6.7) of the given waves. Matching the dispersion relation will be optimized for different range of kH.

6.2 Boussinesq Type Equations

In this section, we review previous work on Boussinesq type equations for slowly varying topography, that is $||\nabla b|| \ll 1$. Depth averaged equations have been developed to match dispersion relation over some range of kH. Figure 6.1 shows the basic formulation for set-up. In the case of submarine landslides, we let $b(x)$ be the bathymetry after deformation has finished, and $\bar{b}(x,t)$ be the displacement of seabed which is small relative to the depth of water. Then the depth of water $h(x,t)$ is given as $h(x,t) = -b(x) - \bar{b}(x,t) + \eta(x,t)$. We use $H(x)$ to denote $H(x) = -b(x)$.

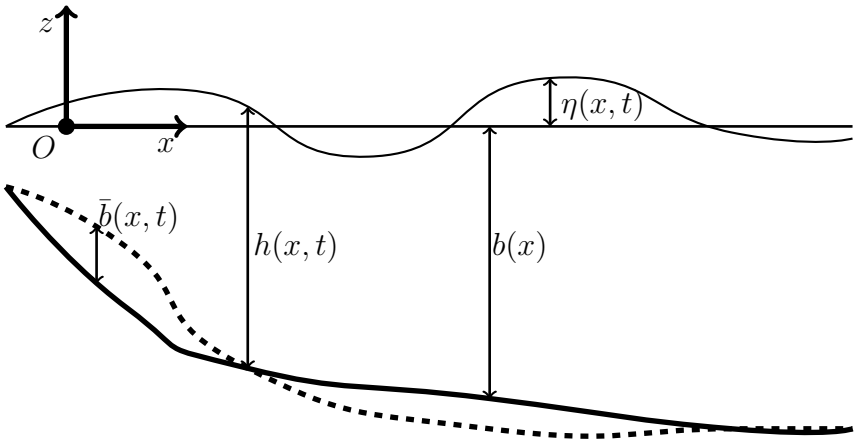

Figure 6.1: Basic set-up for the Boussinesq type equations with moving bathymetry.

6.2.1 Peregrine (1967)

Peregrine [115] derived the following Boussinesq equations

$$\eta_t + \nabla \cdot ((H+\eta)\mathbf{u}) = 0, \tag{6.8}$$

$$\mathbf{u}_t + (\mathbf{u}\cdot\nabla)\,\mathbf{u} + g\nabla\eta + \left[\frac{1}{6}H^2\frac{\partial}{\partial t}\nabla(\nabla\cdot\mathbf{u}) - \frac{1}{2}H\frac{\partial}{\partial t}\nabla(\nabla\cdot(H\mathbf{u})\right] = 0, \tag{6.9}$$

where $\mathbf{u}(\mathbf{x},t)$ is the depth-averaged velocity. This set of equations is derived from the inviscid Euler equation. Two parameters ϵ and μ are defined as the ratio of amplitude to depth and the ratio of depth to wavelength which are relatively small. We assume $\epsilon \approx \mu^2$ in the derivations. Then we use Taylor expansion with these parameters, and retain $O(\epsilon)$ terms. Details of the derivation can be found in Peregrine [115].

6.2.2 Nwogu (1993)

Nwogu [107] improved Peregrine's work by using a quadratic polynomial for the water velocity profile. The set of equations is derived from Euler's equations with a reference velocity at a specific depth, which is

$$\mathbf{u}(x,z) = \mathbf{u}_\alpha + \mu^2\left(\frac{z_\alpha^2}{2} - \frac{z^2}{2}\right)\nabla(\nabla\cdot\mathbf{u}_\alpha) + \mu^2(z_\alpha - z)\nabla(\nabla\cdot(H\mathbf{u}_\alpha)),$$

where $\mathbf{u}_\alpha$ is the velocity at $z = z_\alpha$. Nwogu's Boussinesq equations are written as

$$\eta_t + \nabla \cdot ((H + \epsilon\eta)\mathbf{u}_\alpha) + \mu^2 \nabla \left[\left(\frac{z_\alpha^2}{2} - \frac{H^2}{6} \right) \nabla(\nabla \cdot \mathbf{u}_\alpha) + \left(z_\alpha + \frac{H}{2} \right) H \nabla(\nabla \cdot (H\mathbf{u}_\alpha)) \right] = 0, \tag{6.10}$$

$$\mathbf{u}_{\alpha t} + \epsilon \left(\mathbf{u}_\alpha \cdot \nabla \right) \mathbf{u}_\alpha + g\nabla\eta + \mu^2 \left[\frac{z_\alpha^2}{2} \nabla(\nabla \cdot \mathbf{u}_{\alpha t}) + z_\alpha \nabla(\nabla \cdot (h\mathbf{u}_{\alpha t})) \right] = 0. \tag{6.11}$$

Nwogu defined a value α as

$$\alpha = (z_\alpha/H)^2/2 + (z_\alpha/H), \tag{6.12}$$

and showed that the optimal value for α is equal to -0.390 in the range $0 < H/\lambda_0 < 0.5$, where λ_0 is the deep water wavelength. The value z_α is determined by solving the equation (6.12). If α is zero, then $z_\alpha = 0$, and Peregrine's form is recovered.

6.2.3 Schäffer and Madsen (1995)

Another set of Boussinesq type equations is derived by Schäffer and Madsen [124], that is a modification of Madsen and Sørenson [96]. To derive it, we modify Peregine's model (6.8) and (6.9) in conservative form as follows,

$$h_t + \nabla \cdot (h\mathbf{u}) = 0, \tag{6.13}$$

$$(h\mathbf{u})_t + \left((h\mathbf{u}) \cdot \nabla \right) \mathbf{u} + \mathbf{u} \left(\nabla \cdot (h\mathbf{u}) \right) + gh\nabla\eta + \left[\frac{1}{6} H^3 \frac{\partial}{\partial t} \nabla(\nabla \cdot \mathbf{u}) - \frac{1}{2} H^2 \frac{\partial}{\partial t} \nabla(\nabla \cdot (H\mathbf{u}) \right] = 0. \tag{6.14}$$

By applying the operator $BH^3\nabla(\nabla\cdot)$ to the momentum equation of the linearized shallow water equations, $u_t + g\nabla\eta = 0$, we have

$$-BH^3 \left(\nabla \left(\nabla \left(u_t \right) \right) + \nabla \left(\nabla \cdot g\nabla\eta \right) \right) = 0, \tag{6.15}$$

where B is a parameter to be determined. Adding (6.14) and (6.15) yields the Schäffer and Madsen [124] model. In the two dimensional case, the equations have the following form,

$$h_t + P_x + Q_y = 0, \tag{6.16}$$

$$P_t + \left(\frac{P^2}{h} + \frac{g}{2} h^2 \right)_x + \left(\frac{PQ}{h} \right)_y + ghb_x + \psi_1 = 0, \tag{6.17}$$

$$Q_t + \left(\frac{Q^2}{h} + \frac{g}{2} h^2 \right)_y + \left(\frac{PQ}{h} \right)_x + ghb_y + \psi_2 = 0, \tag{6.18}$$

with

$$\begin{aligned}\psi_1 =&\frac{1}{6}H^3\left(\left(\frac{P}{H}\right)_{xxt}+\left(\frac{Q}{H}\right)_{xyt}\right)-\left(B+\frac{1}{2}\right)H^2\left(P_{xxt}+Q_{xyt}\right)\\&-BgH^2\left(\left(H\eta_x\right)_{xx}+\left(H\eta_y\right)_{xy}\right),\\\psi_2 =&\frac{1}{6}H^3\left(\left(\frac{Q}{H}\right)_{yyt}+\left(\frac{P}{H}\right)_{xyt}\right)-\left(B+\frac{1}{2}\right)H^2\left(Q_{yyt}+P_{xyt}\right)\\&-BgH^2\left(\left(H\eta_y\right)_{yy}+\left(H\eta_x\right)_{xy}\right),\end{aligned}$$

where $P = hu$ and $Q = hv$ are x and y momentum respectively. Madsen and Sørenson [96] deduced that the optimal value of the parameter B is $1/15$ through Padé expansion of the dispersion relation.

6.2.4 Serre's equation

Another form of Boussinesq equations is the Serre or Green-Naghdi equations. Bonneton et al. [17] derived the following equations,

$$\begin{aligned}&h_t+\nabla\cdot(h\mathbf{u})=0,\\&(h\mathbf{u})_t+\frac{\gamma-1}{\gamma}gh\nabla\eta+\nabla\cdot(h\mathbf{u}\otimes\mathbf{u})+\left(I+\gamma h\mathcal{T}\frac{1}{h}\right)^{-1}\left[\frac{1}{\gamma}gh\nabla\eta+h\mathcal{Q}_1(\mathbf{u})\right]=0,\end{aligned}$$

where γ is a parameter. The operator $\mathcal{T}$ and $\mathcal{Q}_\infty$ are defined as

$$\begin{aligned}\mathcal{T}[h,b]W&=\mathcal{R}_1[h,b](\nabla\cdot W)+\mathcal{R}_2[h,b](\nabla b\cdot W),\\\mathcal{Q}_1[h,b](V)&=-2\mathcal{R}_1(\partial_1V\cdot\partial_2V^\perp+(\nabla\cdot V)^2)+\mathcal{R}_2(V\cdot(V\cdot\nabla)\nabla b),\end{aligned}$$

where

$$\begin{aligned}\mathcal{R}_1[h,b]w&=-\frac{1}{3h}\nabla(h^3w)-\frac{h}{2}w\nabla b,\\\mathcal{R}_2[h,b]w&=\frac{1}{2h}\nabla(h^2w)+w\nabla b,\end{aligned}$$

with $V^\perp = (-V_2, V_1)^T$. The parameter γ is determined to approximate the dispersion relation (6.7) and Bonneton et al. showed that the optimal value is $\gamma = 1.159$, which was found for $kH \in [0, 4]$. When the parameter $\gamma = 1$, we recover the original Green-Naghdi equations [55]. One of the advantages of using Serre's equations is the existence of

analytical solutions when the bathymetry is flat, and thus we can use this set of equations for the convergence tests, for instance.

6.2.5 Other approximations

Other forms of Boussinesq type equations have been investigated by various researchers such as Wei et al. [141], Gobbi and Kirby [51] and Lynett and Liu [90]. Higher order approximation can be obtained by retaining up to $O(\epsilon^2)$ and $O(\mu^4)$ terms since $\epsilon = O(\mu^2)$. See Fuhrman and Madsen [94], and Zhou and Teng [144], for example.

6.3 Waves Generated by Submarine Landslides

In this section, we briefly review Boussiesq type equations which incorporate the moving bathymetry. We introduce a new variable $\bar{h}(x, y, t)$ where $b(x, y, t) = H(x, y) + \bar{h}(x, y, t)$, and assume that $|\bar{h}(x, y, t)|$ is small. The displacement $\bar{h}$ is pre-determined and is not affected by the change of water wave.

6.3.1 Lynett and Liu (2002)

Lynett and Liu [90] derived the following equations for submarine landslides,

$$\begin{aligned}
&\eta_t + \nabla \cdot (H\mathbf{u}_\alpha) + \bar{h}_t \\
&+ \nabla \cdot \left[\left(\frac{z_\alpha^2}{2} - \frac{H^2}{6} \right) H \nabla(\nabla \cdot \mathbf{u}_\alpha) + \left(z_\alpha + \frac{H}{2} \right) H \nabla(\nabla \cdot (H\mathbf{u}_\alpha + \bar{h}_t)) \right] = 0, \\
&\mathbf{u}_{\alpha t} + (\mathbf{u}_\alpha \cdot \nabla)\, \mathbf{u}_\alpha + g\nabla\eta + \left[\frac{z_\alpha^2}{2} \nabla(\nabla \cdot \mathbf{u}_{\alpha t}) + z_\alpha \nabla(\nabla \cdot (h\mathbf{u}_{\alpha t} + \bar{h}_t)) \right]_t = 0.
\end{aligned}$$

We notice this set of equations is same as Nwogu's model except the $\bar{h}$ terms. A depth averaged model can be derived to yield

$$\eta_t + \nabla \cdot (H\mathbf{u}) + \bar{h}_t = 0, \tag{6.19}$$

$$\mathbf{u}_t + (\mathbf{u} \cdot \nabla)\, \mathbf{u} + g\nabla\eta + \left[\frac{1}{6} H^2 \nabla(\nabla \cdot \mathbf{u}_t) - \frac{1}{2} H \nabla(\nabla \cdot (H\mathbf{u}_t) + \bar{h}_t) \right]_t = 0. \tag{6.20}$$

This set of equations is Peregrine's equations plus time dependent bathymetry.

6.3.2 Modified Schäffer and Madsen

Following Lynett and Liu's derivation, we modify Schäffer and Madsen's model for submarine landslide case. The set of equations are (6.16), (6.17) and (6.18) with

$$\begin{aligned}\psi_1 =& \frac{1}{6}H^3\left(\left(\frac{P}{H}\right)_{xxt}+\left(\frac{Q}{H}\right)_{xyt}\right)-\left(B+\frac{1}{2}\right)H^2\left(P_{xxt}+Q_{xyt}\right)\\ &-BgH^2\left(\left(H\eta_x\right)_{xx}+\left(H\eta_y\right)_{xy}\right)-\frac{1}{2}H^2\bar{h}_{xtt}, \qquad (6.21)\\ \psi_2 =& \frac{1}{6}H^3\left(\left(\frac{Q}{H}\right)_{yyt}+\left(\frac{P}{H}\right)_{xyt}\right)-\left(B+\frac{1}{2}\right)H^2\left(Q_{yyt}+P_{xyt}\right)\\ &-BgH^2\left(\left(H\eta_y\right)_{yy}+\left(H\eta_x\right)_{xy}\right)-\frac{1}{2}H^2\bar{h}_{ytt}. \qquad (6.22)\end{aligned}$$

6.3.3 Choice of physical model

In this work, we adopt modified the Schäffer and Madsen's model which are (6.16), (6.17), (6.18), (6.21) and (6.22). Note that H will go to zero near the coastline. For H sufficiently small, we switch to the shallow water equations and do not include any dispersive terms. In section 6.6, more details will be discussed.

One of the reasons for choosing this model is that it is a relatively simple depth-averaged model with conservative form. And we can easily distinguish the shallow water part and dispersive part. Another reason for this choice is in the construction of a numerical scheme, and in section 6.5 details will be included.

6.4 Dispersion Relation

In this section, we derive the dispersion relation corresponding to various forms of the Boussinesq equations. We set the local wave number, the angular wave frequency, and phase speed as k, ω, and c respectively.

6.4.1 Dispersion Relation of Schäffer and Madsen's Model

In this section, dispersion relation for Schäffer and Madsen's model will be derived. Consider the 1-dimensional model with flat bottom ($\frac{\partial b}{\partial x} \equiv 0$ and $H =$ constant),

$$h_t + (hu)_x = 0, \tag{6.23}$$

$$(hu)_t + \left(hu^2 + \frac{g}{2}h^2\right)_x + \psi_1 = 0, \tag{6.24}$$

with

$$\psi_1 = \frac{1}{6}H^2 (hu)_{xxt} - \left(B + \frac{1}{2}\right) H^2 (hu)_{xxt} - BgH^3\eta_{xxx}.$$

Assuming a Fourier mode, we let $h = H + h_0 e^{ikx-\omega t}$, $\eta = h_0 e^{i(kx-\omega t)}$ and $hu = P_0 e^{i(kx-\omega t)}$ and plug them into (6.23) and (6.24). If we keep linear terms only, we have

$$\begin{cases} h_0(-i\omega)e^{i(kx-\omega t)} + P_0(ik)e^{i(kx-\omega t)} = 0, \\ P_0(-i\omega)e^{i(kx-\omega t)} + gH(ik)h_0 e^{i(kx-\omega t)} \\ +\frac{1}{6}H^2 P_0(ik^2\omega)e^{i(kx-\omega t)} - \left(B + \frac{1}{2}\right) H^2 P_0(ik^2\omega)e^{i(kx-\omega t)} - BgH^3 h_0(-ik^3)e^{i(kx-\omega t)} = 0. \end{cases}$$

Division by $e^{i(kx-\omega t)}$ and simplification yields

$$\begin{cases} -h_0\omega + kP_0 = 0, \\ (-\omega)P_0 + kgHh_0 - \left(B + \frac{1}{3}\right) H^2 P_0 k^2\omega + k^3 BgH^3 h_0 = 0, \end{cases}$$

$$\Rightarrow (-\omega)P_0 + kgH\left(\frac{kP_0}{\omega}\right) - \left(B + \frac{1}{3}\right) H^2 P_0 k^2\omega + k^3 BgH^3\left(\frac{kP_0}{\omega}\right) = 0,$$

$$\Rightarrow \left(1 + \left(B + \frac{1}{3}\right) k^2 H^2\right)\omega^2 = gH\left(1 + Bk^2H^2\right)k^2, \tag{6.25}$$

$$\Rightarrow c^2 = \left(\frac{\omega}{k}\right)^2 = gH\frac{1 + B(kH)^2}{1 + \left(B + \frac{1}{3}\right)(kH)^2}. \tag{6.26}$$

Equation (6.25) is the dispersion relation for Schäffer and Madsen's model, and the phase velocity is given as (6.26) . Similarly, the dispersion relation and the phase velocity for other models can be derived.

6.4.2 Comparison of Models

By letting the solution to the Boussinesq equations be a small amplitude periodic wave, we obtain the phase velocity $v_p = \omega/k$. For the Schäffer and Madsen's model [124], we have

$$c^2 = gH\frac{1 + B(kH)^2}{1 + \left(B + \frac{1}{3}\right)(kH)^2}, \tag{6.27}$$

as derived above.

In case of the Nwogu model [107], a similar derivation gives

$$c^2 = gH\frac{1 - \left(\alpha + \frac{1}{3}\right)(kH)^2}{1 - \alpha(kH)^2}. \tag{6.28}$$

The phase velocity for the Serre's equations of Bonneton [17] is

$$c^2 = gH\frac{1 + \frac{\gamma-1}{3}(kH)^2}{1 + \frac{\gamma}{3}(kH)^2}. \tag{6.29}$$

The optimal values for the parameters α, B and γ can be determined with respect to the exact phase speed of the Airy wave theory given by

$$c^2 = gH\frac{\tanh(kH)}{kH}. \tag{6.30}$$

For example, Nwogu found the optimal value $\alpha = -0.390$ by minimizing the sum of the relative error of phase speed in the range of $0 \leq h/\lambda_0 \leq 0.5$. Madsen and Sørenson [96] found the optimal value $B = 1/15$ by matching Padé expansion of (6.30). Bonneton et al. [17] found the optimal value $\gamma = 1.159$ by minimizing the error in the range of $0 \leq kH \leq 4$. Each optimal values can be used for other equations. For example, $\alpha = -0.390$ corresponds to the value $B = 0.39 - 1/3 \approx 0.0567$ and $\gamma = 1.17$.

In Figure 6.2, we compare normalized phase speeds for the Schäffer and Madsen's Boussinesq equation for different parameter B. The error is phase velocity error with respect to the Airy wave theory.

6.5 Numerical Scheme for the Boussinesq Equation

In order to solve the Boussinesq type equation numerically, most of the previous work is based on finite difference schemes. For example, Nwogu [107] used the Crank-Nicholson

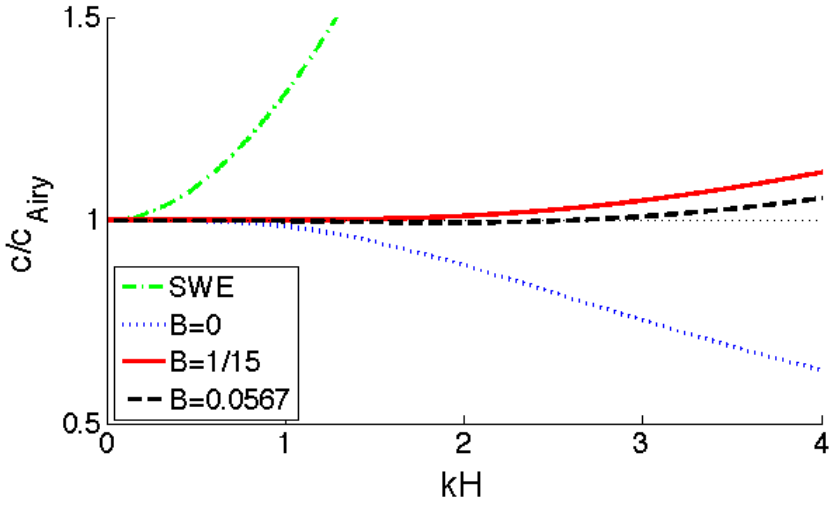

Figure 6.2: Comparison of normalized phase speeds for the Schäffer and Madsen's Boussinesq equation from (6.27).

method, and Madsen and Sørenson [96] employed a time-centered implicit scheme. Gobbi and Kirby [51] and Lynett and Liu [90] used a predictor-corrector scheme, employing a third order in time explicit Adams-Bashforth predictor step, and a fourth order in time Adams-Moulton implicit corrector step. Fuhrman and Madsen [94] used finite difference spatial discretizations, combined with the classical fourth-order, four-stage, explicit Runge-Kutta time stepping scheme.

The drawbacks of finite difference schemes are explained in Shi et al. [126]. Shi et al. pointed out that this scheme is noisy and weakly unstable to high wave numbers, and also it is difficult to implement wave breaking at surf zone and interaction of runup with beach slope.

Recently, numerical schemes have been developed incorporating finite volume methods and finite difference methods. For instance, Bonneton et al. [17] derived a modified Serre's equations and developed a hybrid numerical scheme for the 1-dimensional case. Shi et al. [126] developed a hybrid numerical scheme for the Boussinesq equations. Dutykh et al. [36] applied this type of numerical scheme to KdV-BBM equations and validated through

comparison to the analytical solutions. In this section, we will introduce a hybrid numerical scheme with stability studies.

6.5.1 Hybrid scheme of finite volume and finite difference methods

KdV-BBM equation

Consider the generalized KdV-BBM equation,

$$u_t + \alpha u_x + \beta u u_x - \gamma u_{txx} + \delta u_{xxx} = 0.$$

This can be rearranged as follows,

$$(1 - D)\left(u_t + \alpha u_x + \frac{\beta}{2}\left(u^2\right)_x\right) + \left(\alpha\gamma u_{xx} + \frac{\beta\gamma}{2}(u^2)_{xx} + \delta u_{xx}\right)_x = 0,$$

where $D = \gamma\partial_{xx}^2$ is a differential operator, and α, β, γ and δ are parameters. Let $u_t + \alpha u_x + \frac{\beta}{2}\left(u^2\right)_x = -P$, then for smooth solution we have

$$u_t + \left(\alpha u + \frac{\beta}{2}u^2\right)_x + P = 0, \tag{6.31}$$

with

$$(1 - D)\, P = \left(\left(\alpha\gamma + \delta\right) u_{xx} + \frac{\beta\gamma}{2}(u^2)_{xx}\right)_x. \tag{6.32}$$

For our hybrid scheme, we solve

$$u_t + \left(\alpha u + \frac{\beta}{2}u^2\right)_x = 0,$$

using a finite volume scheme, and then update

$$\begin{cases} u_t + P = 0, \\ (1 - D)\, P = \left(\left(\alpha\gamma + \delta\right) u_{xx} + \frac{\beta\gamma}{2}(u^2)_{xx}\right)_x, \end{cases}$$

with a source term splitting scheme.

Boussinesq equations

We now consider 2-dimensional Boussinesq equations. The main idea is that we use a high resolution finite volume method for the non-linear shallow water part, and then apply a

finite difference method for the linear dispersive terms. To distinguish the dispersive terms, we can rearrange

$$
\begin{aligned}
&h_t + (hu)_x + (hv)_y = 0,\\
&(hu)_t + \left(hu^2 + \frac{g}{2}h^2\right)_x + (huv)_y + ghb_x + S_1 = 0,\\
&(hv)_t + \left(hv^2 + \frac{g}{2}h^2\right)_y + (huv)_x + ghb_y + S_2 = 0,
\end{aligned}
$$

and

$$
\begin{bmatrix} S_1 \\ S_2 \end{bmatrix} = \begin{bmatrix} I - D_1 & -D_2 \\ -D_3 & I - D_4 \end{bmatrix}^{-1} \begin{bmatrix} \Psi_1 \\ \Psi_2 \end{bmatrix},
$$

with

$$
\begin{aligned}
D_1 w &= \left(B + \frac{1}{2}\right) H^2 w_{xx} - \frac{1}{6}H^3 \left(\frac{w}{H}\right)_{xx},\\
D_2 w = D_3 w &= \left(B + \frac{1}{2}\right) H^2 w_{xy} - \frac{1}{6}H^3 \left(\frac{w}{H}\right)_{xy},\\
D_4 w &= \left(B + \frac{1}{2}\right) H^2 w_{yy} - \frac{1}{6}H^3 \left(\frac{w}{H}\right)_{yy}.
\end{aligned}
$$

and

$$
\begin{aligned}
\Psi_1 = &\left(B + \frac{1}{2}\right) H^2 \left((hu^2)_x + g(h\eta_x) + (huv)_y\right)_{xx}\\
&+ \left(B + \frac{1}{2}\right) H^2 \left((hv^2)_y + g(h\eta_y) + (huv)_x\right)_{xy}\\
&- \frac{1}{6}H^3 \left(\frac{(hu^2)_x + gh\eta_x + (huv)_y}{H}\right)_{xx} - \frac{1}{6}H^3 \left(\frac{(hv^2)_y + gh\eta_y + (huv)_x}{H}\right)_{xy}\\
&- BgH^2 \left((H\eta_x)_{xx} + (H\eta_y)_{xy}\right) - \frac{1}{2}H^2 \bar{h}_{xtt},\\
\Psi_2 = &\left(B + \frac{1}{2}\right) H^2 \left((hv^2)_y + g(h\eta_y) + (huv)_x\right)_{yy}\\
&+ \left(B + \frac{1}{2}\right) H^2 \left((hu^2)_x + g(h\eta_x) + (huv)_y\right)_{xy}\\
&- \frac{1}{6}H^3 \left(\frac{(hv^2)_y + gh\eta_y + (huv)_x}{H}\right)_{yy} - \frac{1}{6}H^3 \left(\frac{(hu^2)_x + gh\eta_x + (huv)_y}{H}\right)_{xy}\\
&- BgH^2 \left((H\eta_y)_{yy} + (H\eta_x)_{xy}\right) - \frac{1}{2}H^2 \bar{h}_{ytt}.
\end{aligned}
$$

In the first step, we solve the shallow water equations,

$$\begin{aligned} h_t + (hu)_x + (hv)_y &= 0, \\ (hu)_t + \left(hu^2 + \frac{g}{2}h^2\right)_x + (huv)_y + ghb_x &= 0, \\ (hv)_t + \left(hv^2 + \frac{g}{2}h^2\right)_y + (huv)_x + ghb_y &= 0. \end{aligned}$$

With the same time step Δt determined from shallow water equations, we update the dispersion by solving

$$\begin{aligned} h_t &= 0, \\ (hu)_t + S_1 &= 0, \\ (hv)_t + S_2 &= 0, \end{aligned}$$

with

$$\begin{bmatrix} S_1 \\ S_2 \end{bmatrix} = \begin{bmatrix} I - D_1 & -D_2 \\ -D_3 & I - D_4 \end{bmatrix}^{-1} \begin{bmatrix} \Psi_1 \\ \Psi_2 \end{bmatrix}.$$

We use Godunov splitting in general, but Strang splitting can be used to achieve higher order of accuracy.

Numerical difficulties arise when we solve a linear system with the matrix

$$\mathcal{D} = \begin{bmatrix} I - D_1 & -D_2 \\ -D_3 & I - D_4 \end{bmatrix}.$$

Let the number of grid cells in x and y direction be N and M and use the second order accurate centered discretization for the spatial derivatives. In the 1-dimensional case, this scheme is still efficient as the matrix $\mathcal{D}$ is an $N \times N$ tridiagonal matrix which can be solved in $O(N)$ operations instead of $O(N^3)$. In 2-dimensions, the matrix $\mathcal{D}$ is a $2MN \times 2MN$ block tridiagonal matrix, and computing the exact factorization of this matrix can be obtained in $O((MN)^3)$ operations.

6.5.2 Large System Solvers

Since the matrix is a sparse matrix, we may use an approximate solver such as GMRES or bi-conjugate gradient method. The efficiency of GMRES largely depends on the pre-

conditioner used, and the appropriate pre-conditioner for this system requires more investigation.

If the matrix is not too large compared to the memory of the machine, direct solvers can be as fast as approximate solvers. If we use fixed grids, then we solve systems with the same matrix $\mathcal{D}$ for every time step. In these cases, it is desirable to find a factorization once and use the information again in every step. Direct solvers have this advantage, and we use a direct solver such as MUMPS [2], which stands for Multifrontal Massively Parallel sparse direct Solver.

6.6 Wave Breaking and Wet/dry Interface

When generated waves are approaching a coastal area, the amplitude of the waves becomes larger and they may steepen and break. To handle the possibility of wave breaking and shock formation, we switch from the Boussinesq equations to the shallow water equations. We follow Tonelli and Petti [134] who suggested basing the switching threshold on Froude number analysis. When the ratio of wave amplitude to undisturbed water depth exceeds 0.8, we switch to the shallow water equations.

One of the purposes of tsunami modeling is to predict inundation on coastal area where the wet/dry interface problem must be solved correctly. In the wet/dry situations, we use the shallow water equations rather than the Boussinesq type equations since the dispersion of waves is not clear in those situations. Moreover, the shallow water equations with HLLE scheme or with GEOCLAW have the very desirable depth positivity property.

6.7 Adaptive Mesh Refinement (AMR)

A powerful tool in efficient tsunami modeling is to use mesh refinement in some areas. While relatively coarse grids can capture tsunami propagation in the deep ocean, fine grids are necessary in the coastal area. As waves enter into coastal area, the wave speed decreases with roughly the square root of depth, and thus waves are compressed. The compressed waves have larger amplitude and shorter wave length than those in the deep ocean, and fine scale bathymetry is required to be handled in order to forecast inundation correctly. However, using fine grids in the entire ocean is inefficient in global scale tsunami modeling.

Adaptive refinement methods in general use different grid sizes depending on the nature of solutions in different domains. These schemes can be applied to highly localized problems such as often arise in hyperbolic systems. George, LeVeque, Berger and Mandli [48, 86] extended *Berger-Colella-Oliger* [14, 12] adaptive mesh refinement approach used in CLAWPACK to tsunami modeling, and created a package called GEOCLAW. In the AMR scheme, some required properties include conservation of mass and momentum, and preservation of steady states. Details on these properties with GEOCLAW can be found in George, Berger and LeVeque [48, 13] for example. The GEOCLAW software has shown its efficiency and accuracy through several benchmark problems and field studies. See González et al. [52], George [48], Macinnes et al. [93], and Arcos and LeVeque [4], for example.

6.7.1 Adaptive Mesh Refinement and Boussinesq Equations

Using Boussinesq equations in the entire domain is computationally expensive because solving a large sparse system is involved in the Boussinesq solver. Alternatively we prefer to apply the Boussinesq equations in specific areas, and those areas are often coastal region. As noticed in Figure 6.2, the difference between the shallow water equations and the Boussinesq equations is small if $kH \ll 1$ where tsunamis in general are under this regime. As waves move into the coastal area, waves are compressed and have larger amplitude and smaller wavelength, and therefore the value kH increases. For larger kH, the Boussiesq type equations are better approximation for waves.

There are several difficulties when AMR schemes are applied to the Boussinesq equations. In general, AMR schemes use several grid patches that can be overlap and have different grid sizes, and they are easily applicable to the localized PDE system such as the shallow water equations. If the dispersion correction terms are smaller compared to the shallow water terms, then small difference is expected between uniformly fine grids and AMR.

6.8 Stability and Convergence

6.8.1 Stability Study with von Neumann Analysis

Numerical tests with KdV-BBM equations may exhibit instabilities as the grid is refined if a centered discretization in space is used. In order to investigate stability and convergence of our numerical scheme, we consider a simple PDE as follows,

$$u_t + u_x = u_{txx}. \tag{6.33}$$

We arrange the equation (6.33) as

$$(I - D^2)(u_t + u_x) + D^2 u_x = 0,$$

where $D^2 = \partial_x^2$. For smooth u, we have

$$\begin{cases} u_t + u_x + P_x = 0, \\ (I - D^2)P = D^2 u. \end{cases}$$

We solve the advection equation

$$u_t + u_x = 0, \tag{6.34}$$

with a high resolution finite volume method, then update with a splitting scheme by solving the following equation with a finite difference scheme

$$u_t + P_x = 0, \tag{6.35}$$

$$(I - D^2)P = D^2 u. \tag{6.36}$$

If we use the second order accurate centered discretization for the operator D and apply an upwind scheme for P_x using the upwind direction suggested by the advection equation (6.34), then we have

$$\frac{u_j^{n+1} - u_j^n}{k} + \frac{P_j^n - P_{j-1}^n}{h} = 0, \tag{6.37}$$

$$\text{with} \quad P_j^n - \frac{P_{j+1}^n - 2P_j^n + P_{j-1}^n}{h^2} = \frac{u_{j+1}^n - 2u_j^n + u_{j-1}^n}{h^2} \tag{6.38}$$

where $h = \Delta x$ and $k = \Delta t$.

The von Neumann stability analysis is based on Fourier analysis, and thus can be applied to the linear PDE. Set $u_j^n = e^{i\xi jh}$ and $P_j^n = \alpha e^{i\xi jh}$, then equation (6.38) is

$$\alpha\left[e^{i\xi jh} - \frac{e^{i\xi(j+1)h} - 2e^{i\xi jh} + e^{i\xi(j-1)h}}{h^2}\right] = \frac{e^{i\xi(j+1)h} - 2e^{i\xi jh} + e^{i\xi(j-1)h}}{h^2},$$

$$\Rightarrow \quad \alpha = \frac{\frac{2}{h^2}\left(\cos(\xi h) - 1\right)}{1 - \frac{2}{h^2}\left(\cos(\xi h) - 1\right)} = \frac{2\left(\cos(\xi h) - 1\right)}{h^2 - 2\left(\cos(\xi h) - 1\right)}. \tag{6.39}$$

The equation (6.37) leads to

$$g(\xi)e^{i\xi jh} = e^{i\xi jh} - \frac{k}{h}\alpha\left(e^{i\xi jh} - e^{i\xi(j-1)h}\right).$$

Simplification and replacing α with (6.39) yields

$$\begin{aligned}
g(\xi) &= 1 - \frac{k}{h}\alpha\left(1 - \cos(\xi h) + i\sin(\xi h)\right), \\
|g(\xi)|^2 &= \left(1 - \frac{k}{h}\alpha(1 - \cos(\xi h))\right)^2 + \left(\frac{k}{h}\alpha\sin(\xi h)\right)^2 \\
&= 1 - 2\frac{k}{h}\alpha(1 - \cos(\xi h)) + \left(\frac{k}{h}\alpha\left(1 - \cos(\xi h)\right)\right)^2 + \left(\frac{k}{h}\alpha\sin(\xi h)\right)^2 \\
&= 1 - \frac{2k\alpha}{h}(1 - \cos(\xi h)) + \left(\frac{k\alpha}{h}\right)^2(2 - 2\cos(\xi h)) \\
&= 1 - \frac{2k\alpha}{h}(1 - \cos(\xi h))\left(1 - \frac{k\alpha}{h}\right) \\
&= 1 + \frac{4k\left(\cos(\xi h) - 1\right)^2}{h\left(h^2 - 2\left(\cos(\xi h) - 1\right)\right)}\left(1 - \frac{2k\left(\cos(\xi h) - 1\right)}{h\left(h^2 - 2\left(\cos(\xi h) - 1\right)\right)}\right) > 1, \quad \text{for } 0 < \xi h < 2\pi.
\end{aligned}$$

Since $(\cos(\xi h) - 1) < 0$, we conclude that this scheme is unstable.

Suppose instead we apply the centered discretization for P_x so that (6.37) is replaced by

$$\frac{u_j^{n+1} - u_j^n}{k} + \frac{P_{j+1}^n - P_{j-1}^n}{2h} = 0. \tag{6.40}$$

The equation (6.40) turns to

$$g(\xi)e^{i\xi jh} = e^{i\xi jh} - \frac{k}{2h}\alpha\left(e^{i\xi(j+1)h} - e^{i\xi(j-1)h}\right).$$

Simplification and replacing α with (6.39) yields

$$\begin{aligned}
g(\xi) &= 1 - i\frac{\alpha k}{h}\left(\sin(\xi h)\right), \\
|g(\xi)| &\geq 1.
\end{aligned}$$

Thus this scheme is not stable as well.

Next we apply a 1-sided scheme for P_x in place of (6.37)

$$\frac{u_j^{n+1} - u_j^n}{k} + \frac{P_{j+1}^n - P_j^n}{h} = 0, \tag{6.41}$$

using what appears to be the down-wind direction. Then equation (6.41) becomes

$$g(\xi)e^{i\xi jh} = e^{i\xi jh} - \frac{k}{h}\alpha\left(e^{i\xi(j+1)h} - e^{i\xi jh}\right).$$

Simplification and replacing α with (6.39) yields

$$\begin{aligned}
g(\xi) &= 1 - \frac{k}{h}\alpha\left(\cos(\xi h) - 1\right) - i\frac{k}{h}\alpha\sin(\xi h), \\
|g(\xi)|^2 &= \left(1 - \frac{k}{h}\alpha(\cos(\xi h) - 1)\right)^2 + \left(\frac{k}{h}\alpha\sin(\xi h)\right)^2 \\
&= 1 - 2\frac{k}{h}\alpha(\cos(\xi h) - 1) + \left(\frac{k}{h}\alpha\left(\cos(\xi h) - 1\right)\right)^2 + \left(\frac{k}{h}\alpha\sin(\xi h)\right)^2 \\
&= 1 - \frac{2k\alpha}{h}(\cos(\xi h) - 1) + \left(\frac{k\alpha}{h}\right)^2(2 - 2\cos(\xi h)) \\
&= 1 - \frac{2k\alpha}{h}(\cos(\xi h) - 1)\left(1 + \frac{k\alpha}{h}\right) \\
&= 1 - \frac{4k\left(1 - \cos(\xi h)\right)^2}{h\left(h^2 + 2\left(1 - \cos(\xi h)\right)\right)}\left(1 - \frac{2k\left(1 - \cos(\xi h)\right)}{h\left(h^2 + 2\left(1 - \cos(\xi h)\right)\right)}\right).
\end{aligned}$$

If $k < h + \frac{h^3}{4}$, then $|g(\xi)| \leq 1$ and thus this scheme is stable.

Thus this numerical scheme is stable when the upwind method is employed in the opposite direction to that suggested by the advection term. This seemingly opposite direction can be explained as we carefully look into the system. The equation (6.36) can be written as

$$\mathbf{u}_t + (I - D^2)^{-1}D^2\mathbf{u}_x = 0,$$

with

$$D^2 = \frac{1}{h^2}\begin{bmatrix}
-2 & 1 & & & \\
1 & -2 & 1 & & \\
 & \ddots & \ddots & \ddots & \\
 & & 1 & -2 & 1 \\
 & & & 1 & -2
\end{bmatrix}.$$

Since the matrix $(I - D^2)^{-1}D^2$ is negative definite, the opposite upwind direction is in fact the correct direction. Note that the dispersion relation is

$$\omega = \frac{k}{1+k^2}.$$

The phase velocity, c_p, is,

$$c_p = \frac{\omega}{k} = \frac{1}{1+k^2},$$

and the group velocity, c_g, is equal to

$$c_g = \frac{\partial \omega}{\partial k} = \frac{1-k^2}{(1+k^2)^2} = 1 - \frac{k^2(3+k^2)}{(1+k^2)^2} < 1.$$

Since the advection speed is 1, most energy propagates to the left relative to the advection speed. In Figure 6.3, the solution to the PDE (6.33) is shown at $t = 100$ with Gaussian initial shape. We observe that all wavelengths propagate slower than the advection velocity 1.

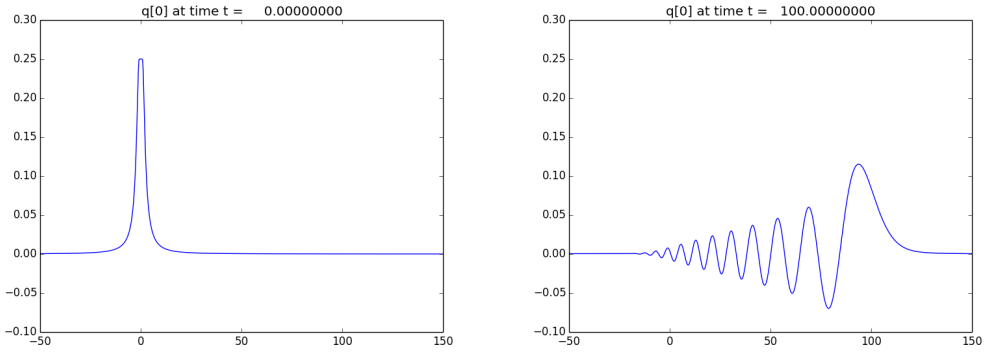

Figure 6.3: Plot of solution to PDE (6.33). Initial condition (left) and at $t = 100$ s (right). Initial shape is Gaussian, and the grid size Δx is equal to $1/2$.

This upwind-like method is stable, but it is only $O(\Delta x)$ accurate. Alternately, the centered difference approximation can be used for spatial discretization, and a Runge-Kutta scheme is employed for time discretization. Also recall that the equation (6.36) is obtained through integration for smooth u. Although the integration process is straight forward for

this simple PDE, it is often complicated for a set of Boussinesq type equations, and thus we return to the original form. If we set $S(x) = -(u_t + u_x)$, then we have

$$\begin{cases} u_t + u_x + S = 0, \\ \left(I - D^2\right) S = D^3 u. \end{cases} \tag{6.42}$$

Assume we use the centered difference approximation of $O(\Delta x^2)$ accuracy, and the 4-stage Runge-Kutta scheme for time stepping. Then we have,

$$\begin{aligned} U_1 &= u^n \\ U_2 &= u^n - \frac{k}{2} S_1, \quad \text{where} \quad (I - D^2) S_1 = D^3 U_1, \\ U_3 &= u^n - \frac{k}{2} S_2, \quad \text{where} \quad (I - D^2) S_2 = D^3 U_2, \\ U_4 &= u^n - k S_3, \quad \text{where} \quad (I - D^2) S_3 = D^3 U_3, \\ u^{n+1} &= u^n - \frac{k}{6} \left[S_1 + 2S_2 + 2S_3 + S_4 \right], \quad \text{where} \quad (I - D^2) S_4 = D^3 U_4. \end{aligned}$$

For each step, S_i's are computed from

$$(S_i)_j - \frac{(S_i)_{j+1} - 2(S_i)_j + (S_i)_{j-1}}{h^2} = \frac{u_{j+2} - 2u_{j+1} + 2u_{j-1} - u_{j-2}}{2h^3}.$$

In order to investigate the stability, replace $u_j = e^{i\xi jh}$ and $(S_1)_j = \alpha e^{i\xi jh}$. Then we have

$$\begin{aligned} \alpha \left(e^{i\xi jh} - \frac{e^{i\xi(j+1)h} - 2e^{i\xi jh} + e^{i\xi(j-1)h}}{h^2} \right) &= \frac{e^{i\xi(j+2)h} - 2e^{i\xi(j+1)h} + 2e^{i\xi(j-1)h} - e^{i\xi(j-2)h}}{2h^3}, \\ \alpha \left(1 - \frac{-2 + 2\cos(\xi h)}{h^2} \right) &= \frac{\sin(2\xi h) - 2\sin(\xi h)}{h^3} i, \\ \alpha &= \frac{-2\sin(\xi h)(1 - \cos(\xi h))}{h^3 + 2h(1 - \cos(\xi h))} i := \beta i. \end{aligned}$$

for some real β. If we replace the 4-stage Runge-Kutta scheme with $u_j = e^{i\xi jh}$ and $(S_1)_j = \alpha e^{i\xi jh}$, then we have

$$\begin{aligned} S_1 &= \alpha e^{i\xi jh}, \quad U_2 = \left(1 - \frac{k\alpha}{2} \right) e^{i\xi jh} \\ S_2 &= \alpha \left(1 - \frac{k\alpha}{2} \right) e^{i\xi jh}, \quad U_3 = \left(1 - \frac{k\alpha}{2} + \frac{(k\alpha)^2}{4} \right) e^{i\xi jh} \\ S_3 &= \alpha \left(1 - \frac{k\alpha}{2} + \frac{(k\alpha)^2}{4} \right) e^{i\xi jh}, \quad U_4 = \left(1 - k\alpha + \frac{(k\alpha)^2}{2} - \frac{(k\alpha)^3}{4} \right) e^{i\xi jh} \\ S_4 &= \alpha \left(1 - k\alpha + \frac{(k\alpha)^2}{2} - \frac{(k\alpha)^3}{4} \right) e^{i\xi jh}. \end{aligned}$$

Thus the growth factor $g(\xi)$ is

$$g(\xi) = 1 - \frac{k}{6}\left(\alpha + 2\alpha\left(1 - \frac{k\alpha}{2}\right) + 2\alpha\left(1 - \frac{k\alpha}{2} + \frac{(k\alpha)^2}{4}\right) + \alpha\left(1 - k\alpha + \frac{(k\alpha)^2}{2} - \frac{(k\alpha)^3}{4}\right)\right)$$
$$= 1 - \frac{1}{6}\left(6k\alpha - 3(k\alpha)^2 + (k\alpha)^3 - \frac{(k\alpha)^4}{4}\right).$$

Since $\alpha = \beta i$ for some real β, setting $X = k\beta$ yields,

$$g(\xi) = 1 - \frac{1}{2}X^2 + \frac{X^4}{24} + \left(\frac{X^3}{6} - X\right)i$$
$$|g(\xi)|^2 = 1 + \frac{1}{4}X^4 + \frac{X^8}{24^2} - X^2 + \frac{X^4}{12} - \frac{X^6}{24} + X^2 + \frac{X^6}{36} - \frac{X^4}{3}$$
$$= 1 - \frac{1}{72}X^6 + \frac{1}{576}X^8.$$

If $|x| < 2\sqrt{2}$, then $|g(\xi)| < 1$. Since $X = k\beta$, the sufficient condition for stability is

$$\left|\frac{k}{h}\frac{\sin(\xi h)(1 - \cos(\xi h))}{h^2 + 2(1 - \cos(\xi h))}\right| < \sqrt{2}, \quad \text{for } \forall \quad \xi h. \tag{6.43}$$

For small h, this condition is approximately

$$\frac{k}{h} < 2\sqrt{2}.$$

6.9 Convergence Studies

We investigate the convergence of our numerical scheme with analytical solutions from KdV-BBM equation and Serre's equations. In numerical simulation, Strang splitting is applied in the source term computation.

6.9.1 KdV-BBM equation

Consider the generalized KdV-BBM equation,

$$u_t + \alpha u_x + \beta u u_x - \gamma u_{txx} + \delta u_{xxx} = 0, \tag{6.44}$$

where α, β, γ and δ are non-negative constants. The solitary wave solution to the KdV-BBM equation has the form

$$u(x,t) = 3\frac{c - \alpha}{\beta}\text{sech}^2\left(\frac{1}{2}\sqrt{\frac{c - \alpha}{\gamma c + \delta}}(x - ct)\right),$$

where c is the speed of traveling wave.

When $\alpha = \beta = \gamma = 1$ and $\delta = 0$, the equation (6.45) is called as Benjamin-Bona-Mahony (BBM) equation which is

$$u_t + u_x + uu_x - u_{txx} = 0. \tag{6.45}$$

We can rearrange

$$(I - D^2)\left(u_t + \left(u + \frac{1}{2}u^2\right)_x\right) + D^2\left(u + \frac{1}{2}u^2\right)_x = 0.$$

A single solitary wave with $c = 1.1$ is tested for this numerical test, and the CFL number is fixed at 0.70. Figure 6.4 shows the ∞-norm and 2-norm errors with $t = 100$ which are measured by

$$E^{\infty} = \frac{||h_{num} - h_{sol}||_{\infty}}{||h_{sol}||_{\infty}}, \quad E^2 = \frac{||h_{num} - h_{sol}||_2}{||h_{sol}||_2},$$

where h_{num} and h_{sol} are numerical and exact solutions respectively.

Table 6.1 shows the convergence rate, and the grid size Δx is varying from 1 to 1/256. We clearly observe convergence to the exact solutions as we increase the number of cells, and the convergence rate is 2.

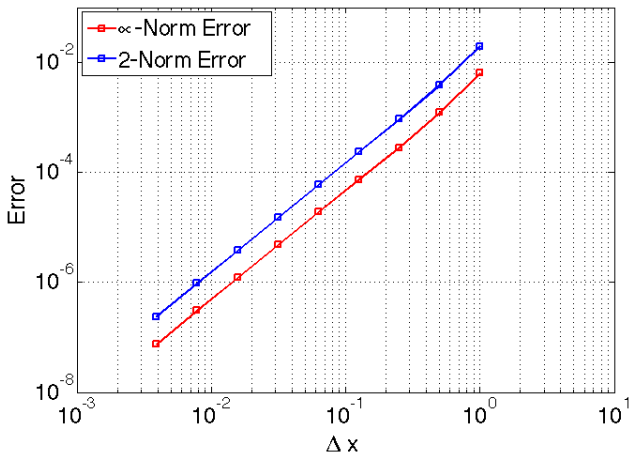

Figure 6.4: Plot of ∞-norm and 2-norm errors for the BBM equation (6.45) with $c = 1.1$ and at time $t = 100$. Grid size Δx varies from 1 to 1/256.

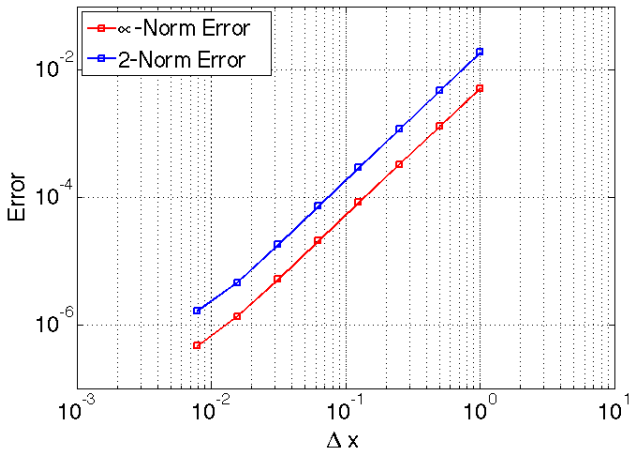

Figure 6.5: Plot of ∞-norm and 2-norm errors for the KdV-BBM equation (6.46) with $c = 1.1$ and at time $t = 100$. Grid size Δx varies from 1 to 1/256.

Next we include the u_{xxx} term and let $\alpha = \beta = \gamma = \delta = 1$. Then the equation is written as

$$u_t + u_x + uu_x - u_{txx} + u_{xxx} = 0. \tag{6.46}$$

The same test is performed, and Figure 6.5 shows the ∞- and 2-norm errors at $t = 100$. Table 6.2 shows the convergence rate which is again approximately 2.

We have tested two cases of KdV-BBM equation with single solitary wave propagation. Through these numerical tests, we have shown that our numerical scheme is stable for $k/h < 1$, and second order accurate.

6.9.2 Serre's Equations

Serre's equations have solitary wave solutions when the bathymetry is constant. If $(b(x))_x \equiv 0$, then Serre's equations are written as

$$h_t + (hu)_x = 0, \tag{6.47}$$

$$(hu)_t + \left(hu^2 + \frac{g}{2}h^2\right)_x = \frac{1}{3}\left(h^3\left(u_{xt} + uu_{xx} - (u_x)^2\right)\right)_x. \tag{6.48}$$

Δx	Rate(E^∞)	Rate(E^2)
1/2	2.3998	2.3298
1/4	2.1116	2.0678
1/8	1.9431	1.9761
1/16	1.9436	1.9811
1/32	1.9757	1.9985
1/64	1.9909	1.9947
1/128	1.9992	1.9898
1/256	2.0176	1.9983

Table 6.1: Convergence rate for BBM equation. ($\alpha = \beta = \gamma = 1$ and $\delta = 0$)

Δx	Rate(E^∞)	Rate(E^2)
1/2	1.9711	2.0150
1/4	1.9850	2.0121
1/8	2.0006	2.0063
1/16	1.9911	2.0027
1/32	2.0085	1.9997
1/64	1.9329	1.9851
1/128	1.5385	1.4778
1/256	1.9536	1.9988

Table 6.2: Convergence rate KdV-BBM equation. ($\alpha = \beta = \gamma = \delta = 1$)

Using the fact that

$$h^3 u_{xt} = h^2(hu)_{xt} + h^2(hu)_{xx}u - hh_x(hu)_t - hh_x(hu)_x u + h^2(hu)_x u_x,$$

the momentum equation (6.48) can be rewritten as

$$\begin{aligned}(hu)_t - \frac{1}{3}\left(h^2(hu)_{xt} - hh_x(hu)_t\right)_x + \left(hu^2 + \frac{g}{2}h^2\right)_x \\ = \frac{1}{3}\left(h^2(hu)_{xx}u - hh_x(hu)_x u + h^2(hu)_x u_x + h^3 u u_{xx} - h^3(u_x)^2\right)_x .\end{aligned}$$

If we define the operator D as

$$Dw = -\frac{1}{3}\left(h^2 w_x - hh_x w\right)_x ,$$

we have

$$\begin{aligned}(1+D)\left((hu)_t + \left(hu^2 + \frac{g}{2}h^2\right)_x\right) - D\left(hu^2 + \frac{g}{2}h^2\right)_x \\ = \frac{1}{3}\left(h^2(hu)_{xx}u - hh_x(hu)_x u + h^2(hu)_x u_x + h^3 u u_{xx} - h^3(u_x)^2\right)_x .\end{aligned}$$

After simplification, Serre's equations can be written as follows

$$
\begin{aligned}
&h_t + (hu)_x = 0,\\
&(hu)_t + \left(hu^2 + \frac{g}{2}h^2\right)_x = P,\\
&(1+D)P = \frac{1}{3}\left[-2h^3(u_x)^2 - gh^3h_{xx}\right]_x.
\end{aligned}
$$

The exact solitary wave solutions are given as,

$$
\begin{aligned}
&h(x,t) = H + h_0\mathrm{sech}^2(\kappa(x-ct)),\\
&u(x,t) = c\left(1 - \frac{h_0}{h(x,t)}\right),\\
&\kappa = \frac{\sqrt{3H}}{2h_0\sqrt{h_0+H}}, \quad c = \sqrt{g(H+h_0)},
\end{aligned}
$$

where H is the undisturbed depth of water, and h_0 is the initial amplitude of the wave.

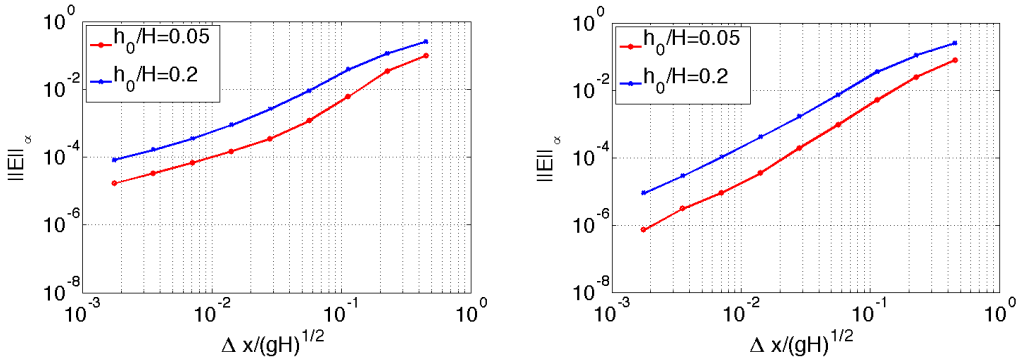

Figure 6.6: Maximum relative error for two cases $h_0/H = 0.05$ (red) and $h_0/H = 0.2$ (blue) with Godunov splitting (left) and Strang splitting(right).

We performed the same numerical tests suggested by Bonneton et al. [17]. We test two cases where h_0/H is equal to 0.05 and 0.2 with $H = 0.5$, and the CFL number is fixed at 0.70. The grid size Δx is varying from 1 to 1/256, and maximum errors are measured at $t = 3$.

In Figure 6.6, we show the maximum errors with Godunov splitting (left) and Strang splitting (right) in the dispersive terms computation. Tables 6.3 and 6.4 show the convergence rate for each case. With these splitting schemes, we observe the convergence rate

Δx	$h_0/H = 0.05$	$h_0/H = 0.2$
1/2	1.5166	1.1478
1/4	2.5343	1.5484
1/8	2.3364	2.1109
1/16	1.7737	1.7809
1/32	1.2395	1.5620
1/64	1.1057	1.3271
1/128	1.0454	1.1036
1/256	1.0001	1.0105

Table 6.3: Convergence rate with Godunov splitting

Δx	$h_0/H = 0.05$	$h_0/H = 0.2$
1/2	1.6786	1.2081
1/4	2.2685	1.6151
1/8	2.4053	2.2818
1/16	2.3207	2.1284
1/32	2.4768	2.0187
1/64	1.9259	1.9930
1/128	1.5649	1.8507
1/256	2.1219	1.6909

Table 6.4: Convergence rate with Strang splitting.

with Godunov splitting is between 1 and 2. Strang splitting shows the convergence rate is less than 2 but clearly larger than that of Godunov splitting.

6.10 Implicit Scheme

We consider implicit schemes, and compare the same results from the previous sections. We test with the KdV-BBM equation (6.46) given as

$$u_t + u_x + uu_x - u_{txx} + u_{xxx} = 0.$$

As a choice of the implicit scheme, we use 2nd order diagonally implicit Runge-Kutta(DIRK) scheme with 2nd order centered discretization for the space.

We consider the same soliton problem with $c = 1.1$ and $\Delta t/\Delta x = 1$, and measure ∞-norm error at $t = 100$. In Figure 6.7, the error is shown from DIRK2 and our numerical scheme. We notice the error from our numerical scheme is smaller than with the DIRK2 scheme, and convergence rate is larger than with the DIRK2 scheme.

The error from the DIRK2 can be reduced as we set $\Delta t/\Delta x$ smaller. When the grid size is fixed at $\Delta x = 1/4$, the errors from our previous numerical scheme are 5.263×10^{-4}

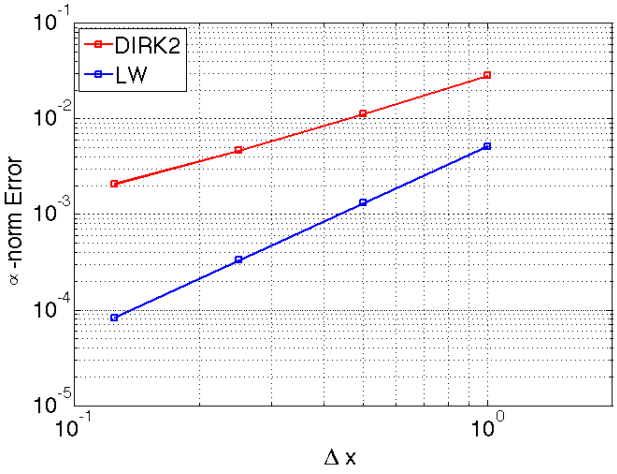

Figure 6.7: Comparison of the ∞-norm errors of DIRK2 (red) and our hybrid scheme (blue).

$\Delta t/\Delta x$	∞-norm error	2-norm error
1	4.682×10^{-3}	1.411×10^{-2}
1/2	2.688×10^{-3}	8.327×10^{-3}
1/4	1.731×10^{-3}	5.714×10^{-3}
1/8	1.264×10^{-3}	4.559×10^{-3}
1/16	1.058×10^{-3}	4.049×10^{-3}

Table 6.5: DIRK2 errors vs. $\Delta t/\Delta x$ with $\Delta x = 1/4$ fixed.

in ∞-norm and 1.881×10^{-3} in 2-norm. Table 6.5 shows the errors from the DIRK2 while $\Delta t/\Delta x$ is varying from 1 to 1/16. Even if we set $\Delta t/\Delta x = 1/16$, the errors are still larger than our numerical scheme.

6.11 Computational Cost Comparison

In this section, computational speeds are compared with the shallow water equations solver and the Boussinesq solver. In solving the shallow water equations, GEOCLAW software is employed. In solving the Boussinesq-type equations, large matrix solver is required and two

methods are used. In this work, MUMPS and GMRES have been chosen as a direct solver and an iterative solver respectively.

Computational domain in this section is $[-100, 100] \times [-100, 100]$ and the bathymetry is a parabola shape bowl given as $z(x, y) = z_{min} \cdot (x^2 + y^2) \cdot 1.25 \times 10^{-4} - z_{min}$ where z_{min} is the depth of the bowl. The initial condition of the water is a Gaussian shape hump with maximum height equal to η_0, and no momentum is imposed with $u = v = 0$. The CFL number is fixed at 0.8 for the numerical tests in this section.

GMRES is an approximate iterative solver, and tolerance can be chosen which is a convergence criterion. In Figure 6.8, a semi log plot of errors of GMRES versus computational cost is shown. The true solution is computed with the direct solver, MUMPS, and the error is measured as

$$Error = \frac{\|\eta_{approx} - \eta_{true}\|_2}{\|\eta_{true}\|_2}.$$

And the error is computed at $t = 10$ with two cases $\eta_0 = 2$ and $\eta_0 = 10$. In both cases, similar computational time is required for the same error bounds.

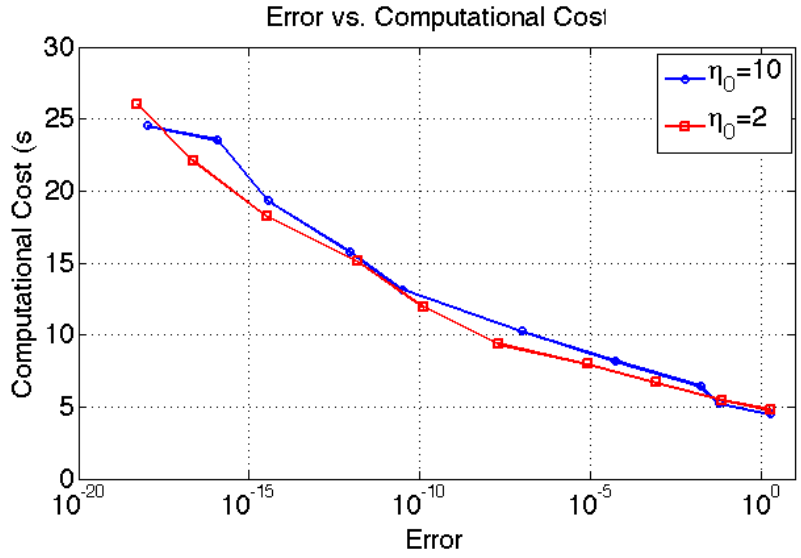

Figure 6.8: Semilog plot of the GMRES error versus computational cost. Two cases with $\eta_0 = 2$ and $\eta_0 = 10$ are tested, and error is measured at $t = 10$.

Next, computational costs of GEOCLAW, MUMPS and GMRES are compared with a uni-

form grid. One of the advantages of using a direct solver is observed when the computational domain is fixed. If the adaptive mesh refinement scheme is not used, then the computational domain does not change over time, and the factorization of a matrix only needs to be computed once and can be used repeatedly at every time step. In Table 6.6, computational costs are compared when different numerical schemes are used. Since the dispersive wave computation is not involved in shallow water equations, the computation of a factorization of a large sparse matrix is not required, and thus GEOCLAW is fastest. The direct solver MUMPS is comparable to GEOCLAW when the factorization of the matrix is computed only once. If the computation of the factorization is required at every time step, the efficiency deteriorates drastically as the size of a matrix increases. Thus MUMPS is an efficient method for a fixed grid, and an iterative solver such as GMRES can be a better choice for AMR.

Grid	GEOCLAW	MUMPS	MUMPS*	GMRES(10^{-4})	GMRES(10^{-8})
50×50	0.605	0.792	3.567	0.86	1.076
100×100	3.164	4.337	36.098	6.803	10.297
200×200	24.908	32.007	522.697	74.788	137.047
300×300	66.069	103.975	3515.953	402.122	807.055

Table 6.6: Comparison of numerical schemes with fixed computational domain. The unit of computational time is in second. For GEOCLAW, the shallow equations are solved without dispersion. For MUMPS, the factorization of the matrix is computed once and reused. In the case of MUMPS*, the factorization is computed for every time step. In GMRES, there is an option for the tolerance, and two cases are tested with tolerance equal to 10^{-4} and 10^{-8}.

In dispersive wave computations, one major difficulty with AMR is in that the solution is not local so that the solutions may be different if they are computed in different grids. In next numerical test, two results from a uniform grid and a subdivision of grid into patches will be compared.

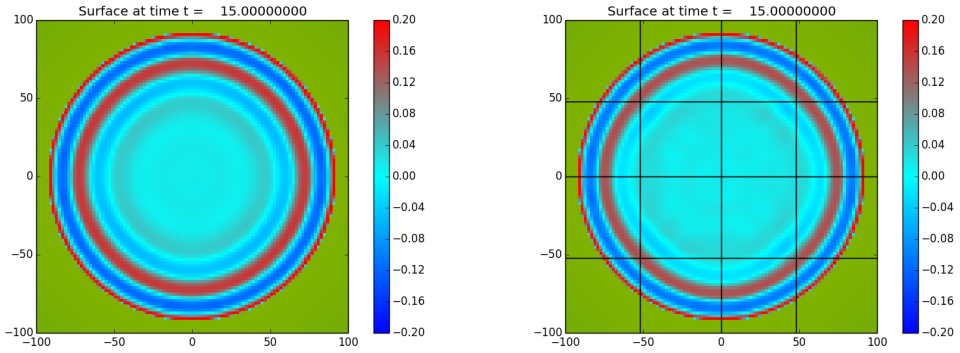

Figure 6.9: Snapshot at $t = 15$

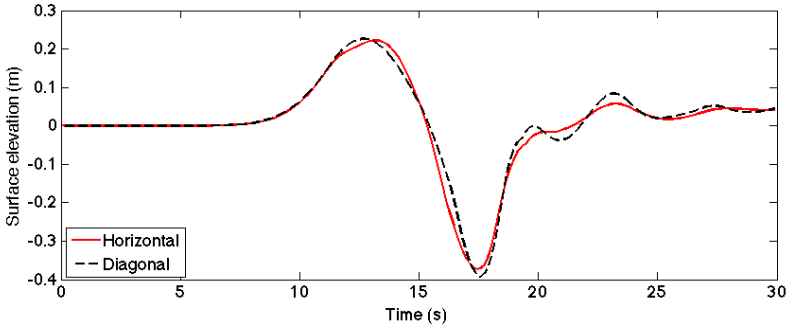

Figure 6.10: Comparison of horizontal and diagonal gauges.

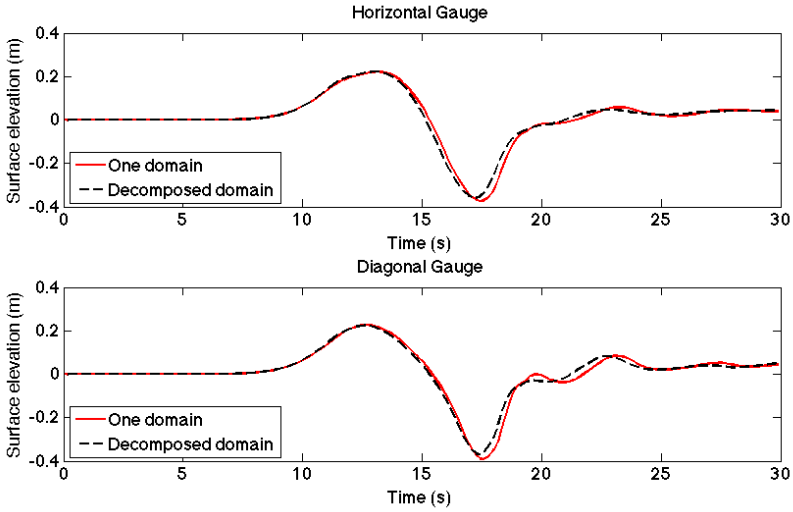

Figure 6.11: Gauge plot with one domain and sixteen subdomain cases

Chapter 7

ONE-DIMENSIONAL NUMERICAL TESTS

In this chapter, several numerical tests are performed on wave propagation problems. The first example is the solitary wave propagation without a change of bathymetry, and the Boussinesq type equations are validated through comparison with laboratory data. The other examples are about waves generated by submarine landslides. If the submarine landslide is a rigid-body, then the one-way coupled model is employed. If the submarine landslide is composed of granular materials, then the fully-coupled model is also considered.

7.1 Benchmark Problem 5

Several benchmark problems were suggested in the NTHMP benchmarking project [52]. Details of benchmark problems and numerical results from GEOCLAW can be found at `http://www.clawpack.org/links/nthmp-benchmarks/` for example.

In this benchmark problem 5, the bathymetry is piecewise linear, and a solitary wave is generated from the left boundary and solid wall is imposed on the right boundary. In Figure 7.1 the sketch of the water tank is shown.

In this work, two cases of benchmark problem (b) and (c) were considered. The difference between benchmark problem (b) and (c) is that the initial height of solitary waves are 0.30 m and 0.70 m respectively. The computational domain is between the gauge 4 and the right solid wall. Thus the left boundary condition is determined from the gauge 4 data in the laboratory experiment. We use 200×2 grid points without bottom friction, and compared the results from the shallow water equations and Boussinesq equations.

In Figure 7.2, 7.3, 7.4 and 7.5, we show gauge plots for benchmark problem 5 (b) and (c) where the locations of the gauges are shown in Figure 7.1. We observe that the results from the Boussinesq equations show dispersion of waves which is not reproducible with the shallow water equations. The wave arrival time is fairly correctly captured by two sets of

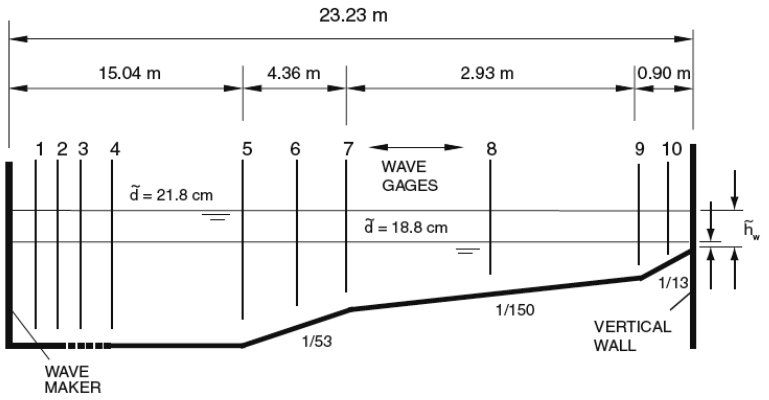

Figure 7.1: Sketch of the flume with gauge locations

equations.

In the computation of dispersive terms, there is a parameter which switches from the Boussinesq equations to the shallow water equations. Typically, if the ratio of the wave amplitude to the depth of water is greater than 0.8, then the shallow water equations are used. In the cases (b) and (c), two different thresholds have been chosen. The thresholds were 0.45 and 0.7 for the benchmark problem (b) and (c) respectively. If we switch to the shallow water equations, then smaller wave amplitude is expected. If a larger threshold is chosen, the reflected waves arrive at each gauge faster since larger wave amplitude is maintained. There are other schemes for the choice of thresholds with regard to the energy of waves. See Tonelli and Petti [134] for example.

In both cases, smaller wave amplitude is produced from numerical simulations for the reflected waves. The difference between the Boussinesq equations and the laboratory data is clearly observed at gauge 10, which is close to the solid wall boundary. At the solid wall, complex interactions are expected including wave breaking, and depth-averaged models are unable to capture these interactions correctly. But still, the results from the Boussinesq equations are in good agreement with the laboratory data.

In Figure 7.6 and 7.7, snapshots at $t = 5$ and $t = 8$ are shown. For Figure 7.6, we use centered difference in the spatial discretization of the dispersive terms, where we use the

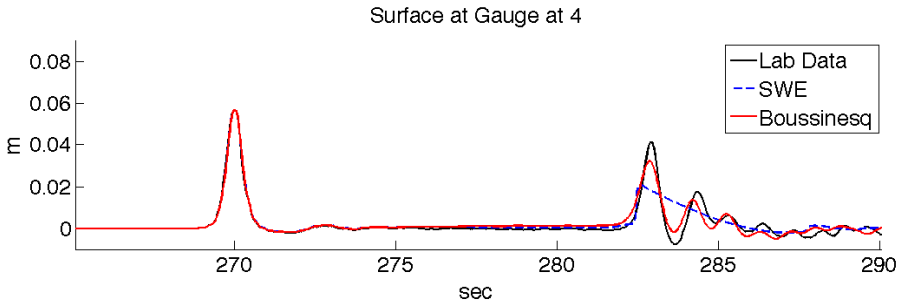

Figure 7.2: Gauge 4 plot for benchmark problem 5(b). Black line is laboratory data, dashed blue line is results from the shallow water equations, and solid red line is results from the Boussinesq equations.

four stage Runge-Kutta scheme (RK4) for Figure 7.7. We already have shown that central discretization may generate instability for a simple PDE. We observe similar instabilities when we use centered differencing with the Boussinesq equations. When we apply the RK4 scheme which was suggested in the previous chapter, we obtain a stable numerical scheme as shown in Figure 7.7.

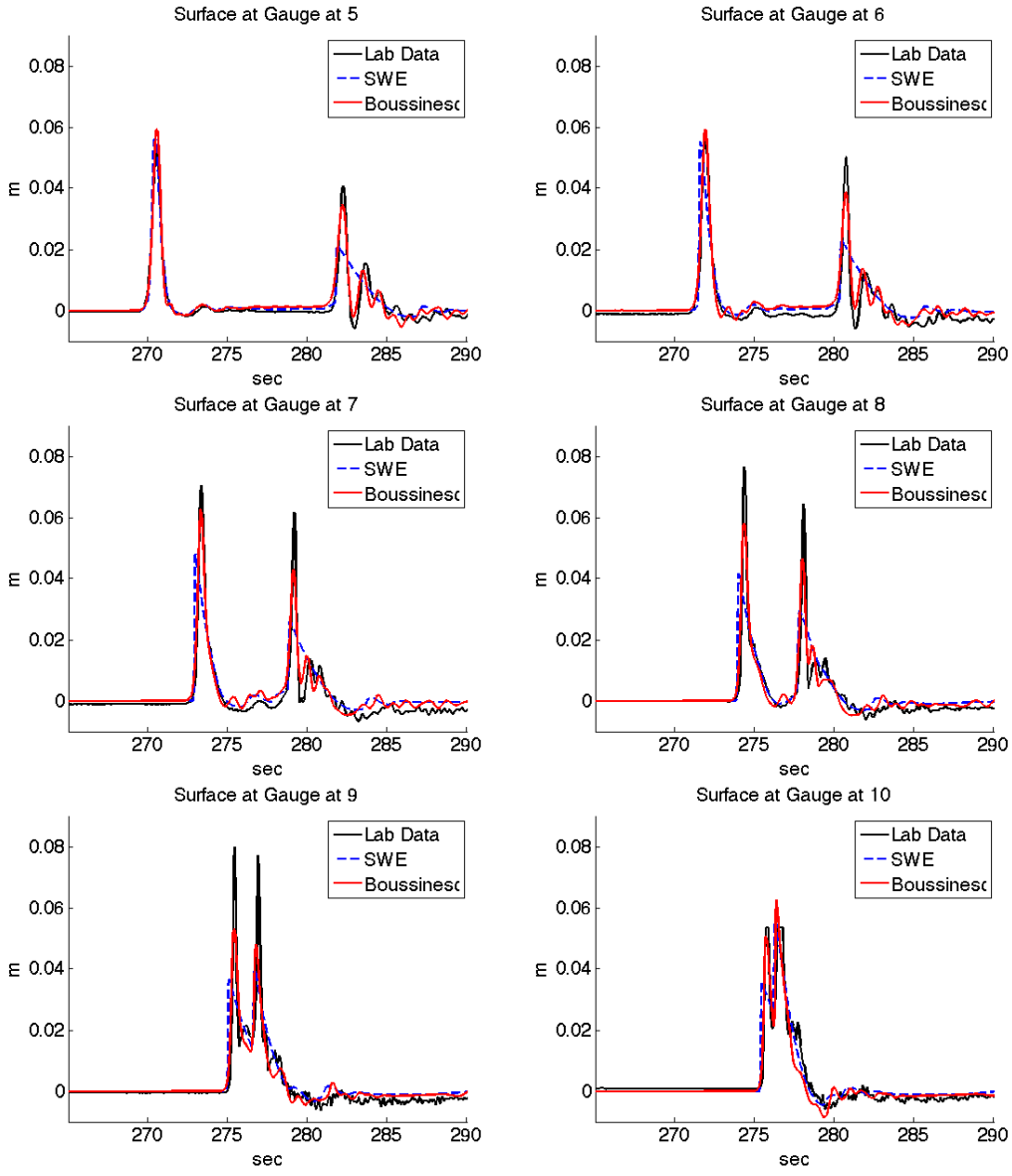

Figure 7.3: Gauge plots (5-10) for benchmark problem 5(b). Black line is laboratory data, dashed blue line is results from the shallow water equations, and solid red line is results from the Boussinesq equations.

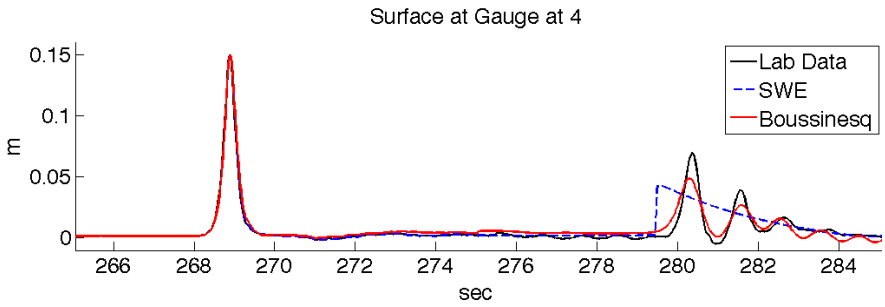

Figure 7.4: Gauge 4 plot for benchmark problem 5(c). Black line is laboratory data, dashed blue line is results from the shallow water equations, and solid red line is results from the Boussinesq equations.

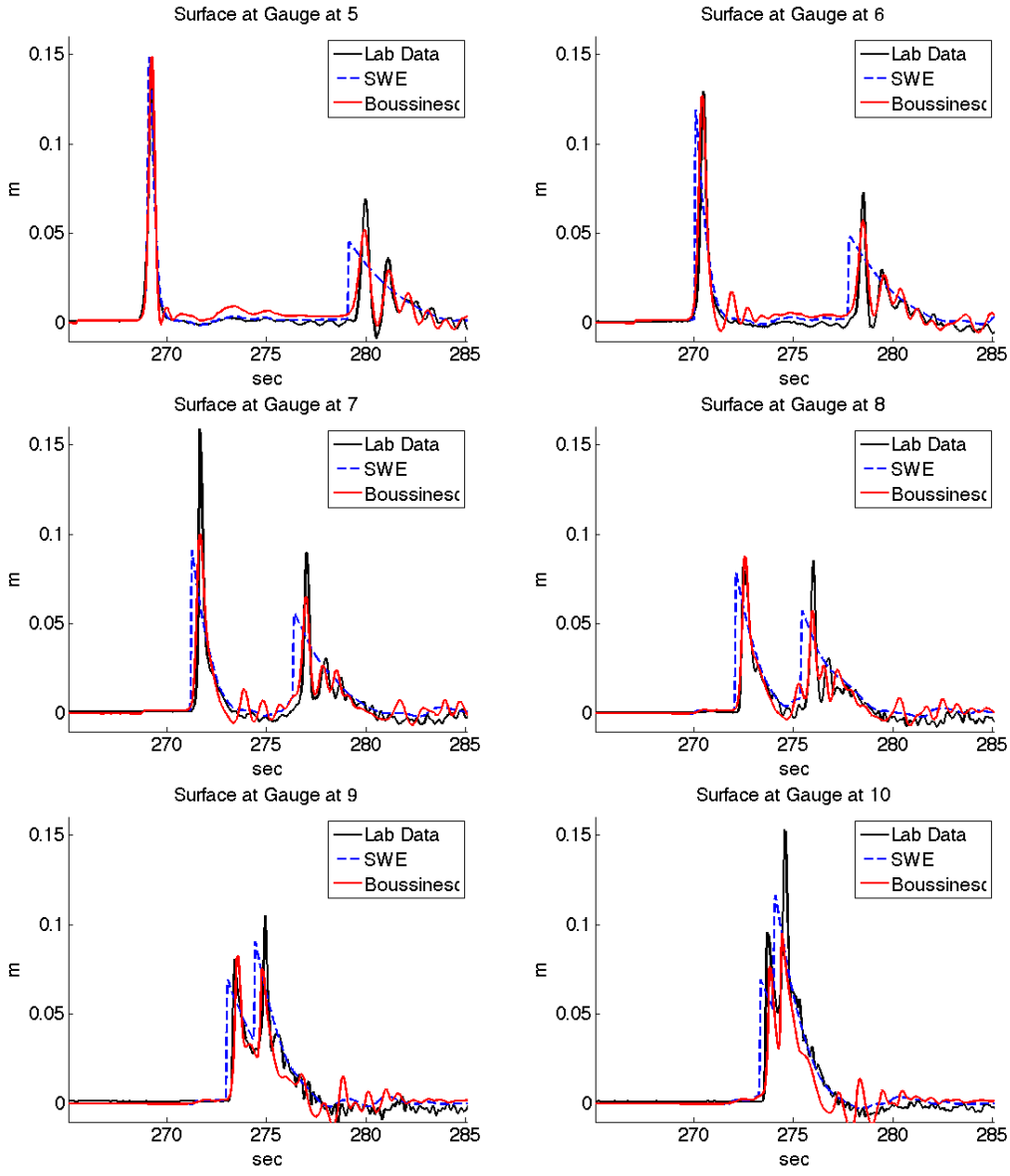

Figure 7.5: Gauge plots (5-10) for benchmark problem 5(c). Black line is laboratory data, dashed blue line is results from the shallow water equations, and solid red line is results from the Boussinesq equations.

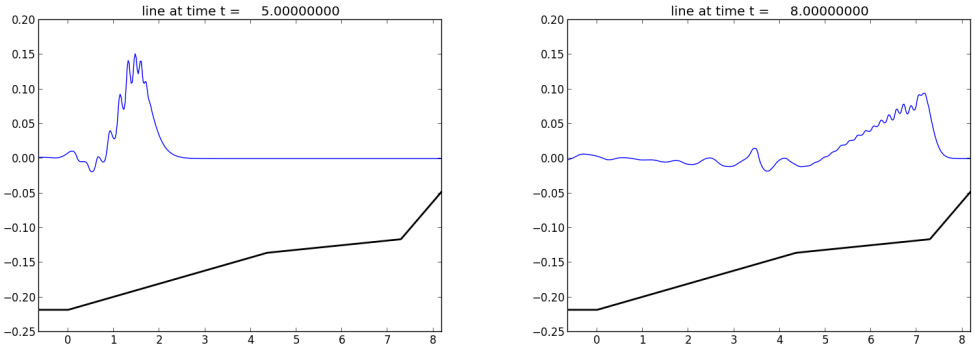

(a) $t = 5$ (b) $t = 8$

Figure 7.6: Snap shots at $t = 5$ and $t = 8$ for benchmark problem 5(c) with centered discretization in the finite difference method for source terms.

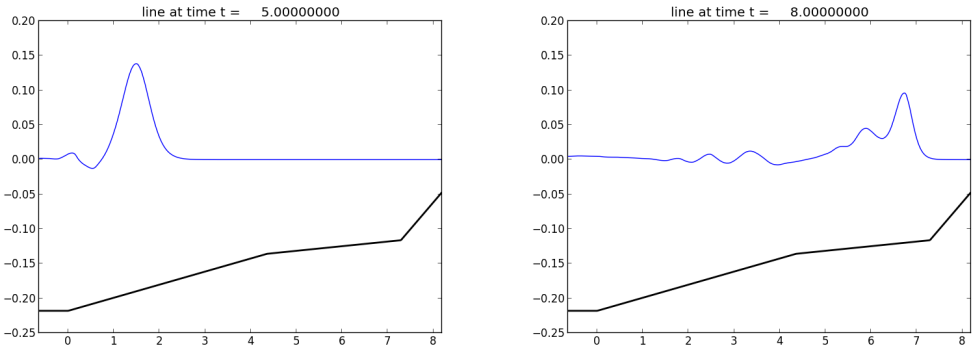

(a) $t = 5$ (b) $t = 8$

Figure 7.7: Snapshots at $t = 5$ and $t = 8$ for benchmark problem 5(c) with RK4 scheme in the finite difference method for source terms.

7.2 Lynett and Liu 2002

This is a small scale 1-D test problem on a mild slope proposed by Lynett and Liu [90]. The angle of slope is 6° and the initial distance from the slide to the water surface is 0.2114 m. The elliptic shape slide has 1 m of length and 0.05 m of maximum thickness.

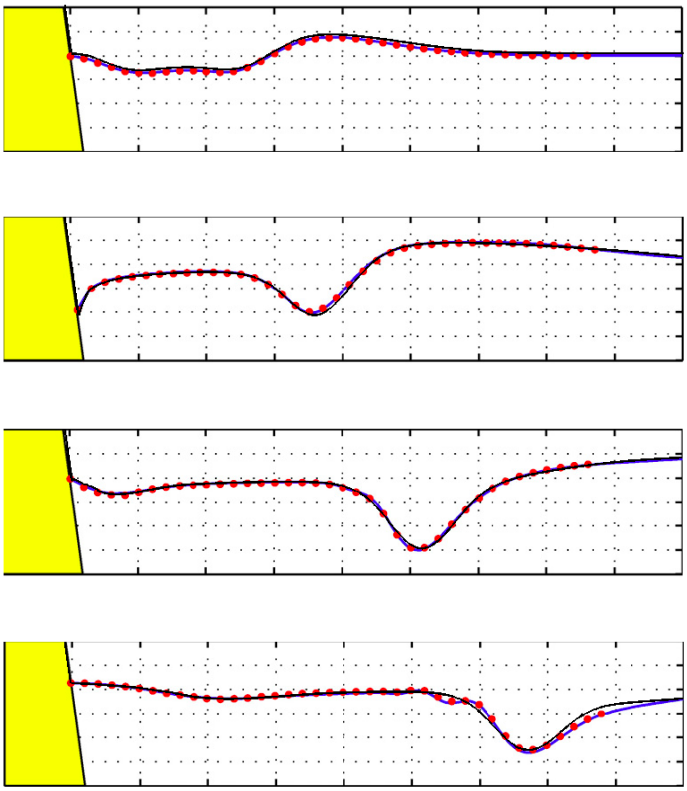

Figure 7.8: Lynett and Liu [90] results. SWE(black), Fuhrman and Madsen(blue) and experiment(red dots) at t=1.51 s, 3 s, 4.51 s and 5.86 s from top to bottom.

In Figure 7.8, we compare laboratory results and numerical results at t=1.51 s, 3 s, 4.51 s and 5.86 s from top to bottom respectively. For this problem, the shallow water equations are in good agreement with the experiment and the Boussinesq type equations. The waves generated by this submarine motion, shows that $k_c h = 0.55$ where k_c is the characteristic wave number. Since the generated wave is long enough, the shallow water equations shows

validity for this case, and the Boussinesq-type equations are not necessary.

7.3 Continental Shelf

Figure 7.9 is the bathymetry and the initial conditions of the landslide. The simplified ocean bathymetry is divided into four parts with different slopes. There are coastal area, continental shelf, continental slope and deep ocean. We fix the width and slope of the continental shelf so that it is 10000 meter wide with a mild slope of $1 : 150$. Continental slope area is parabolic such that the initial angle is $15°$ and the angle reaches zero as it reaches to the deep ocean. We impose non-reflecting boundary condition on the right.

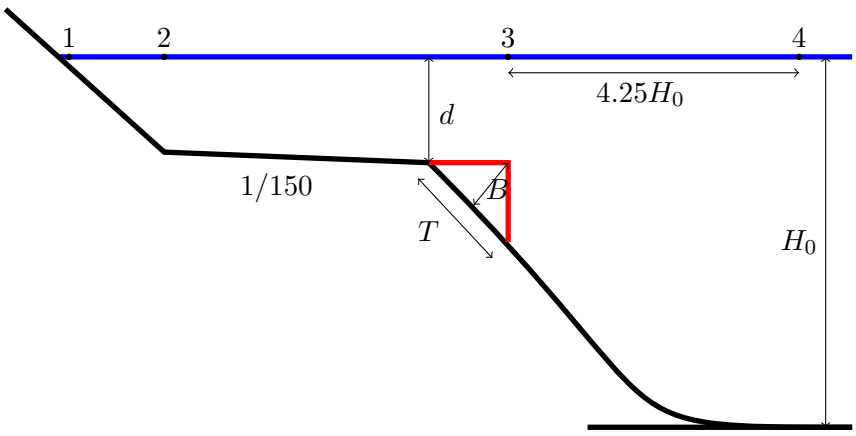

Figure 7.9: A sketch of the bathymetry. This is not to scale.

Four gauges are located to measure the amplitudes of waves as given in Figure 7.9 with the shoreline at $x = 0$. Gauge 1 is located close to the shoreline at $x = 100$, and gauge 2 is located where the bathymetry is changing from shore to continental shelf. The position of the gauge 3 is at the center of landslide, and gauge 4 is at $4.25H_0$ which measures the far-field waves as suggested by Watts' experiments [139]. For numerical computation, we employ 1000 grid points on the domain $[-2000, 28000]$.

The landslide layer is located at the edge of the continental shelf. Initially it is motionless having a wedge shape with base length T and the height B. We set $T = 1500$ and $B = 150$ so that the aspect ratio B/T is $1/10$, and the density of the landslide is 2000 kg/m^3. Here

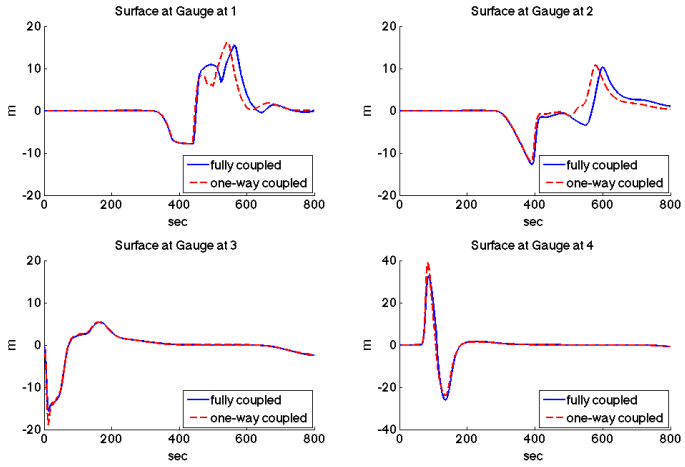

Figure 7.10: Surface elevation at gauges with the distance from the landslide to the surface $d = 100$. The viscous fluid model is employed for the submarine landslide with viscosity $5,000$ Pa·s.

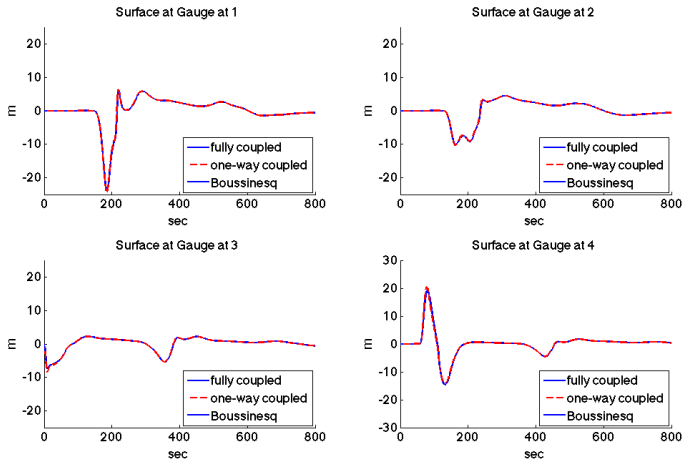

Figure 7.11: Surface elevation at gauges with the distance from the landslide to the surface $d = 500$. Viscous friction model is employed for the submarine landslide with viscosity $5,000$ Pa·s.

we used the viscous fluid model for the landslide with viscous coefficient $5,000\ Pa \cdot s$.

We are interested in comparing the performance of the coupled and uncoupled models as we vary the distance (d) from water surface to the landslide. In general, the depth of continental shelf varies, but is often limited to water shallower than 150 meter. On the contrary, Papua New Guinea 1998 tsunamis was induced by a landslide whose location is believed to be about 500 meter deep in the water. We vary d from 100 to 500 and compare tsunami waves generated by the submarine landslide. Figures 7.10 and 7.11 show gauge plots when the distance from the landslide to the water surface $d = 100$ and 500 respectively. The difference between the two models is relatively large for $d = 100$, but the difference is almost not noticed for $d = 500$.

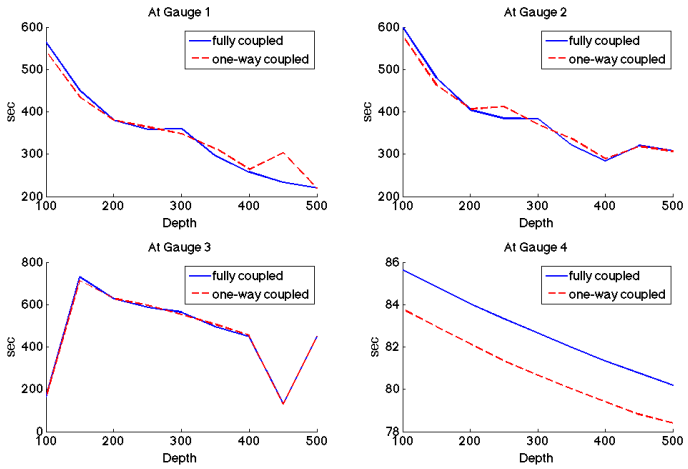

Figure 7.12: Arrival time of the first wave computed with the fully coupled and one-way coupled models as a function of the depth d in Figure 7.9. The viscous fluid model is employed for the submarine landslide with viscosity $5,000$ Pa·s.

Figure 7.12 is a plot of arrival time of the first wave at gauges 1 through 4, and we notice the difference between the fully coupled and one-way coupled models is small. Once waves are generated by the submarine slide, the arrival time is mainly governed by the shape of the bathymetry.

Figure 7.13 shows the maximum height of crests at the gauges. When d is less than 300,

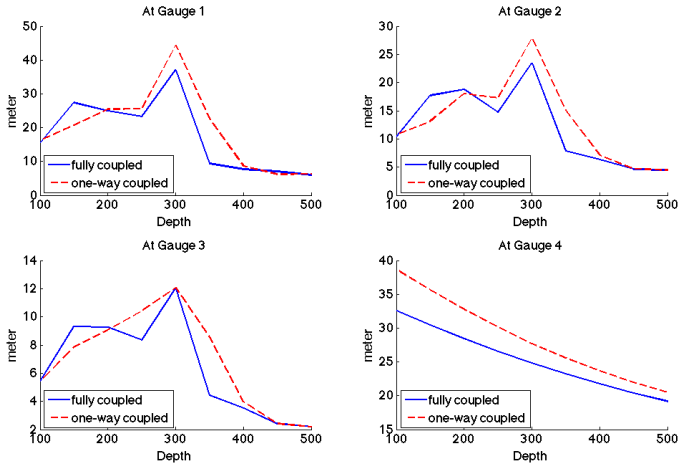

Figure 7.13: Maximum height of crests computed with the fully coupled and one-way coupled models as a function of the depth d in Figure 7.9. The viscous fluid model is employed for the submarine landslide with viscosity $5,000$ Pa·s.

a clear difference is observed between the fully coupled and one-way coupled models. The initial difference at gauge 3 increases as waves approach toward shoreline (gauge 1 and 2), and then is amplified with reflection. Except for the $d = 100$ case, we notice that the one-way model predicts larger amplitude of the crest than the fully coupled model. The one-way coupled system does not include the momentum transfer from the water column onto the landslide. Numerical results suggest that this momentum transfer becomes important when the distance from the top of the submarine landslide to the water surface is small.

In Figures 7.14, surface elevation at gauges are shown with the viscosity coefficient equal to 5×10^5 Pa·s. If viscosity is larger, then the submarine landslide moves slower and generates smaller waves. From the comparison between Figure 7.10 and 7.14, we observe that the difference between the fully coupled and one-way coupled models becomes smaller with larger viscosity.

Numerical results from one-way coupled model are similar to those from the fully coupled model. If d and viscosity are large, then the difference is significantly small. If d is small, some difference is observed for the waves propagating toward the shoreline, but it is relatively

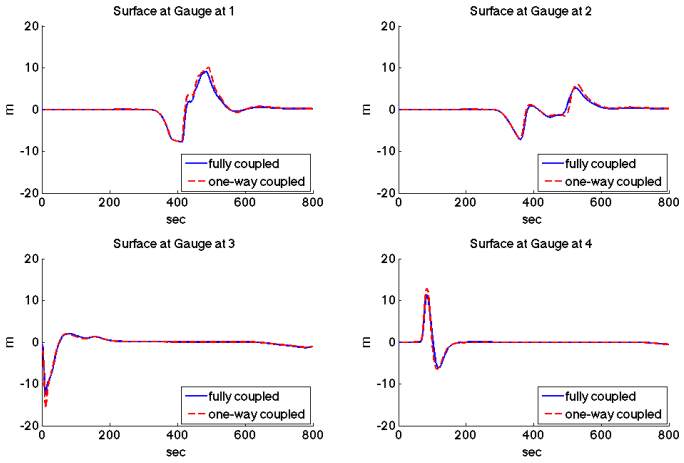

Figure 7.14: Surface elevation at gauges with the distance from the landslide to the surface $d = 100$. Viscous friction model is employed for the submarine landslide with viscosity 5×10^5 Pa·s.

small compared to the wave amplitude.

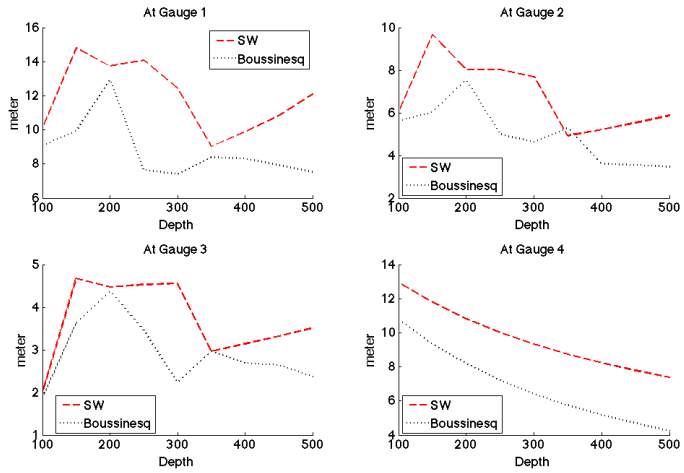

Figure 7.15: Maximum surface elevation computed from the shallow water and the Boussinesq models at gauges with viscosity 5×10^5 Pa·s.

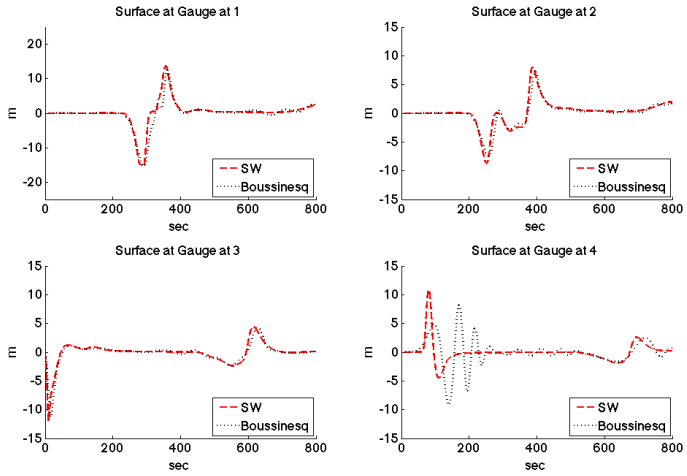

Figure 7.16: Surface elevation computed from the shallow water and and the Boussinesq models at gauges with $d = 200$ and viscosity 5×10^5 Pa·s.

In Figures 7.15 and 7.16, numerical results at gauges are plotted from the shallow water equations and the Boussinesq equations with the one-way coupled model. The maximum height of crest is plotted with the distance from slide to water surface in Figure 7.15. Smaller amplitudes are computed from the Boussinesq equations which results from the dispersion of waves. One specific case when $d = 200$ is plotted in Figure 7.16. Similar wave pattern is observed for those waves which are propagating toward shoreline at gauge 1 and 2. When the Boussinesq equations are employed, dispersion of waves is clearly perceived at gauge 4, and small amplitude at the crests and large amplitude at the troughs are observed.

7.4 Watts' Experiments

7.4.1 Laboratory experiments

Watts [139] investigated analysis and laboratory experiments on waves generated by underwater landslides. Watts derived an approximate solution based on Airy wave theory, and compared it with experiments. Solid body and granular materials have been used for laboratory experiments. A wedge shaped rigid body was used to generate waves with different

initial conditions. Beads with various diameter and crushed calcite were used to emulate granular materials.

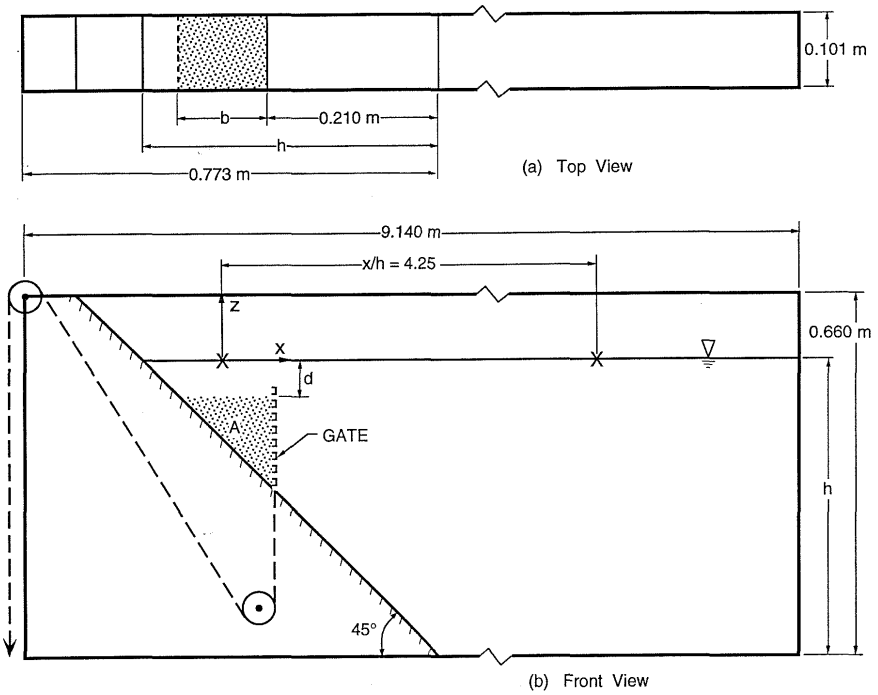

Figure 7.17: Schematic representation of water tank from Watts [139]. For the crushed calcite experiments, $b = 0.085$ and $d = 0.073$ have been chosen.

Watts performed experiments in a water tank illustrated in Figure 7.17. Since the water tank is narrow and long with landslide material filling the width of it, this experiment can be considered as a 2-dimensional problem that might be modeled with 1-dimensional shallow water equations. One wave gauge measures initial generation of waves, and another gauge assesses propagation of waves.

Among Watts' experiments, granular experiments are of the most interest. Beads and crushed calcite were used, and experiments with crushed calcite are appropriate because the Coulomb friction law can be applied. The initial suspension density of crushed calcite is $1,950$ kg/m^3, and the Coulomb friction angle is $20°$. In Figure 7.18, surface elevation at

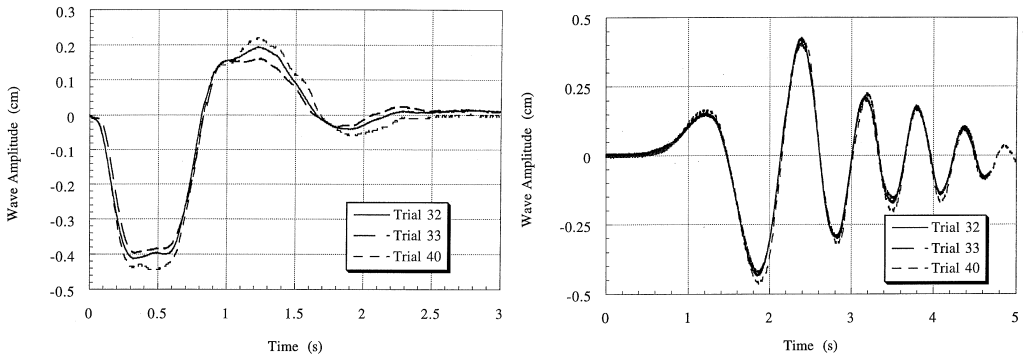

(a) Near-field gauge (b) Far-field gauge

Figure 7.18: Surface elevation at gauges from Watts' laboratory experiments of crushed calcite from Watts [139].

the gauges is shown from three experiments whose initial conditions are similar.

7.4.2 Numerical tests

In our numerical tests, we assume submarine landslide as a fluid of uniform density $1,950$ kg/m^3. The Coulomb friction law is applied with friction angle of $20°$. The size of grid cell is $\Delta x = 0.005$ with computational domain $[0, 3]$. Numerical tests are performed with the one-way coupled model shallow water and Boussinesq model. We do not use the fully coupled model because the system loses hyperbolicity. As the slope is steep with $45°$, the speed of slide becomes large, and the system is non-hyperbolic.

In Figure 7.19, we compare numerical results from the one-way coupled shallow water and Boussinesq model. At near-field gauge, we observe difference between numerical and laboratory tests. In numerical simulation, the trough is generated as soon as the landslide is released. The shallow water equations predict smaller amplitude at the trough and crest, and the crest is generated earlier than laboratory tests. With the Boussinesq equations, we observe very large amplitude at the trough, but the generation time and amplitude of crest is very similar to the experiments.

At the far field gauge, we observe clear difference between the shallow water and the

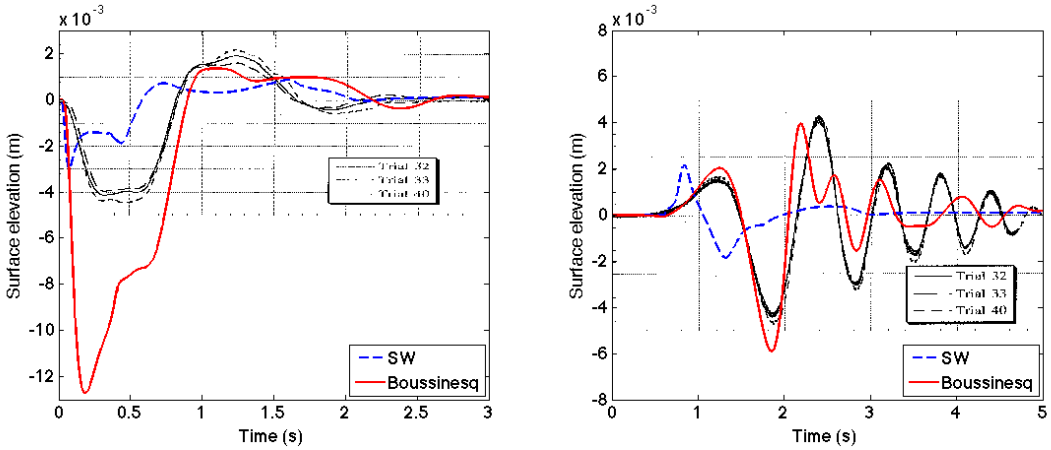

(a) Near-field gauge

(b) Far-field gauge

Figure 7.19: Surface elevation at gauges from the one-way coupled shallow water and Boussinesq model. We compared against laboratory experiments of Watts [139].

Boussinesq model. From the shallow water equations, dispersion of the wave is not observed. When the Boussinesq equations are applied, the numerical result is in much better agreement with laboratory experiments. At the near field gauge, the interaction between slide and water is important and the depth-average model may not be suitable.

Chapter 8

TWO-DIMENSIONAL NUMERICAL TESTS

8.1 Benchmark Problem 3

We consider benchmark problem 3 from NTHMP benchmark problems [52]. The slide is elliptic shape and placed on 15° slope. Figure 8.1 shows generated waves at t=0.8212 s and the location of gauges.

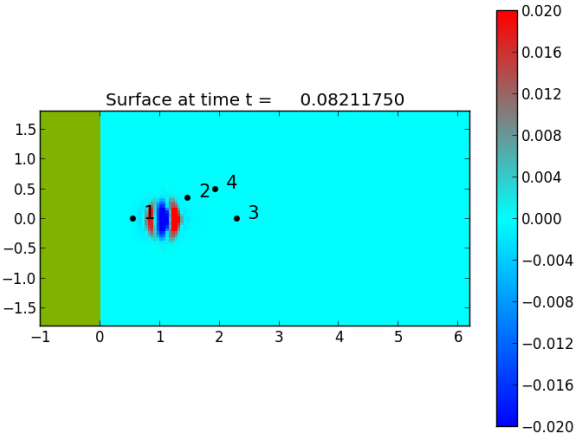

Figure 8.1: Sketch of the flume with gauge locations for the benchmark problem 3.

In Figure 8.2 and 8.3, the numerical results on the gauges are compared when the distance from water surface to slide block is 0.061 and 0.189 respectively. For these cases, we observe discrepancy between numerical results and laboratory data. The Boussinesq equations are slightly better than the shallow water equations. One of the reasons is that the generated waves have approximately $k_c h \approx 5$ at gauge 3, and $k_c h \approx 10$ at gauge 4. From the linear dispersion relation, we do not expect our Boussinesq model would be in good agreement with laboratory results for this range of $k_c H$.

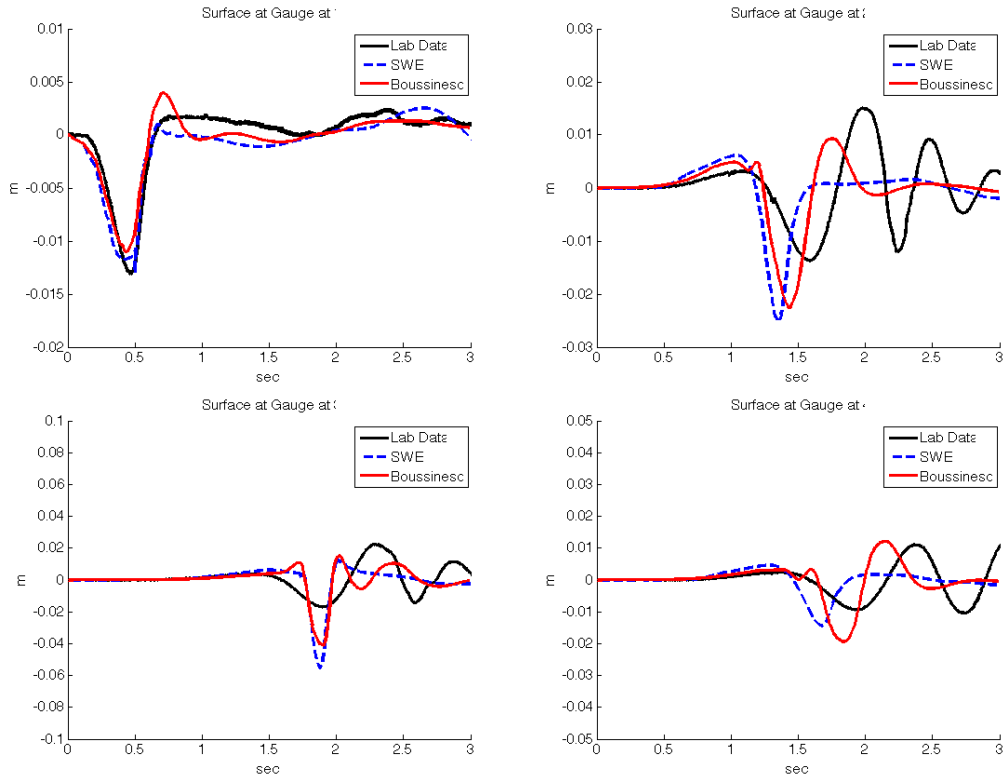

Figure 8.2: Computed and measured results for $d = 0.061$m.

8.2 Grilli et al. 2002

In this section we consider Grilli et al. [57] test for underwater slide generated tsunami. The laboratory experiments were performed in 1:1000 scale. The angle of slope is 15°, and the slide is ellipse shape with length $b = 1000$ m and maximum thickness $T = 52$ m.

In Figure 8.4, we show the gauge plots from different results. General patterns of waves are similar, but we still observe discrepancies between these results. One of the reasons can be found in the ambiguity of the submarine rigid body motion in Grilli et al's paper. And in the following work of Fuhrman and Madsen, the shape and motion of submarine slide is different from Grilli et al's work. For our numerical tests, we followed the description of Grilli et al.'s paper. In Figure 8.5, we compare the numerical results of the shallow water equations and Boussinesq equations at $t = 97.4$ s, 168.8 s and 197.2 s.

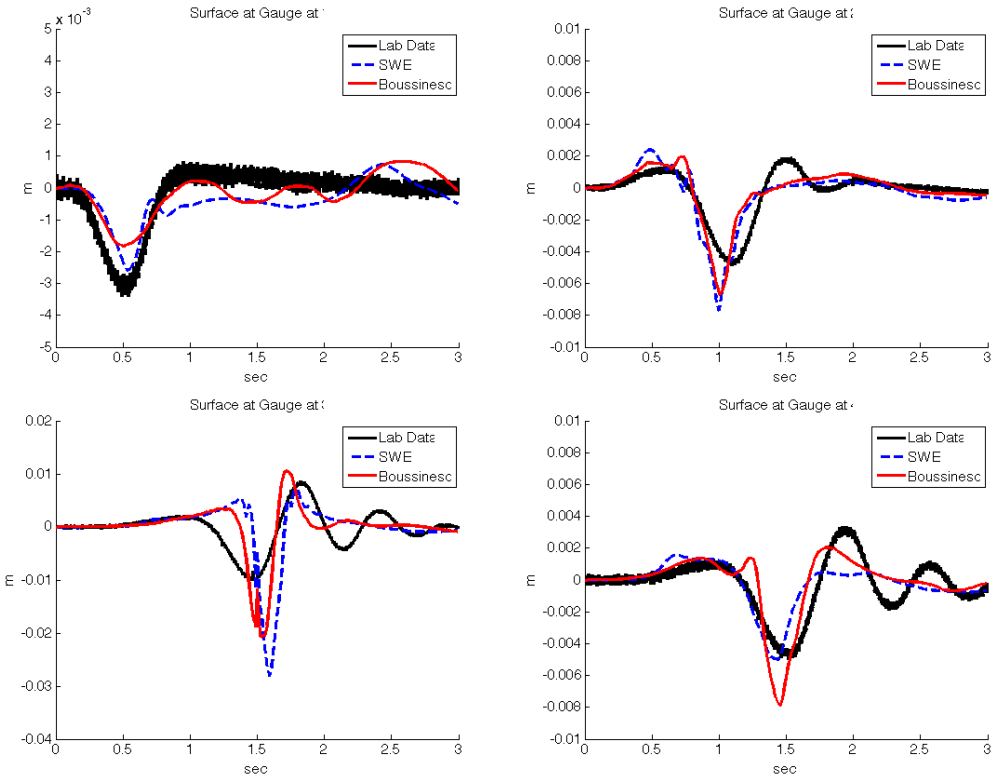

Figure 8.3: Computed and measured results for $d = 0.189$m.

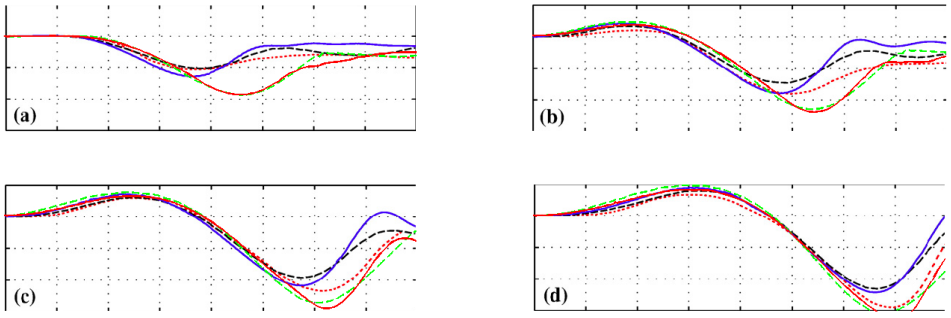

Figure 8.4: Gauge plots of modified Schäffer and Madsen(solid red), SWE(dashed green) Fuhrman and Madsen(solid blue), and numerical/experimental (dashed/dotted lines) results from Grilli et al. [57].

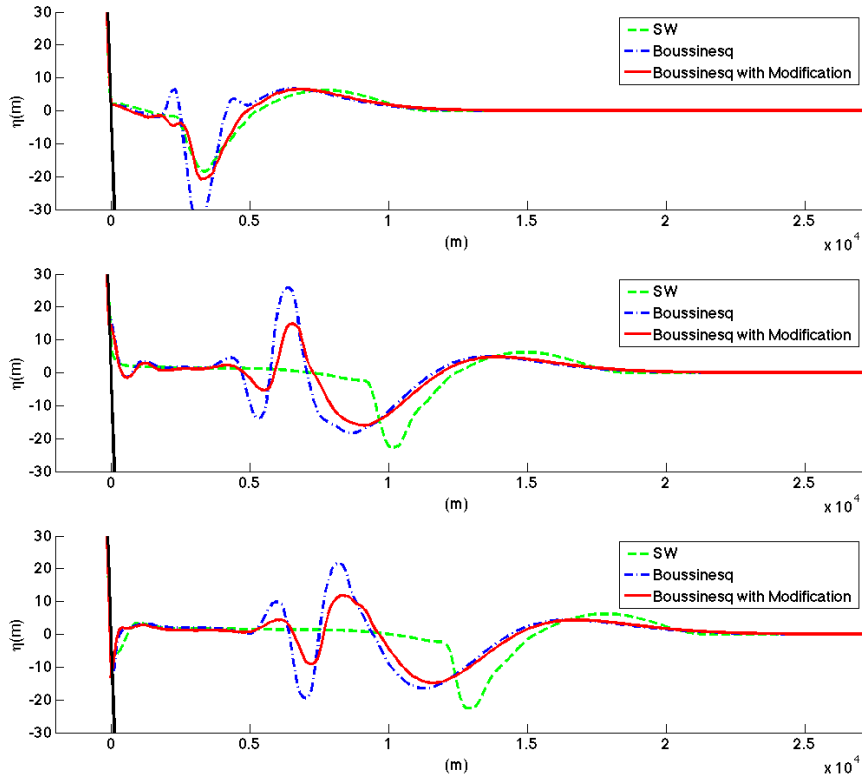

Figure 8.5: Numerical tests with Grilli et al [57]'s problem. SWE(dashed green), Scäffer and Madsen(dotted blue), and modified Scäffer and Madsen(solid red) (6.21) and (6.22) with $\Delta x = 100$ at t=97.4 s, t=168.8 s and 197.2 s from top to bottom.

8.3 Papua New Guinea 1998

8.3.1 Introduction

On July 17th 1998, magnitude 7.1 earthquake took place at the north coast of Papua New Guinea(PNG). A large tsunami was generated and killed approximately 2200 people as a result. Even though the source of the tsunami is still controversial, it is widely accepted that it was generated by the submarine landslide. One piece of supporting evidences is that there is a 10 minute difference between the field-measured arrival time and the fault-generated tsunami arrival time from numerical simulation. Secondly, it is believed that earthquakes of magnitude less than 8.0 do not generate large waves, and the earthquake of PNG was only

7.1 magnitude. For these reasons, many researchers conclude that the waves were mainly generated by submarine landslides.

8.3.2 Numerical Simulations of the PNG 1998 Tsunamis

Field surveys

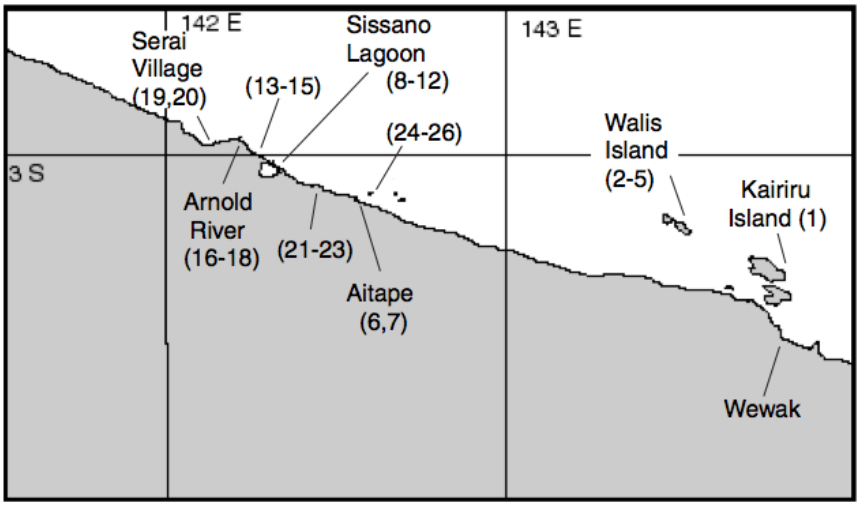

Figure 8.6: Survey locations by the International Tsunami Survey Team(ITST). Adopted from Synolakis et al. [92] Figure 1.

The first tsunami investigation was carried out by the International Tsunami Survey Team(ITST) from 31 July to 7 August, 1998. Kawata et al. [79] documented measured run-ups from the field survey team which was split into two groups to investigate tsunami inundation. One group surveyed Walis island and Kainriru island, while the other surveyed Sissano Lagoon area. In Figure 8.6, survey locations are displayed.

Figure 8.7 shows the maximum water height measured by ITST. Along the coastline, the survey of maximum run-up and inundation was measured from tsunami debris, but the same strategy could not be applied on the lagoon area. For details, see Kawata et al. [79] and Lynett et al. [92]. In Figure 8.7, we observe that worst damages were focused on the Sissano

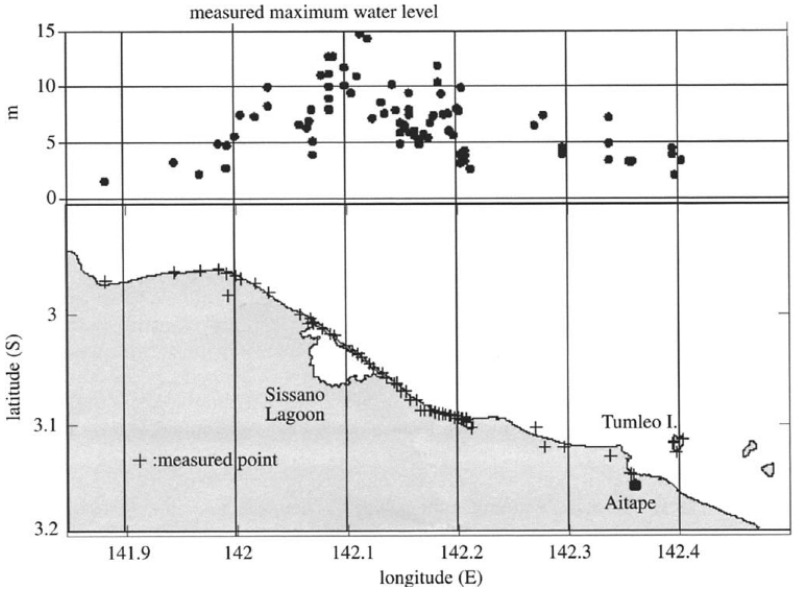

Figure 8.7: Maximum water heights measured by the International Tsunami Survey Team(ITST). The map at the bottom shows the location of the individual measurements (crosses). The diagram at the top plots the individual heights as a function of longitude along the coast. Adopted from Synolakis et al. [130] Figure 2.

Lagoon which is a narrow sand spit between the sea and the lagoon. Since this lagoon area was washed away and completely overtopped by tsunami waves, the measurements are based on debris such as a bucket on a tree.

Submarine landslide modeling

Many factors affect the deformation of landslides including location, depth, friction coefficients and initial shape. If there are data before and after submarine avalanches, the deformation can be found relatively easily. From initial and final deformation, we can estimate the friction coefficient. For example, Weiss et al. [142] used a viscous fluid model for Valdes slide, and concluded that the dynamic viscous coefficient is equal to 7.83×10^5 Pa·s.

In the PNG 1998 case, however, the exact topography before the landslide is unknown. Many researchers agreed on the location of submarine avalanches and suggested the volume

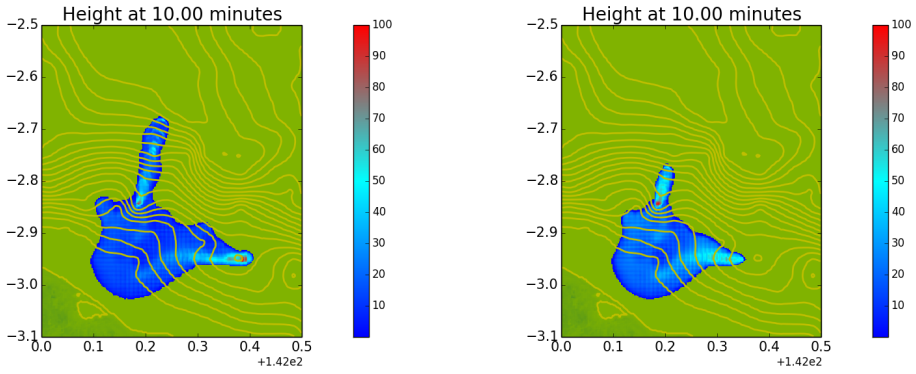

Figure 8.8: Deposition at $t = 10$ minutes with dynamic viscosity coefficient $\nu = 1 \times 10^4$ Pa·s (left) and $\nu = 2.5 \times 10^4$ Pa·s (right). The initial condition is the same as case 5 of Imamura et al. [74].

was between 3 km^3 and 9 km^3, but they have proposed different initial conditions with various height, diameter and friction coefficients. For example, Imamura et al. [74] suggested 5 possible cases with different diameter and relatively small height. Heinrich et al. [67] have chosen initial shape of landslides with large height , and applied viscous and granular friction models with several choices of coefficients. Lynett et al. [92] did not include the motion of the landslides directly, but modified initial water elevation which have been generated by submarine deformation.

When we use friction models for the submarine landslide, the choice of friction coefficient makes a difference in landslide deformation and generated waves' height. For example, Figure 8.8 shows the deposition at $t = 10$ minutes with two different viscous coefficients $\nu = 1 \times 10^4$ and $\nu = 2.5 \times 10^4$ Pa·s. The difference in the deformation affect the wave generations, and we will investigate the wave height and run-ups in the following section.

Modeling wave generation

In this section, we present numerical results with the reduced model. We compute the submarine landslide deformation up to $t = 600$ seconds, then use these results as a change

of bottom bathymetry that generates waves. We apply both shallow water equations and Boussinesq equations to compute the height of the generated waves.

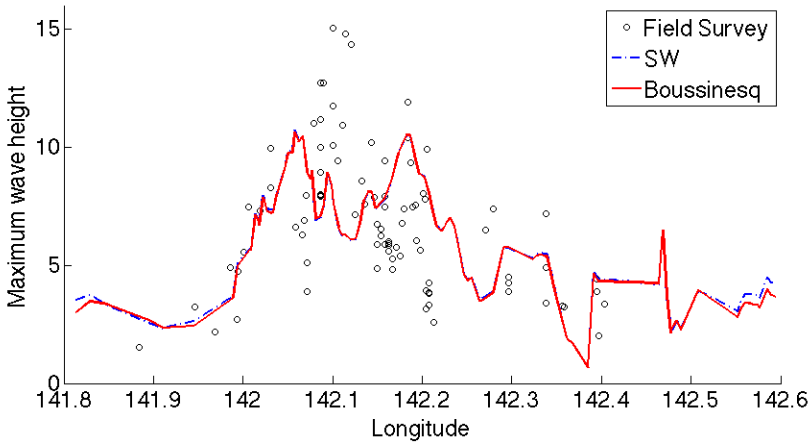

Figure 8.9: Maximum run-up with shallow water equations and Boussinesq equations. We use $\Delta x = 500$m grid with dynamic viscosity $\nu = 2.5 \times 10^4$, and initial condition is same as case 5 of Imamura et al. [74]. Numerical results from the shallow water equations and the Boussinesq equations are almost same except around 141.8 W and 142.6 W.

In order to validate our numerical model, we compare tsunami run-ups with field survey. To measure maximum run-ups in numerical simulation, we place 1600 gauges along the coastlines of longitude between 141.8 W and 142.6 W, then compute maximum height of waves on each longitude.

In Figure 8.11, we plot maximum run-ups with three different choices of viscosity. We observe that dynamic viscosity should be carefully chosen since the difference in run-ups can be relatively large. In the following numerical tests, we have chosen $\nu = 2.5 \times 10^4$ Pa·s for the dynamic viscous coefficient. Note that the same was found in [142].

Another factor that affects wave heights is the grid size of computational domain. In Figure 8.12, we observe that larger waves are generated for finer grids. When we compare numerical results with the field survey, we observe that numerical simulations have lower wave height around 142.1 W. Sissano lagoon is shown in Figure 8.7, where detailed

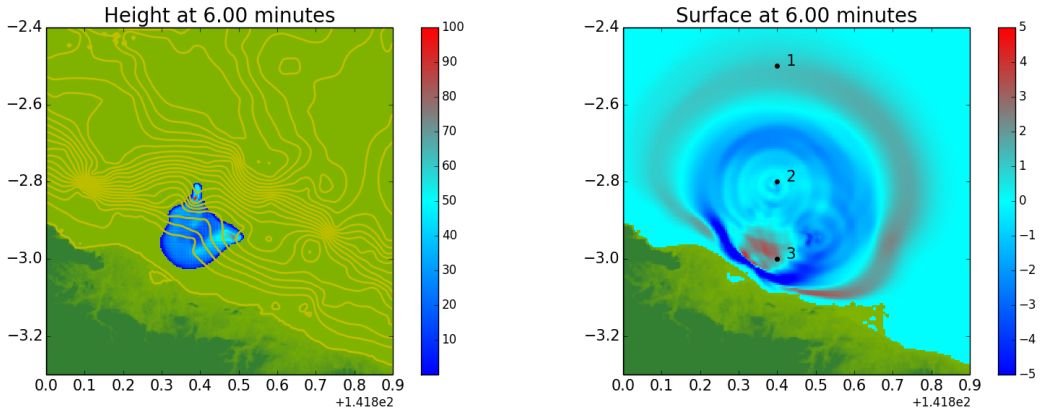

Figure 8.10: Snapshot of submarine landslide (left) and water surface elevation (right) at $t = 6$ minutes. We use $\Delta x = 500$m grid withynamic viscosity $\nu = 2.5 \times 10^4$, and the initial condition is the same as case 5 of Imamura et al. [74].

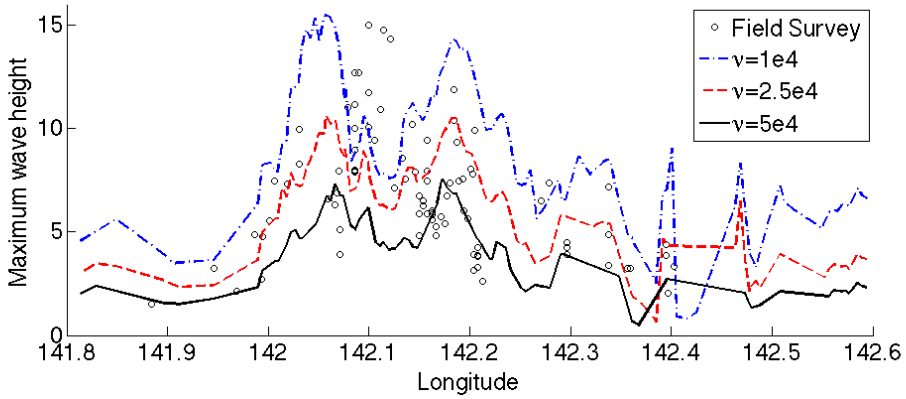

Figure 8.11: Maximum run-up with three dynamic viscous coefficients $\nu = 1 \times 10^4$, $\nu = 2.5 \times 10^4$ and $\nu = 5 \times 10^4$. Grid size is $\Delta x = \Delta y = 500$m. Initial condition is same as case 5 of Imamura et al. [74].

topography is necessary to compute run-ups accurately. For efficiency, we use adaptive mesh refinement with finest grid resolution $\Delta x = \Delta y = 50$ m at the lagoon area, and then maximum run-ups about 15 meters at 141.1 W is recovered.

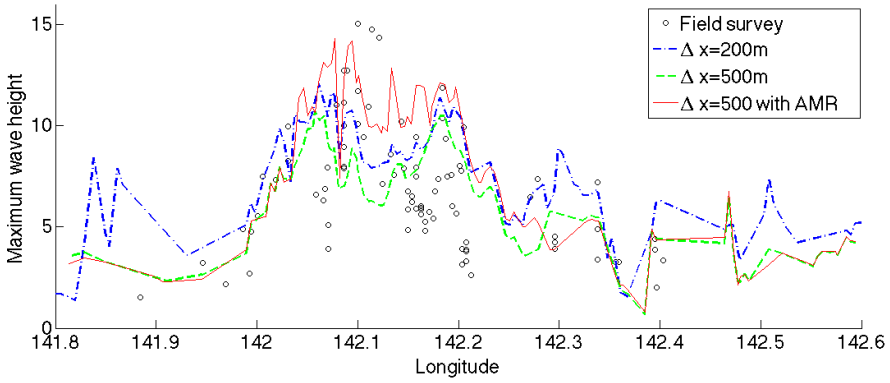

Figure 8.12: Maximum run-up with $\Delta x = \Delta y = 200$ m and $\Delta x = \Delta y = 500$ m. Adaptive mesh refinement is applied between 142.05 W and 142.2 W with finest grid $\Delta x = \Delta y = 50$ m. We apply shallow water equations with dynamic viscosity $\nu = 2.5 \times 10^4$ and initial condition is same as case 5 of Imamura et al. [74].

We apply both shallow water equations and Boussinesq equations in wave generation. In Figure 8.9, maximum run-ups are plotted from two sets of equations. Results from shallow water and Boussinesq equations are similar and only small discrepancy is observed. This can be explained in several ways. First, the distance from the center of submarine landslide to coast is not far enough for the dispersion to develop. Secondly, when the Boussinesq equations are used, there is a threshold of switching to the shallow water equations. The threshold is determined by the ratio of the wave amplitude and the bathymetry. If the ratio is larger than 0.8, then the wave breaking is expected and the shallow water equations are used instead. As large waves approach coastal area, the threshold is reached and the shallow water equations are used instead.

However, the difference between the shallow water equations and the Boussinesq equations becomes significant when the generated waves propagate toward the open ocean. In Figure 8.13, numerical results from the two sets of equations are shown. The locations of gauges can be found from Figure 8.13. The results are similar for gauges 2 and 3, but dispersion is clearly observed from gauge 1. Although wave patterns in gauge 1 are different, the largest wave amplitude and arrival time are similar between two equations.

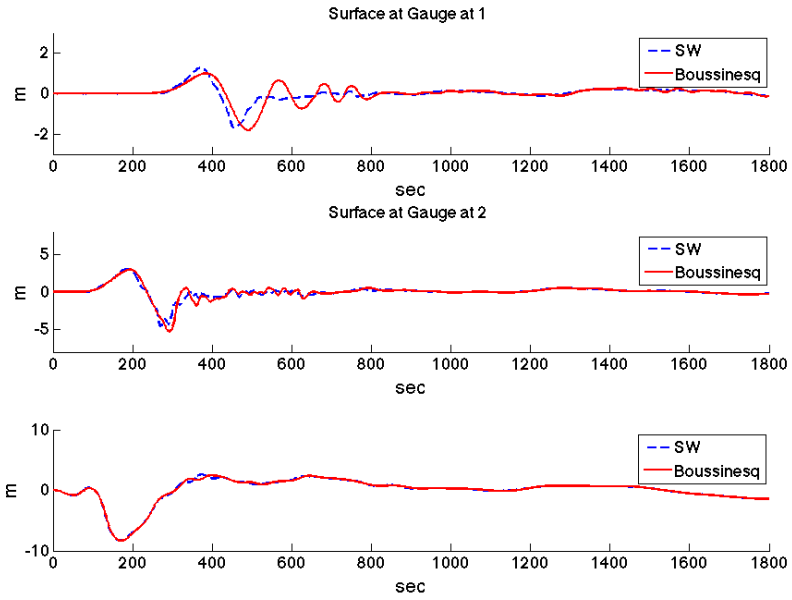

Figure 8.13: Gauge plots from the shallow water equations and Boussinesq equations, where the locations are shown in Figure 8.10.

8.4 Storegga Slide

8.4.1 Introduction

There is evidence that supports the existence of large submarine landslides at the edge of Norway's continental shelf. Bugge et al. [20] and Haflidason et al. [60] reported that one of the largest slides took place about 6,000-8,000 years ago, and the total volume was 2,400-3,200 km^3. This large slide is called as *Storegga slide* and this submarine landslide generated large tsunamis.

Tsunami deposits were discovered in Scotland and western Norway by Dawson et al. [31] and Bondevik et al. [16]. The highest deposits were found at above 20 meter from Shetland and 10-12 meter above sea level on the outer coast of western Norway. The generated tsunamis also reached Greenland, and Wagner et al. [137] found the tsunami deposits at the bottom of the Loon Lake which is located at 18 meter above sea level.

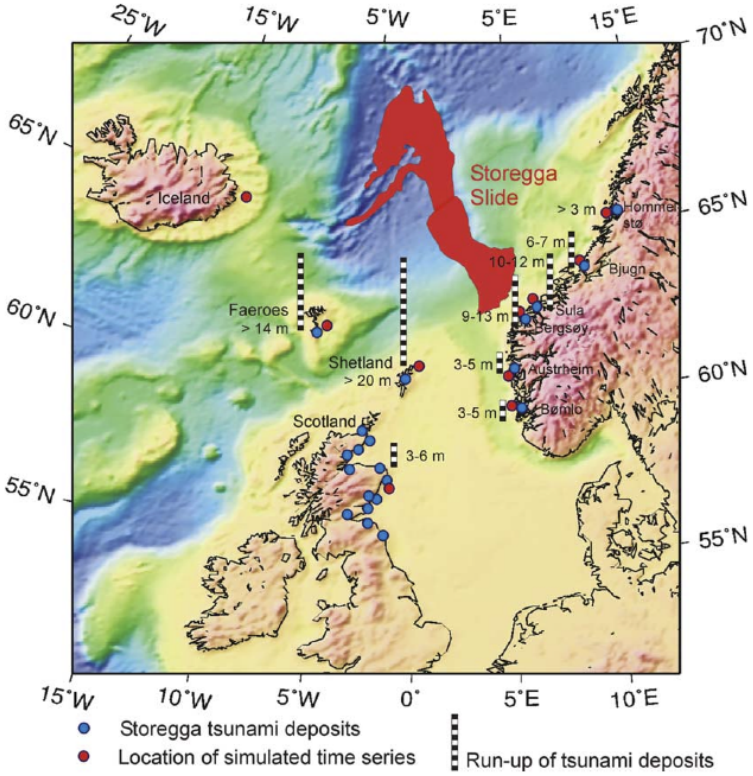

Figure 8.14: Map of the Storegga slide from Bondevik et al. [16]. Blue dots indicate where tsunami deposits have been found, and numbers show elevation of the deposits above the contemporary sea level.

Although the causes of this massive landslides are not obvious, possible ones are earthquake and natural gas field. Excessive pore pressure, induced by gas-hydrate dissociation due to sea-level/water-temperature change, is related to the occurrence of the landslides. On this unstable condition, large earthquakes may have triggered the Storegga landslides. We refer to Bryn et al. [19], Kvalstad et al. [82], Masson et al. [99] and Haflidason et al. [60] for more details.

8.4.2 Submarine landslide modeling

Previously, researchers used solid block motion to simulate submarine landslides. Harbitz [63] performed the numerical simulation of tsunami generation with one solid rigid body motion for the submarine landslides. Bondevik et al. [15] reconstructed the landslides with 167 blocks, and applied Haflidason et al. [60]'s *retrogressive* motion, so that each block slides with a time lag which varies from zero to 60 s. The initial acceleration is 0.016 m/s^2, and two cases were tested with the maximum speed equal to $u_{max} = 35$ m/s and $u_{max} = 20$ m/s. Bondevik et al. [15] performed numerical simulation in both coarse and fine grids, and concluded that fine grids are necessary for more accurate results.

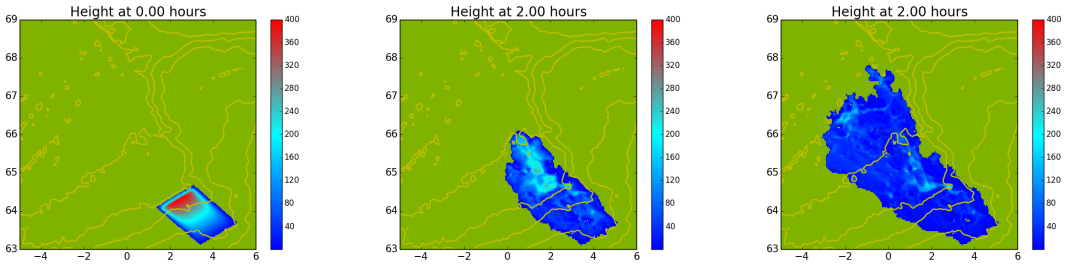

Figure 8.15: Initial shape (left) and deposition after $t = 2$ hours. Viscous coefficients are $\nu = 1 \times 10^4$ (left) and $\nu = 1 \times 10^3$ (right).

In this work, the viscous fluid model is applied for slide motion with the density of slide $\rho_s = 1,700\text{kg/m}^3$. The initial shape of slide is similar to Bondevik et al [15] whose volume is about $2,400$ km^3. Since the viscous fluid model is used, the maximum speed is not an appropriate indicator to distinguish different landslide cases, and we test with two choices of dynamic viscosity. In Figure 8.15, landslide deposition after 2 hours is shown for two cases with dynamic viscosity 1×10^4 and 1×10^3.

Modeling wave generation

In this section, we mainly use the shallow water equations for wave generation and propagation. When numerical results from the shallow water equations and Boussinesq equations,

are compared with uniform grid $\Delta x = \Delta y = 2'$, very small differences are observed. Especially when we compare the wave gauges at the indicated locations of Figure 8.14, the two results are nearly identical. Only a small discrepancy is noticed for the waves that are propagating north. The submarine landslide is 150 km $\times$ 100 km with 400 meter of maximum height, and the wave length of the generated waves is hundreds of kilometers, which is large compared to the depth of the ocean, and thus dispersion of waves is not observed.

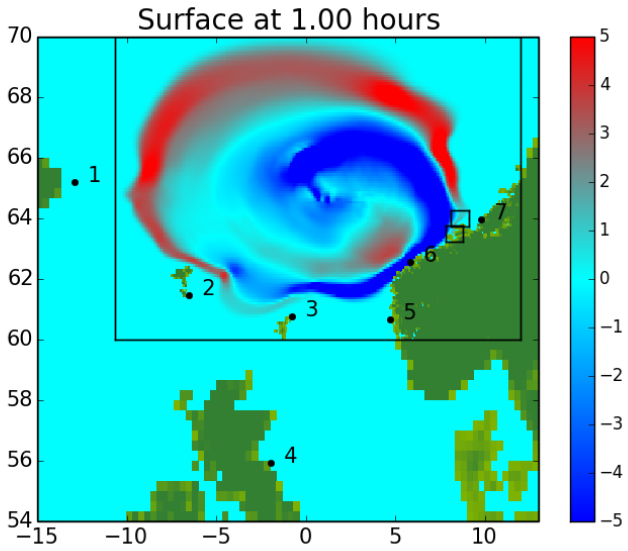

Figure 8.16: Snap shot of generated waves after 1 hour. Waves were generated by submarine landslide of viscosity 1×10^3 Pa·s.

We perform numerical tests with adaptive mesh refinement with smallest grid $\Delta x = \Delta y = 1' = 1/60°$. With viscous fluid model for landslide and *one-way coupled* scheme, we performed similar tests as Bondevik et al. [15]'s.

In Table 8.1, our numerical results are compared with field observation and Bondevik et al's results where the locations of gauges are the same as Bondevik et al [15]. The choice of viscosity makes a significant difference in surface elevation in all gauges. As Figure 8.17 shows, the pattern of waves are similar with different viscosity. Surface elevation from our numerical results is smaller than Bondevik et al's where rigid body motion is employed.

Site (Gauge #)	Observations(m)	Bondevik et al's	$\nu = 1 \times 10^3$	$\nu = 1 \times 10^4$
Bjugn(7)	6-8	14.3	7.7	3.6
Sula(6)	10-12	12.7	10.8	8.1
Austrheim(5)	3-5	6.6	2.7	1.5
Scotland(4)	3-6	5.9	3.0	1.4
Shetland island(3)	>12	8.0	5.8	4.7
Faeroe island(2)	>15-20	7.2	2.6	2.5
Iceland(1)	-	6.3	6.2	4.6

Table 8.1: Surface elevation from field observation and numerical simulations. Bondevik et al [15]'s data are the case with coarse grid and $u_{max} = 35$ m/s. For our numerical results, viscous model is employed for landslide motion with dynamic viscosity $\nu = 1 \times 10^3$ Pa·s and $\nu = 1 \times 10^4$ Pa·s ,and shallow water equations are used for waves.

Experiments from Watts [139] and Ataie-Ashtiani and Najafi-Jilani [7] support that waves generated by rigid body have larger amplitude than those generated by granular materials. Since the viscous fluid model is employed for our results, smaller wave amplitude is observed compared to Bondevik et al's.

We can observe the growth of wave amplitudes by the resonance arising from the complexity of the bathymetry. These phenomena can be detected more clearly if finer grids are used. For example, Shetland Islands have complex topography which is located at gauge 3 of Figure 8.16. In Figure 8.18, snapshots with two different grids are provided at the Shetland Islands. In the left figure, coarse grid is employed with $\Delta x \approx 5$ km and $\Delta y \approx 9$ km. For the right figure, AMR scheme is used with the finest grid size equal to $\Delta x \approx 0.25$ km and $\Delta y \approx 0.45$ km. In Figure 8.19, water surface elevations at each gauges are given with coarse and fine grids. Larger waves are observed with finer grids with resonance. At gauge 12 and 14, for instance, wave inundation is not observed with coarse grids, but wave amplitude larger than 10 meter is observed with fine grids.

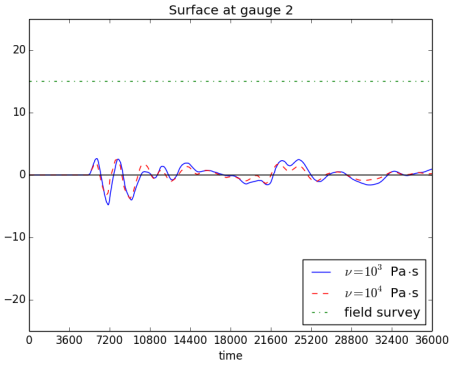

(a) Faeroe island

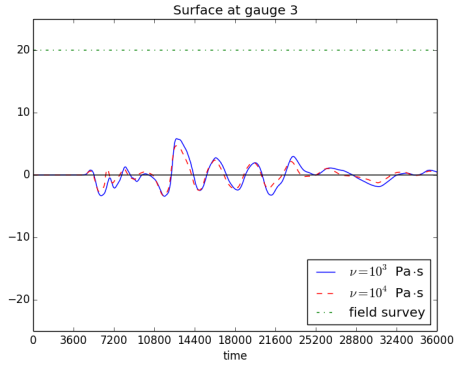

(b) Shetland island

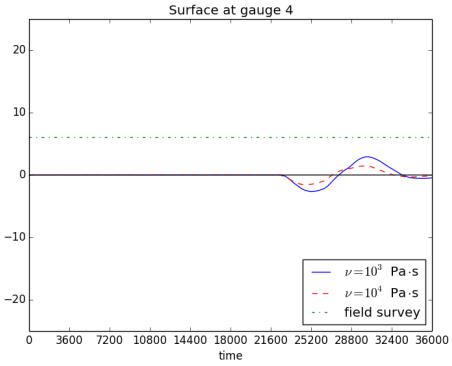

(c) Scotland

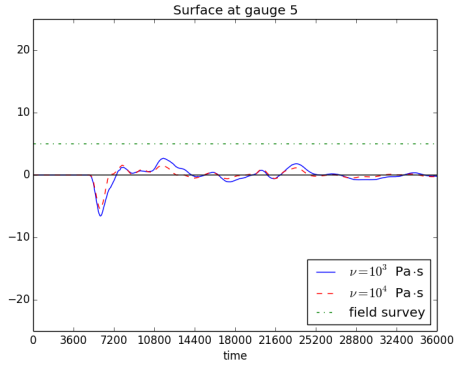

(d) Austrheim Norway

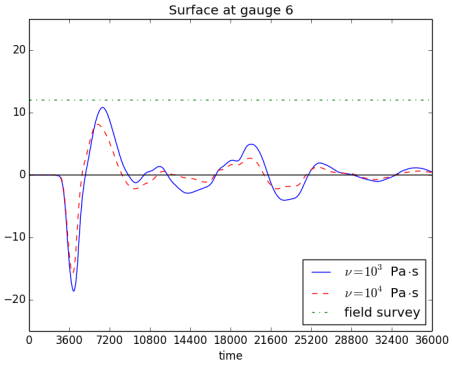

(e) Sula Norway

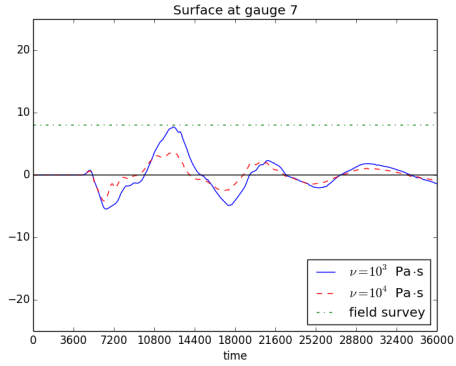

(f) Bjugn Norway

Figure 8.17: Gauge plots of numerical simulation of Storegga slide. Gauge locations are the same as Bondevik et al. [15]. Field survey is the observed run-up. Two cases for the viscosity is included with $\nu = 10^3$ Pa·s and $\nu = 10^4$ Pa·s.

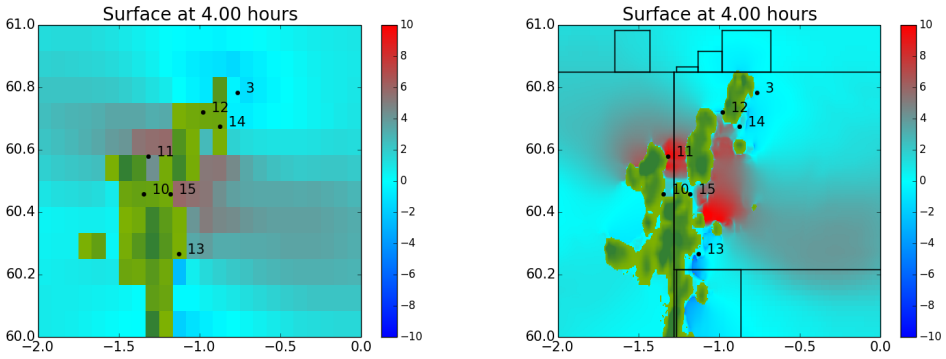

(a) Level 3

(b) AMR with Level 5

Figure 8.18: Snapshots of tsunami propagation at Shetland Islands with two different grids. For the left figure, the finest grid size is $\Delta x \approx 5$ km and $\Delta y \approx 9$ km. For the right figure, the finest grid size is $\Delta x \approx 0.25$ km and $\Delta y \approx 0.45$ km.

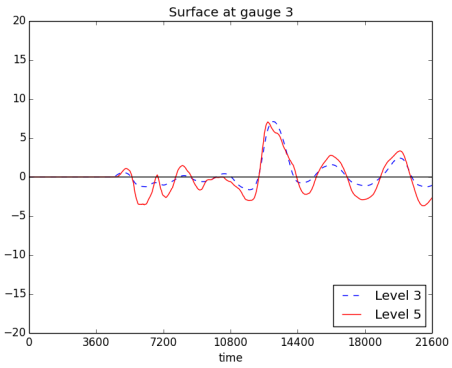

(a) Gauge 3

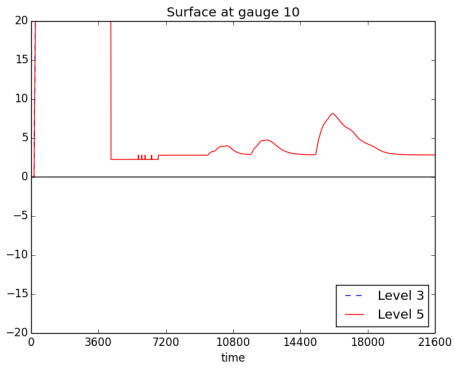

(b) Gauge 10

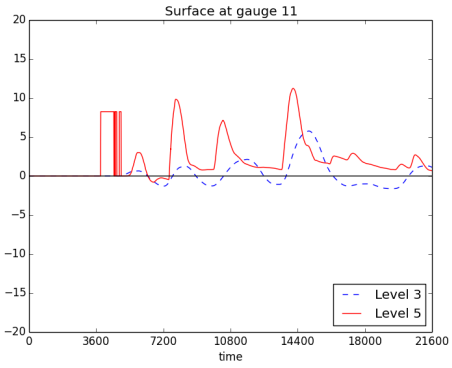

(c) Gauge 11

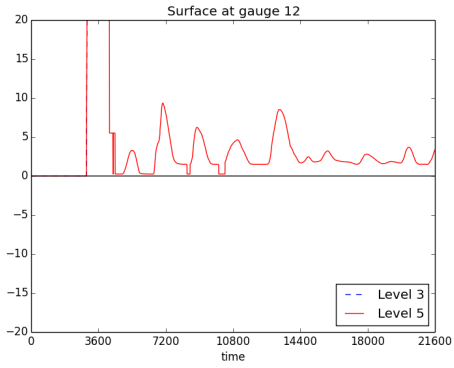

(d) Gauge 12

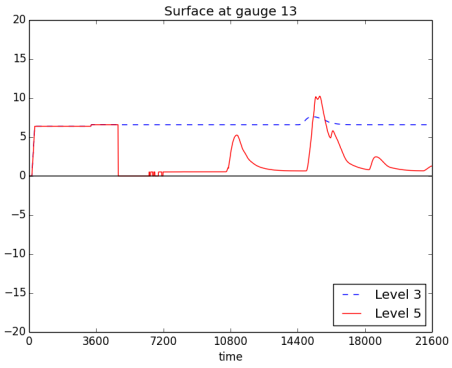

(e) Gauge 13

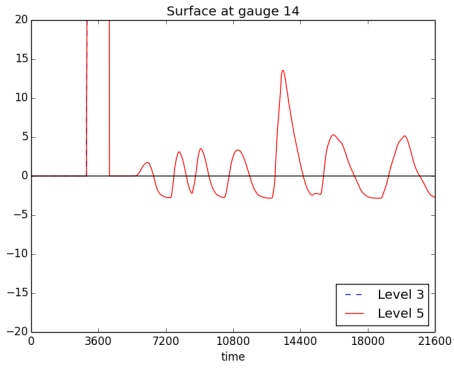

(f) Gauge 14

Figure 8.19: Gauge plots at the Shetland Islands with coarse and fine grids. The location is indicated in Figure 8.18.

Chapter 9

CONCLUSIONS AND FUTURE DIRECTIONS

In this chapter, a brief summary will be given and possible future directions will be addressed.

9.1 Conclusions

The main contribution of this thesis is the development and analysis of numerical schemes for modeling the surface waves generated by submarine landslides. The multi-layer shallow water equations were derived, and properties of the system were investigated with approximate Riemann solvers that can solve the dry state problems properly. The Riemann solver was constructed with *f-wave* propagation method to preserve steady states. A *one-way coupled* scheme was suggested that is applicable to the tsunamis generated by submarine landslides. The *one-way coupled* scheme was compared with the *fully coupled* scheme through numerical simulations in Chapter 7. If the distance from the landslide layer to the water surface is large and the density difference between the two layers is large, then small differences were observed between the two numerical approaches. Since most of the submarine landslides occur at the edge of continental shelves or deeper ocean, and the density of landslide is $2,600$ kg/m^3 while the density of water is $1,000$ kg/m^3, the one-way coupled scheme is recommended because it can solve the problem more efficiently.

The landslide deformation was modeled in the shallow flow regime with a uniform density. Chapter 5 reviewed several numerical models for landslides, and compared the viscous fluid model and the Coulomb friction model with numerical simulations. The landslide deformation was highly affected by the choice of the friction models, and also influenced by the parameter in each friction model so that it is generally very difficult to achieve good agreements with observations. Between the two models, the Coulomb friction model was more sensitive to the choice of the friction parameter.

Waves generated by submarine landslides often have shorter wavelength than the earthquakes generated tsunamis, and it is desirable to incorporate the dispersion of waves. A class of depth averaged equations was investigated in Chapter 6 that is called the Boussinesq-type equations. Different forms of the Boussinesq equations were reviewed, and Schäffer and Madsen's model [124] was adopted because their model is derived in conservation form and includes the dispersion terms in the momentum equations only, but still the dispersion relation is well-satisfied for the waves of short wavelength. The numerical implementation is relatively easy and it is cheaper computationally than the other candidates. Following Lynett and Liu's work, Schäffer and Madsen's model was modified to include the change of bathymetry.

Numerical schemes for this Boussinesq equations were developed as a hybrid of high resolution finite volume and finite difference methods. The Boussinesq equations were rearranged into the shallow water equations and the dispersive terms, and the shallow water equations are solved with the finite volume method while dispersive terms are computed with the finite difference method. For the spatial discretization, a second order centered scheme is used, and a fourth order Runge-Kutta scheme is used for the time stepping. Stability and convergence of the hybrid scheme was studied using the KdV-BBM equations and the Serre's equations as model problems. In two space dimensions, the solver was also combined with adaptive mesh refinement to solve the global scale problems efficiently.

Numerical schemes were validated through comparison with laboratory experiments and field studies of historical events. Both the shallow water equations and the Boussinesq equations were tested and the results were given in Chapter 7. In NTHMP Benchmark problem 5, numerical simulations with the Boussinesq equations is in a good agreement with the laboratory results which was not possible with the shallow water equations. The Coulomb friction model was used for comparison to Watts' experiments, but our model did not produce the landslide deformation correctly, and there is clear discrepancy between the numerical and laboratory results. With the Boussinesq solver, however, an improvement is observed in the far-field wave gauge where the dispersion of waves developed.

in Chapter 8, we also performed numerical tests for large-scale problems such as the Papua New Guinea 1998 and the Storegga slide. Our method was developed with adaptive

mesh refinement (AMR) and incorporated into GEOCLAW. AMR is an efficient way to handle the complex bathymetry at the lagoon area of Papua New Guinea and the Shetland islands of the Storegga slide, and the global scale wave propagation at the same time.

If the waves are generated by submarine landslides at the edge of the continental shelves, the numerical results from the shallow water equations and the Boussinesq equations are very similar in the case of the waves approaching to the nearby coastline. When the waves propagating toward the open ocean are compared, the numerical results are significantly different. In the Papua New Guinea case, the most damaged area was Sissano lagoon which was closest from the source of the submarine landslide, and the shallow water equations produced almost identical results to the Boussinesq equations.

It is most likely that large-scale submarine landslides occur at the edge of the continental shelf, and large waves will be hitting the nearby shore. Therefore, the shallow water equations with adaptive mesh refinement should be the first choice. If the area of interest is further from the site of submarine landslides, then the Boussinesque solver may be worth using.

9.2 Future Directions

One possible future direction for this work is improving the landslide modeling. As indicated in this thesis, the computed landslide deformation can be significantly different depending on the choices of the friction models and parameters. Adopting a well-established numerical model can be a solution to this problem, and one option is to use the DCLAW software currently being developed at the Cascades Volcano Observatory. Although it is desirable to develop more reliable computational models for submarine landslides, the exact values of the parameters for the landslide materials cannot be pre-determined in general. It is also hard to predict the location or total mass of future landslides. In order to assess the hazards due to submarine landslides and the generated waves, probabilistic approaches may need to be adopted.

Landslides plunging into the water can also generate large waves, and the *one-way coupled* model cannot be applied, because the reaction from the water to the landslide cannot be ignored and needs to be considered carefully. In those situations, the fully coupled models

would be more suitable, but efficient schemes for the fully coupled schemes still require more study. Furthermore, the depth-averaged models may not be appropriate to use and full 3-dimensional models may be required instead.

There are several possible directions in further development of the Boussinesq type solvers. A finite difference scheme with fourth order Runge-Kutta time stepping has been used in this thesis, but other higher order accurate schemes such as spectral methods can be used instead. The spectral method will require generating another set of grids and interpolation. The other direction is to choose higher order equations. In this work, we have chosen the Schäffer and Madsen model, which is often called a *second order* Boussinesq-type equation. There are higher order set of equations. For example, see Lynett and Liu [91], Fuhrman and Madsen [94] and Zhou and Tang [144]. Their models are more complicated and also require the update of the mass equation in the dispersion term computation.

BIBLIOGRAPHY

[1] R. Abgrall and S. Karni. Two-layer shallow water system: A relaxation approach. *SIAM J. Sci. Comput.*, 31(3):1603–1627, 2009.

[2] P. R. Amestoy, I. S. Duff, J. L'Excellent, and J. Koster. *MUMPS: a general purpose distributed memory sparse solver*, pages 121–130 Springer, 2001.

[3] C. Ancey. Plasticity and geophysical flows: A review. *Journal of non-Newtonian fluid mechanics.*, 142(1), 2007.

[4] M. E. M. Arcos and R. J. LeVeque. Validating velocities in the GEOCLAW tsunami model using observations near Hawaii from the 2011 Tohoku tsunami. *submitted*, 2013.

[5] A. Argnani, S. Tinti, F. Zaniboni, G. Pagnoni, A. Armigliato, D. Panetta, and R. Tonini. The eastern slope of the southern Adriatic basin: a case study of submarine landslide characterization and tsunamigenic potential assessment. *Marine Geophysical Researches*, 32(1-2):1–2, 2011.

[6] S. Assier-Rzadkiewicz, P. Heinrich, P. C. Sabatier, B. Savoye, and J. F. Bourillet. Numerical modelling of a landslide-generated tsunami: The 1979 Nice event. *Pure and Applied Geophysics*, 157:1707–1728, 2000.

[7] B. Ataie-Ashtiani and A. Najafi-Jilani. Laboratory investigations on impulsive waves caused by underwater landslide. *Coast. Eng. Coastal Engineering*, 55(12):989–1004, 2008.

[8] B. AtaieAshtiani and A. Najafi-Jilani. A higher order Boussinesq type model with moving bottom boundary: applications to submarine landslide tsunami waves. *International Journal for Numerical Methods in Fluids*, 53(6):1019–1048

[9] E. Audusse. A multilayer Saint-Venant model. *Discrete and Continuous Dynamical Systems, Series B*, 5(2):189–214, 2005.

[10] D. Bale, R. J. LeVeque, S. Mitran, and J. A. Rossmanith. A wave-propagation method for conservation laws and balance laws with spatially varying flux functions. *SIAM J. Sci. Comput.*, 24:955–978, 2002.

[11] S. A. Beisel, L. B. Chubarov, Z. I. Fedotova, and G. S. Khakimzyanov. On the approaches to a numerical modeling of landslide mechanism of tsunami wave generation. *Communications in Applied Analysis*, 11(1):121–135, 2007.

[12] M. J Berger and P. Colella. Local adaptive mesh refinement for shock hydrodynamics. *Journal of computational Physics*, 82(1):64–84 1989.

[13] M. J. Berger, D. L. George, R. J. LeVeque, and K. T. Mandli. The GEOCLAW software for depth-averaged flows with adaptive refinement. *Advances in Water Resources*, 34(9):1195–1206 2011.

[14] M. J Berger and J. Oliger. Adaptive mesh refinement for hyperbolic partial differential equations. *Journal of computational Physics*, 53(3):484–512 1984.

[15] S. Bondevik, F. Løvholt, C. Harbitz, J. Mangerud, A. G Dawson, and J. Inge Svendsen. The Storegga slide tsunami - comparing field observations with numerical simulations. *Marine and Petroleum Geology*, 22(1–2):195–208, 2005.

[16] S. Bondevik, J. I. Svendsen, G. Johnsen, J. Mangerud, and P. E. Kaland. The Storegga tsunami along the Norwegian coast, its age and runup. *BOREAS*, 26(1):29–54, 1997.

[17] P. Bonneton, F. Chazel, D. Lannes, F. Marche, and M. Tissier. A splitting approach for the fully nonlinear and weakly dispersive Green-Naghdi model. *Journal of Computational Physics*, 230(4):1479–1498 0021–9991, 2011.

[18] F. Bouchut and V. Zeitlin. A robust well-balanced scheme for multi-layer shallow water equations. *Discrete and Continuous Dynamical Systems*, 13(4):739–758, 2010.

[19] P. Bryn, K. Berg, C. F. Forsberg, A. Solheim, and T. J. Kvalstad. Explaining the Storegga slide. *Marine and Petroleum Geology*, 22(1-2):11–19, 2005.

[20] T Bugge, RH Belderson, and NH Kenyon. The Storegga slide. *Philosophical Transactions of the Royal Society of London. Series A, Mathematical and Physical Sciences*, pages 357–388 1988.

[21] M. Castro, J.T. Frings, S. Noeele, C. Pasre, and G. Puppo. On the hyperbolicity of two- and three-layer shallow water equations.

[22] M. J. Castro, J. A. Garcia-Rodriguez, J. M. Gonzalez-Vida, J. Macias, and C. Pares. Improved FVM for two-layer shallow-water models: Application to the Strait of Gibraltar. *Advances in Engineering Software*, 38(6):386–398, 2007.

[23] M. J. Castro, J. M. González-Vida, and C. Parés. Numerical treatment of wet/dry fronts in shallow flows with a modified Roe scheme. *Mathematical Models and Methods in Applied Sciences*, 16(06):897–931, 2006.

[24] M.J. Castro, P.G. LeFloch, M.L. Munoz-Ruiz, and C. Pares. Why many theories of shock waves are necessary: Convergence error in formally path-consistent schemes. *J. Computational Physics*, 227(17):8107, 2008.

[25] M.J. Castro, J. Macias, and C. Pares. A Q-scheme for a class of systems of coupled connservation laws with source. application to a two-layer 1-d shallow water system terms. *M2AN Math. Model. Numer. Anal.*, 35:107–127, 2001.

[26] S. Chen and S. Peng. Two-dimensional numerical model of two-layer shallow water equations for confluence simulation. *Advances in Water Resources*, 29:1608–1617, 2006.

[27] S. Chen, S. Peng, and H. Capart. Two-layer shallow water computation of mud flow intrusions into quiescent water. *Journal of Hydraulic Research*, 45(1):13–25, 2007.

[28] L. Chumakova, F. E. Menzaque, P. A. Milewski, R. R. Rosales, E. G. Tabak, and C. V. Turner. Shear instability for stratified hydrostatic flows. *Communications on Pure and Applied Mathematics*, 62(2):183–197, 2009.

[29] D. M Cruden and D. J Varnes. Landslide types and processes. *Landslides: investigation and mitigation*, 247:36–75, 1996.

[30] Peter A Cundall. *Formulation of a three-dimensional distinct element model—Part I. A scheme to detect and represent contacts in a system composed of many polyhedral blocks*, volume 25. Elsevier, 1988.

[31] A. G Dawson, D Long, and D. E Smith. The Storegga slides: Evidence from eastern Scotland for a possible tsunami. *Marine Geology*, 82(3–4):271–276, 8 1988.

[32] F. V. De Blasio. Hydroplaning and submarine debris flows. *J. Geophys. Res. Journal of Geophysical Research*, 109(C1), 2004.

[33] R. P. Denlinger and R. M. Iverson. Granular avalanches across irregular three-dimensional terrain: 1. theory and computation (doi 10.1029/2003jf000085). *Journal of geophysical research.*, 109, 2004.

[34] R. P. Denlinger and R. M. Iverson. Granular avalanches across irregular three-dimensional terrain: 2. Experimental tests. *J. Geophys. Res.*, 109:F01015, 2004.

[35] V. Dolejší and T. Gallouët. A numerical study of a particular non-conservative hyperbolic problem. *Computers & Fluids*, 37(9), 2008.

[36] D. Dutykh, Th Katsaounis, and D. Mitsotakis. Finite volume methods for unidirectional dispersive wave models. *International Journal for Numerical Methods in Fluids 1097-0363*, 2012.

[37] B. Einfeldt. On Godunov-type methods for gas dynamics. *SIAM J. on Num. Anal.*, 25(2):294–318, 04 1988.

[38] F. Enet and S. T Grilli. Experimental study of tsunami generation by three-dimensional rigid underwater landslides. *Journal of Waterway, Port, Coastal, and Ocean Engineering*, 133(6):442–454

[39] L.C. Evans. *Partial Differential Equations*. American Mathematical Society, 2010.

[40] E. D. Fernandez-Nieto, F. Bouchut, D. Bresch, M. J. Castro Diaz, and A. Mangeney. A new Savage-Hutter type model for submarine avalanches and generated tsunami. *Journal of Computational Physics*, 227(16):7720–7754, 2008.

[41] I. V. Fine, A. B. Rabinovich, R. E. Thomson, and E. A. Kulikov. Numerical modeling of tsunami generation by submarine and subaerial landslides. *Submarine Landslides and Tsunamis*, 1, 2003.

[42] W. D. L. Finn. *Landslide-generated tsunamis: geotechnical considerations*, pages 1879–1894 Springer, 2003.

[43] U. Fjordholm, S. Mishra, and E. Tadmor. Energy preserving and energy stable schemes for the shallow water equations. *London Mathematical Society Lecture Note Series*, (363):93–139, 2009.

[44] J. G. Fleming, R. A. Walters, L. P. Sue, and R. I. Nokes. Experimental design for solid block and granular submarine landslides: a unified approach. *Advances in Natural and Technological Hazards Research*, 23:259–278, 2005.

[45] F. G. Friedlander. *Introduction to the theory of distributions*. Cambridge University Press, Cambridge [Cambridgeshire]; New York, 1982.

[46] H. M. Fritz, F. Mohammed, and J. Yoo. Lituya bay landslide impact generated mega-tsunami 50th anniversary. *Pure Appl. Geophys. Pure and Applied Geophysics*, 166(1-2):153–175, 2009.

[47] E. L. Geist. Origin of the 17 July 1998 Papua New Guinea tsunami: Earthquake or landslide? *Seismological Research Letters*, 71:344–351, 2000.

[48] D. L. George. Finite volume methods and adaptive refinement for tsunami propagation and inundation. *Ph.D. Thesis, University of Washington*, 2006.

[49] D. L. George. Augmented Riemann solvers for the shallow water equations over variable topography with steady states and inundation. *J. of Com. Phys.*, 227(6), 2008.

[50] D. L. George and R. M. Iverson. A two-phase debris-flow model that includes coupled evolution of volume fractions, granular dilatancy, and pore-fluid pressure. In R. Genevois, D. Hamilton, and A. Prestininzi, editors, *The 5th intl. conf. on debris-flow hazards*, pages 415–424, Padova, Italy, June 2011. Italian Journal of Engineering, Geology and Environment.

[51] M Gobbi and J Kirby. Wave evolution over submerged sills: tests of a high-order Boussinesq model. *Coastal Engineering*, 1999.

[52] F I González, R J LeVeque, P Chamberlain, B Hirai, J Varkovitzky, and D L George. Geoclaw model. In *Proceedings and Results of the 2011 NTHMP Model Benchmarking Workshop*, pages 135–211. National Tsunami Hazard Mitigation Program, NOAA, 2012.

[53] F. I. Gonzalez, B. L. Sherrod, B. F. Atwater, A. P. Frankel, S. P. Palmer, M. L. Holmes, R. E. Karlin, B. E. Jaffe, V. V. Titov, H. O. Mofjeld, and A. J. Venturato. Puget Sound tsunami sources - 2002 workshop report. 2003.

[54] J.M.N.T. Gray, M. Wieland, and K. Hutter. Gravity driven free surface flow of granular avalanches over complex basal topography. *Proc. R. Soc. London A*, (455):1841–1874, 1999.

[55] AE Green and PM Naghdi. A derivation of equations for wave propagation in water of variable depth. *Journal of Fluid Mechanics*, 78(02):237–246 1976.

[56] S. T. Grilli, J. C. Harris, D. Tappin, R. J. Geller, T. Masterlark, J. T. Kirby, F. Shi, and G. Ma. A submarine landslide is required to explain the 2011 1 Tohoku tsunami. *in preparation.*

[57] S. T. Grilli, S. Vogelmann, and P. Watts. Development of a 3d numerical wave tank for modeling tsunami generation by underwater landslides. *Engineering Analysis with Boundary Elements*, 26(4):301–313 0955–7997, 2002.

[58] S. T. Grilli and P. Watts. Modeling of waves generated by a moving submerged body. applications to underwater landslides. *Engineering Analysis with boundary elements*, 23(8):645–656 0955–7997, 1999.

[59] S. T. Grilli and P. Watts. Tsunami generation by submarine mass failure. i: Modeling, experimental validation, and sensitivity analyses. *Journal of Waterway, Port, Coastal, and Ocean Engineering*, 131(6):283–297, 2005.

[60] H. Haflidason, H. P. Sejrup, A. Nygard, J. Mienert, P. Bryn, R. Lien, Carl F. Forsberg, K. Berg, and D. G. Masson. The Storegga slide: architecture, geometry and slide development. *Marine geology.*, 213(1), 2004.

[61] M. A. Hallworth and H. E. Hupert. Abrupt transition in high-concentration, particle-driven gravity currents. *Physics of Fluids*, 10(5), 1998.

[62] M. A Hampton, Homa J. Lee, and J. Locat. Submarine landslides. *Reviews of geophysics*, 34(1):33–59

[63] C. B. Harbitz. Model simulations of tsunamis generated by the Storegga slides. *Marine geology.*, 105(1-4):1–22, 1992.

[64] C.B. Harbitz, F. Lovholt, G. Pedersen, and D.G. Masson. Mechnisms of tsunami generation by submarine landslide: a short review. *Norwegian Journal of Geology*, 86:255–264, 2006.

[65] A. Harten. High resolution schemes for hyperbolic conservation laws. *Journal of computational physics*, 49(3):357–393 1983.

[66] A. Harten, P. D. Lax, and B. V. Leer. On upstream differencing and godunov-type schemes for hyperbolic conservation laws. *SIAM Review*, 25(1):35–61, 01 1983.

[67] Ph. Heinrich, A. Piatanesi, and H. Hebert. Numerical modelling of tsunami generation and propagation from submarine slumps: the 1998 Papua New Guinea event. *Geophys. J. Int.*, 145:97–111, 2001.

[68] J. Horrillo, Z. Kowalik, and Y. Shigihara. Wave dispersion study in the Indian Ocean-tsunami of December 26, 2004. *Marine Geodesy*, 29(3):149–166, 2006.

[69] X. Huang, A. Garcia, and H. Marcelo. A Herschel–Bulkley model for mud flow down a slope. *Journal of Fluid Mechanics*, 374:305–333, 1998.

[70] O. Hungr, S. G. Evans, M. J. Bovis, and J. N. Hutchinson. A review of the classification of landslides of the flow type. *Environmental & Engineering Geoscience*, 7(3):221–238, 2001.

[71] E. H. Huppert. Gravity currents: A personal perspective. *Journal of Fluid Mechanics*, 554(1):299–322, 2006.

[72] J. N. Hutchinson. *General report: morphological and geotechnical parameters of landslides in relation to geology and hydrogeology: Proc 5th International Symposium on Landslides, Lausanne, 10–15 July 1988V1, P3–35. Publ Rotterdam: AA Balkema, 1988*, volume 26. Pergamon, 1989.

[73] K. Hutter, Y. Wang, and S. P. Pudasaini. The Savage-Hutter avalanche model: How far can it be pushed? *Philosophical Transactions: Mathematical, Physical and Engineering Sciences*, 363(1832):1507–1528, 07 2005.

[74] F. Imamura and K. Hashi. Re-examination of the source mechanism of the 1998 Papua New Guinea earthquake and tsunami. *Pure and Applied Geophysics*, 160:2071–2086, 2003.

[75] R. M. Iverson. The physic of debris flows. *Rev Geophys*, 35:245–296, 1997.

[76] R. M Iverson, M. Logan, and R. P Denlinger. Granular avalanches across irregular three-dimensional terrain: 2. experimental tests. *Journal of Geophysical Research: Earth Surface (2003–2012)*, 109(F1), 2004.

[77] C. D. Jan and H. W. Shen. Review dynamic modeling of debris flows. *Lecture notes in earth sciences.*, (64), 1997.

[78] L. Jiang and P.H. LeBlond. The coupling of a submarine slide and the surface waves which it generates. *Journal of Geophysical Research*, 97(C8):12731–12744, August 1992.

[79] Y. Kawata, B. C. Benson, J. C. Borrero, J. L. Borrero, H. L. Davies, W. P. Lange, F. Imamura, H. Letz, J. Nott, and C. E. Synolakis. Tsunami in Papua New Guinea was as intense as first thought. *Eos, Transactions American Geophysical Union*, 80(9):101–105 2324–9250, 1999.

[80] T. Koch, R. Greve, and K. Hutter. Unconfined flow of granular avalanches along a partly curved chute. II. experiments and numerical computations. *Proc. R. Soc. London A*, 445:415–435, 1994.

[81] P. K. Kundu and I. M. Cohen. Fluid mechanics, 1990.

[82] T. J. Kvalstad, L. Andresen, C. F. Forsberg, K. Berg, P. Bryn, and M. Wangen. The Storegga slide: evaluation of triggering sources and slide mechanics. *Marine and petroleum geology.*, 22(1-2):245–256, 2005.

[83] P.A. Milewski R.R. Rosales E.G. Tabak L. Chumakova, F.E. Menzaque and C.V. Turner. Stability properties and nonlinear mappings of two and three-layer stratified flows. 2007.

[84] P. D. Lax. *Hyperbolic partial differential equations.* Courant Institute of Mathematical Sciences ; American Mathematical Society, New York; Providence, R.I., 2006.

[85] L. Lee and R. J. LeVeque. An immersed interface method for incompressible navier-stokes equations. *SIAM J. Sci. Comput.*, 25(3), 2004.

[86] R. J. LeVeque, D. L. George, and M. J. Berger. Tsunami modelling with adaptively refined finite volume methods. *Acta Numerica*, 20(1):211–289, 2011.

[87] R. J. J. LeVeque. *Finite volume methods for hyperbolic problems.* Cambridge University Press, Cambridge; New York, 2002.

[88] R. Liska and B. Wendroff. Analysis and computation with multi-layer fluid. 1996.

[89] ZB Liu and ZC Sun. Two sets of higher-order Boussinesq-type equations for water waves. *Ocean engineering*, 32(11):1296–1310

[90] P. Lynett and P. L. F. Liu. A numerical study of submarine landslide generated waves and run-up. *Proceedings of the Royal Society of London. Series A: Mathematical, Physical and Engineering Sciences*, 458(2028):2885–2910 1364–5021, 2002.

[91] P. Lynett and P. L. F. Liu. A two-layer approach to wave modelling. *Proceedings: Mathematical, Physical and Engineering Sciences*, 460(2049):2637–2669, 2004.

[92] P. J. Lynett, J. C. Borrero, Philip L-F Liu, and C. E. Synolakis. *Field survey and numerical simulations: A review of the 1998 Papua New Guinea tsunami*, pages 2119–2146 Springer, 2003.

[93] B. T. MacInnes, A. R. Gusman, R. J. LeVeque, and Y. Tanioka. Comparison of earthquake source models for the 2011 tohoku event using tsunami simulations and nearfield observations. *Bulletin of the Seismological Society of America*, 103(2B):1256–1274

[94] D R Fuhrmanand P A Madsen. Tsunami generation, propagation, and run-up with a high-order Boussinesq model. *Coastal Engineering*, 56(7):747–758

[95] H. A. Madsen, P. A.and Schäffer. Higher order Boussinesq-type equations for surface gravity waves: derivation and analysis. *Philosophical Transactions of the Royal Society of London. Series A: Mathematical, Physical and Engineering Sciences*, 356(1749):3123–3181

[96] P. A. Madsen and O. R. Sørensen. A new form of the Boussinesq equations with improved linear dispersion characteristics. part 2. a slowly-varying bathymetry. *Coastal Engineering*, 18(3-4):183–204, 1992.

[97] K. T. Mandli. Finite volume methods for the multilayer shallow water equations with applications to storm surges, Ph. D. thesis, University of Washington, 2011.

[98] G. Dal Maso, P.G. LeFloch, and F. Murat. Definition and weak stability of nonconservative products. *J. Math. Pures Appl.*, 74:483–548, 1995.

[99] D. G. Masson, C. B. Harbitz, R. B. Wynn, G. Pedersen, and F. Lovholt. Submarine landslides: processes, triggers and hazard prediction. *Philosophical Transactions of the Royal Society A: Mathematical, Physical and Engineering Sciences*, 364(1845):2009–2039, 2006.

[100] M. Matsuyama, J. P. Walsh, and H. Yeh. The effect of bathymetry on tsunami characteristics at Sisano Lagoon, Papua New Guinea. *Geophysical Research Letters*, 26(23):3513–3516, 1999.

[101] B.G. McAdoo and P. Watts. Tsunami hazard from submarine landslides on the Oregon continental slope. *Marine Geolog*, 203:235–245, 2004.

[102] P.A. Milewski, E.G. Tabak, C. Turner, R.R. Rosales, and F. Menzaque. Nonlinear stability of two-layer flows. *Comm. Math. Sci.*, 2(3):427–442, 2004.

[103] Don J. Miller. The Alaska earthquake of July 10, 1958: Giant wave in Lituya bay. *Bulletin of the Seismological Society of America*, 50(2):253–266, 1960.

[104] D. Mohrig and K. X. Whipple. Hydroplaning of subaqueous debris flows. *Geological Society of America Bulletin*, 110(3), 1998.

[105] L. F. Moody. Friction factors for pipe flow. *Trans. ASME*, 66(8):671–684, 1944.

[106] M. L. Munoz-Ruiz and C. Pares. Godunov method for nonconservative hyperbolic systems. *Mathematical Modelling and Numerical Analysis*, 41(1):169–185, 2009.

[107] O. Nwogu. Alternative form of Boussinesq equations for nearshore wave propagation. *Journal of waterway, port, coastal, and ocean engineering*, 119(6):618–638

[108] V. Ostapenko. Modified shallow water equations which admit the propagation of discontinuous waves over a dry bed. *Journal of Applied Mechanics and Technical Physics*, 48(6):795–812, 2007.

[109] V. V. Ostapenko. Complete systems of conservation laws for two-layer shallow water models. *Journal of Applied Mechanics and Technical Physics*, 40:796–804, 1999.

[110] V. V. Ostapenko. Numerical simulation of wave flows caused by a shoreside landslide. *Journal of Applied Mechanics and Technical Physics C/C of Zhurnal Prikladnoi Mkhaniki I Tekhnicheskoi Fiziki*, 40:647–654, 1999.

[111] L. V. Ovsyannikov. Two-layer shallow water model. *Prikl. Mekh. Tekh. Fiz.*, (2):3–14, 1979.

[112] M. Pailha and O. Pouliquen. A two-phase flow description of the initiation of underwater granular avalanches. *J. Fluid Mech. Journal of Fluid Mechanics*, 633:115–135, 2009.

[113] M. Pelanti, F. Bouchut, and A. Mangeney. A Roe-type scheme for two-phase shallow granular flows over variable topography. *Mathematical Modelling and Numerical Analysis*, 42(5):851–886, 2009.

[114] E. Pelinovsky and A. Poplavsky. Simplified model of tsunami generation by submarine landslides. *Physics and Chemistry of The Earth*, 21(1-2):13–17, 1996.

[115] D. H. Peregrine. Long waves on a beach. *Journal of Fluid Mechanics*, 27, 1967.

[116] M. Pirulli. Numerical modelling of landslide runout. A continuum mechanics approach, 2005.

[117] P. Pistek and P. E. La Violette. Observations of the suppression of tide-generated nonlinear internal wave packets in the Strait of Gibraltar. *J. of Marine Systems*, 20(1/4):113–128, 1999.

[118] E. B. Pitman and L. Le. A two-fluid model for avalanche and debris flows. *Philosophical Transactions: Mathematical, Physical and Engineering Sciences*, 363(1832):1573–1601, 2005.

[119] S.P. Pudasaini and K. Hutter. Rapid shear flows of dry granular masses down curved and twisted channels. *J. Fluid Mech.*, 495:193–208, 2003.

[120] L. Rondon, O. Pouliquen, and P. Aussillous. Granular collapse in a fluid: Role of the initial volume fraction. *Physics of Fluids*, 23(7), 2011.

[121] R. Salmon. Numerical solution of the two-layer shallow water equations with bottom topography. *Journal of Marine Research*, 60:605–638, 2002.

[122] K. Satake. Tsunami modeling from submarine landslides. *Proceedings of the International Tsunami Symposium*, pages 665–674, 2001.

[123] S.B. Savage and K. Hutter. The motion of a finite mass of granular material down a rough incline. *J. Fluid Mech.*, 199:177–215, 1989.

[124] H. A. Schäffer and P. A. Madsen. Further enhancements of Boussinesq-type equations. *Coastal Engineering*, 26(1–2):1–14, 9 1995.

[125] H. B. Seed. *The landslide at the Port of Nice on October 16, 1979.* Earthquake Engineering Research Center, University of California, 1988.

[126] F. Shi, J. T. Kirby, J. C. Harris, J. D. Geiman, and S. T. Grilli. A high-order adaptive time-stepping tvd solver for Boussinesq modeling of breaking waves and coastal inundation. *Ocean Modelling*, 43:36–51

[127] J. O. Shin, S. B. Dalziel, and P. F. Linden. Gravity currents produced by lock exchange. *Journal of Fluid Mechanics*, 521:1–34, 2009.

[128] P K Sweby. High resolution schemes using flux limiters for hyperbolic conservation laws. *SIAM J. on Numerical Analysis*, 21(5):995–1011 1984.

[129] S. Sweet and E.A. Silver. Tectonics and slumping in the source region of the 1998 Papua New Guinea tsunami from seismic reflection images. *Pure and Applied Geophysics*, 160:1945–1968, 2003.

[130] C.E. Synolakis, J. Bardet, J.C. Borrero, H.L. Davies, E.A. Okal, E.I. Silver, S. Sweet, and D.R. Tappin. The slump origin of the 1998 Papua New Guinea tsunami. *Mathematical, physical and Engineering Sciences*, 458(2020):763–789, 2002.

[131] T. Takahashi. *Debris flow: mechanics, prediction and countermeasures*. Taylor & Francis, 2007.

[132] O. D. S. Taylor, A. S. Bradshaw, C. D. P. Baxter, and S. T. Grilli. The effects of basal resistance and hydroplaning on the initial kinematics of seismically induced tsunamigenic landslides. *Geotechnical special publication.*, (178):522–529, 2008.

[133] S.W. Tinti, G. Pagnoni, and F. Zaniboni. The landslides and tsunamis of the 30th of december 2002 in stromboli analysed through numerical simulations. *Bulletin of Volcanology*, 68(5):462–479, 2006-04-01.

[134] M. Tonelli and M. Petti. Hybrid finite volume- finite difference scheme for 2DH improved Boussinesq equations. *Coastal Engineering*, 56(5):609–620

[135] D. J Varnes. Slope movement types and processes. *Transportation Research Board Special Report*, (176 0360-859X), 1978.

[136] D. Völker, J. Geersen, J. H. Behrmann, and W. R. Weinrebe. *Submarine mass wasting off Southern Central Chile: Distribution and possible mechanisms of slope failure at an active continental margin*, pages 379–389 Springer, 2012.

[137] B. Wagner, O. Bennike, M. Klug, and H. Cremer. First indication of Storegga tsunami deposits from East Greenland. *Journal of Quaternary Science*, 22(4):321–325 2007.

[138] S. N. Ward. Landslide tsunami. *Journal of Geophysical Research: Solid Earth (1978–2012)*, 106(B6):11201–11215

[139] P. Watts. Water waves generated by underwater landslides, Ph.D. thesis, Caltech, 1997.

[140] P. Watts. Probabilistic predictions of landslide tsunamis off Southern California. *Marine Geology*, 203(3):281–301

[141] G. Wei, J. T. Kirby, S. T. Grilli, and R. Subramanya. A fully nonlinear Boussinesq model for surface waves. part 1. highly nonlinear unsteady waves. *Journal of Fluid Mechanics*, 294(13):71–92, 1995.

[142] R. Weiss, S. Krastel, A. Anasetti, and K. Wunnemann. Constraining the characteristcs of tsunami waves from deformable submarine slides.

[143] R. Weiss and K. Wuennemann. Understanding tsunami by landslides as the next challenge for hazard, risk and mitigation: Insight from multi-material hydrocode modeling. *AGU Fall Meeting*, page C6, Dec 2007.

[144] H. Zhou and M. H. Teng. Extended fourth-order depth-integrated model for water waves and currents generated by submarine landslides. *J. Eng. Mech. Journal of Engineering Mechanics*, 136(4):506–516, 2010.

VITA

Jihwan Kim was born in Seoul, Korea and earned his Bachelors degrees in mathematics at Seoul National University, Korea. He received an M.S. in applied mathematics at the University of Manchester, UK. He then earned Ph.D. in applied mathematics at the University of Washington in 2014.